

1-2-2013

# Design, Synthesis, And Luminescence Properties Of Bridged Dimetallic Lanthanide Coordination Compounds

Jeremiah David Moore  
*Wayne State University,*

Follow this and additional works at: [http://digitalcommons.wayne.edu/oa\\_dissertations](http://digitalcommons.wayne.edu/oa_dissertations)

 Part of the [Chemistry Commons](#)

---

## Recommended Citation

Moore, Jeremiah David, "Design, Synthesis, And Luminescence Properties Of Bridged Dimetallic Lanthanide Coordination Compounds" (2013). *Wayne State University Dissertations*. Paper 787.

This Open Access Dissertation is brought to you for free and open access by DigitalCommons@WayneState. It has been accepted for inclusion in Wayne State University Dissertations by an authorized administrator of DigitalCommons@WayneState.

**DESIGN, SYNTHESIS, AND LUMINESCENCE PROPERTIES  
OF BRIDGED DIMETALLIC LANTHANIDE  
COORDINATION COMPOUNDS**

by

**JEREMIAH D. MOORE**

**DISSERTATION**

Submitted to the Graduate School

of Wayne State University,

Detroit, Michigan

in partial fulfillment of the requirements

for the degree of

**DOCTOR OF PHILOSOPHY**

2013

MAJOR: CHEMISTRY

Approved by:

\_\_\_\_\_  
Advisor

\_\_\_\_\_  
Date

\_\_\_\_\_

\_\_\_\_\_

\_\_\_\_\_

## **DEDICATION**

My dissertation is dedicated to my Mother and Father, Grandma and Grandpa Moore, Nona and Papa, and Katherine. All of you have fostered my love of science and my pursuit of understanding. Thank you all for your wisdom, patience, and love.

## ACKNOWLEDGMENTS

I would like to express my deepest gratitude to my advisor, Dr. Matthew J. Allen, for his support, guidance, and tireless effort throughout my graduate career, and for his confidence and optimism in allowing me to pursue a project of my own interest. I am thankful to my committee members, Dr. Zhongwu Guo, Dr. Gavin Lawes, and Dr. Charles Winter, for giving their time and energy to help me through this process. I thank Dr. G. Andrés Cisneros and Dr. Richard Lord for their fruitful collaboration and insight, without which much of my work would have remained a mystery. I am grateful to Dr. John Endicott for teaching me how to think about spectroscopy and energy levels, Dr. Claudio Verani for sharing his knowledge on magnetism and spectroscopy, Dr. Ivan Lysenko for our many discussions about organic synthesis, Dr. Stanislav Groysman for the use of his infrared spectrometer, Dr. Mike McGillivary for teaching me HPLC and LCMS, Dr. David Benson for welcoming me into his group, and Drs. Peter Andreana and James Rigby for their steadfast advice and support for the PLU.

My work could not have been completed without the help of the CIF and LIC staff, Dr. Bashar Ksebati, Dr. Brian Shay, Dr. Lew Hryhorczuk, Dr. Philip Martin, Dr. Judy Westrick, Dr. David Coleman, Marty Krol, and Nestor Ocampo, who I thank for their assistance, training, helpful conversations, and friendship.

I enjoyed my time at Wayne State in large part because I was fortunate enough to work beside people I love: my friends and colleagues in the Allen Group, Dr. Yujiang Mei, Dr. Prabani Dissanayake, Nipuni Gamage, Derek Averill, Nikhil Barua, Levi Ekanger, Joel Garcia, Lauren Hopper, Akhila Wedagedara, Chamika Lenora, Zhijin Lin, Buddhima Mahanama, Stephanie Neal, and especially to Sashi Vithanarachchi, my hood-mate, confidant, and mother of the Allen Group; Dr. Christopher Snyder, who's friendship, generosity, and intellect knows no

bounds; Dr. Tomasz Respondek, who's knowledge is only exceeded by his kindness, who's friendship is that of a brother, and with whom I share a desire for truth; Janir Datucan, who helped me to laugh again and again; members of the Second Street house, Dr. Ben Swarts, Dr. Mark Saly, and Jean Paul Bourgault, with whom far too much fun was had; the lunch crew, Dr. Baptiste Jolland, Dr. Fernando Xavier, and Mathilde Niocelle; and Madiha Khalid, David Nei, Dr. Irina Pala, Dr. Myriame Moume-Pymbock, and Dajena Tomco.

I also want to acknowledge Brendan Yonke, who shared the graduate school experience with me from Maryland, Adam Young, with whom I grew up and who helped me to get away from the lab when I needed it, and Dave Marchuck, who is such a good friend that he asks me about my work on 'lamthanites' to make me think I'm doing something smart.

I am tremendously grateful for the support of my parents, Dave and Mary Ann, my sisters Brandi and Kate, and my grandparents, James, Peggy, Frank, and Lillian, who provided me with sound values and inspiration to pursue this degree. I would also like to thank the most recent additions to my family, John and Monica and the Eklem and Hynds families, who so graciously accepted me into their lives and supported me in this endeavor. Finally, I am eternally indebted to my wife, Katherine, who keeps me calm, focused, and motivated, and who has more confidence in me than I have in myself, and used it to encourage me through every moment of my graduate career.

## TABLE OF CONTENTS

Dedication	ii
Acknowledgments	iii
List of Tables	vi
List of Figures	vii
List of Schemes	xi
Chapter 1: Multimetallic Lanthanide Complexes Toward Imaging Applications	1
Chapter 2: Ligand Design and Synthetic Attempts	27
Chapter 3: Concentration-Independent pH Detection with a Luminescent Dimetallic Eu <sup>3+</sup> -Based Probe	42
Chapter 4: Tb <sup>3+</sup> to Eu <sup>3+</sup> Energy Transfer in a Heterodimetallic Complex	55
Chapter 5: Summary, Conclusions, and Future Directions	78
Appendix A: Chapter 2 Data	86
Appendix B: Chapter 3 Data	96
Appendix C: Permissions	112
References	114
Abstract	126
Autobiographical Statement	127

## LIST OF TABLES

<b>Table 1.1.</b> Comparison of the distance between $Gd^{3+}$ chelates to calculated electronic relaxation times at 0.47 T. <sup>46</sup> Reprinted with permission from Moore, J.D.; Allen, M.J. <i>Recent Patents on Nanomedicine</i> <b>2011</b> , <i>1</i> , 88–100. Copyright 2011 Bentham Science Publishers.....	15
<b>Table 2.1.</b> Experimental conditions for attempts to synthesize <b>2.2</b> .....	29
<b>Table 4.1.</b> Summary of energy states involved in energy transfer for lanthanides used in <b>4.1–4.4</b> .....	55

## LIST OF FIGURES

- Figure 1.1.** Molecular structures of macrocyclic DOTA and acyclic DTPA. Reprinted with permission from Moore, J.D.; Allen, M.J. *Recent Patents on Nanomedicine* 2011, 1, 88–100. Copyright 2011 Bentham Science Publishers. ....3
- Figure 1.2.** Common chelates in multimeric ligands. Arrows point to positions where linking substituents can be attached. Reprinted with permission from Moore, J.D.; Allen, M.J. *Recent Patents on Nanomedicine* 2011, 1, 88–100. Copyright 2011 Bentham Science Publishers. ....4
- Figure 1.3a.** Multilanthanide complexes studied for use as contrast agents for MRI reported since 2006. Due to a lack of data necessary for comparison to other complexes described in this chapter, complex **1.10** is not discussed in the text.<sup>51</sup> Coordinated water molecules have been removed for clarity. Reprinted with permission from Moore, J.D.; Allen, M.J. *Recent Patents on Nanomedicine* 2011, 1, 88–100. Copyright 2011 Bentham Science Publishers. ....7
- Figure 1.3b.** Multilanthanide complexes studied for use as contrast agents for MRI reported since 2006. Due to a lack of relevant data, complexes **1.16** and **1.20** are not discussed in the text.<sup>52,53</sup> Coordinated water molecules have been omitted for clarity. Reprinted with permission from Moore, J.D.; Allen, M.J. *Recent Patents on Nanomedicine* 2011, 1, 88–100. Copyright 2011 Bentham Science Publishers. ....8
- Figure 1.4.** Multilanthanide complexes with nonrigid (**1.24**) and rigid (**1.25**) linkages deviate from the  $MW-1/\tau_R$  relationship observed in larger complexes. Reprinted with permission from Moore, J.D.; Allen, M.J. *Recent Patents on Nanomedicine* 2011, 1, 88–100. Copyright 2011 Bentham Science Publishers. ....9
- Figure 1.5.** Comparison of molecular weight to  $1/\tau_R$  for complexes **1.1–1.8**, **1.11–1.13**, **1.15**, and **1.17**. Values of  $1/\tau_R$  were determined by fitting NMRD data acquired at 298 K. The number at each point corresponds to the number of the complex shown in **Figures 1.3a** and **1.3b**. Reprinted with permission from Moore, J.D.; Allen, M.J. *Recent Patents on Nanomedicine* 2011, 1, 88–100. Copyright 2011 Bentham Science Publishers. ....10
- Figure 1.6.** Plot of  $\omega_I$  (♦) and  $1/T_{1e}$  for GdDOTA (■) over the low to ultra-high magnetic field strength range. The gray bar represents the range of field strengths at which most multilanthanide complexes have been studied up to common clinical field strengths. Reprinted with permission from Moore, J.D.; Allen, M.J. *Recent Patents on Nanomedicine* 2011, 1, 88–100. Copyright 2011 Bentham Science Publishers. ....14

<b>Figure 1.7.</b>	Multilanthanide PARACEST agents that contain exchangeable protons capable of reducing the bulk-water-signal intensity (arrows point to exchangeable protons). Water molecules not observable by PARACEST have been omitted for clarity. Reprinted with permission from Moore, J.D.; Allen, M.J. <i>Recent Patents on Nanomedicine</i> <b>2011</b> , <i>1</i> , 88–100. Copyright 2011 Bentham Science Publishers. ....	18
<b>Figure 1.8.</b>	Illustration of the excitation and emission processes of a lanthanide ion by direct excitation (top left) and antenna-sensitized excitations (top right). Simple Jablonski diagram of lanthanide excitation and emission processes during direct excitation (bottom left) and antenna-sensitized excitation (bottom right). Reprinted with permission from Moore, J.D.; Allen, M.J. <i>Recent Patents on Nanomedicine</i> <b>2011</b> , <i>1</i> , 88–100. Copyright 2011 Bentham Science Publishers. ...	22
<b>Figure 1.9.</b>	Multilanthanide complexes studied as luminescence probes discussed in this review. Coordinated water molecules have been omitted for clarity. Reprinted with permission from Moore, J.D.; Allen, M.J. <i>Recent Patents on Nanomedicine</i> <b>2011</b> , <i>1</i> , 88–100. Copyright 2011 Bentham Science Publishers. ....	23
<b>Figure 2.1.</b>	Structure of ditopic ligand <b>2.1</b> , designed to bridge two Ln <sup>3+</sup> ions with an alcohol donor .....	27
<b>Figure 3.1.</b>	Natural log plot of luminescence intensity of <b>3.1</b> in H <sub>2</sub> O (□) and D <sub>2</sub> O (○) as a function of time. Reprinted with permission from Moore, J.D.; Lord, R.L.; Cisneros, G.A.; Allen, M.J. <i>J. Am. Chem. Soc.</i> <b>2012</b> , <i>134</i> , 17372–17375. Copyright 2012 American Chemical Society.....	48
<b>Figure 3.2.</b>	Natural log plots of luminescence intensity of <b>3.1</b> in 50 mM citrate and 50 mM phosphate buffer at pH values of 4 (red) through 8 (pink) by 0.2 pH units. Reprinted with permission from Moore, J.D.; Lord, R.L.; Cisneros, G.A.; Allen, M.J. <i>J. Am. Chem. Soc.</i> <b>2012</b> , <i>134</i> , 17372–17375. Copyright 2012 American Chemical Society.....	49
<b>Figure 3.3.</b>	Luminescence-decay rate of 0.5 (♦) and 1.0 mM (□) <b>3.1</b> as a function of pH (50 mM citrate, 50 mM phosphate, λ <sub>ex</sub> = 395 nm, λ <sub>em</sub> = 595 nm). Reprinted with permission from Moore, J.D.; Lord, R.L.; Cisneros, G.A.; Allen, M.J. <i>J. Am. Chem. Soc.</i> <b>2012</b> , <i>134</i> , 17372–17375. Copyright 2012 American Chemical Society.....	50
<b>Figure 3.4.</b>	Optimized structures of <b>3.1</b> <sup>-</sup> (left) and H <b>3.1</b> (right): Eu = pink, C = cyan, N = blue, O = red, and H = white. Non-exchangeable hydrogen atoms are omitted for clarity. Reprinted with permission from Moore, J.D.; Lord, R.L.; Cisneros, G.A.; Allen, M.J. <i>J. Am. Chem. Soc.</i> <b>2012</b> , <i>134</i> , 17372–17375. Copyright 2012 American Chemical Society.....	51

<b>Figure 3.5.</b>	Comparison of emission spectra of <b>3.1</b> at pH 4.4 (solid line) and pH 7.4 (dashed line) (0.5 mM <b>3.1</b> , 50 mM citrate, 50 mM phosphate, $\lambda_{\text{ex}} = 395$ nm). Arrows point to peaks that may result from a second $\text{Eu}^{3+}$ environment. Reprinted with permission from Moore, J.D.; Lord, R.L; Cisneros, G.A.; Allen, M.J. <i>J. Am. Chem. Soc.</i> <b>2012</b> , <i>134</i> , 17372–17375. Copyright 2012 American Chemical Society.....	52
<b>Figure 3.6.</b>	Proposed mechanism for the response of <b>3.1</b> to changes in pH. At high pH (top), the lack of OH oscillators leads to long-lived luminescence (long wavy arrows, $\lambda_{\text{em}}$ ). At low pH (bottom), the bridging OH oscillator quenches the $\text{Eu}^{3+}$ excited state leading to rapid luminescence decay (short wavy arrows, $\lambda_{\text{em}}$ ). Reprinted with permission from Moore, J.D.; Lord, R.L; Cisneros, G.A.; Allen, M.J. <i>J. Am. Chem. Soc.</i> <b>2012</b> , <i>134</i> , 17372–17375. Copyright 2012 American Chemical Society.....	53
<b>Figure 4.1.</b>	Previously reported multimetallic complexes that exhibit Ln–Ln energy transfer. <sup>83, 113–115</sup> .....	54
<b>Figure 4.2.</b>	Dimetallic complexes reported in this chapter .....	57
<b>Figure 4.3a.</b>	(a) HPLC chromatogram of <b>4.7</b> prior to HPLC purification ( $\lambda_{\text{ex}} = 394$ nm, $\lambda_{\text{em}} = 616$ nm). (b) Extracted mass spectrum at 14.620 min retention time. (c) Extracted mass spectrum at 15.700 min retention time.....	59
<b>Figure 4.3b.</b>	(d) Extracted mass spectrum at 17.410 min retention time. Inset illustrates the 5-arm species that corresponded to the observed mass peaks. (e) Extracted mass spectrum at 18.745 min retention time. Inset illustrates the 5-arm species that corresponded to the observed mass peaks. (f) Extracted mass spectrum at 21.415 min retention time. Inset illustrates the monometallated $\text{Eu}^{3+}$ -containing 6-arm species that corresponded to the observed mass peaks.....	60
<b>Figure 4.4.</b>	(Top) HPLC chromatogram of <b>4.7</b> ( $\lambda_{\text{ex}} = 394$ nm, $\lambda_{\text{em}} = 616$ nm). (Bottom) Extracted mass spectrum averaged over 13.945–15.055 min retention time .....	61
<b>Figure 4.5.</b>	(Top) HPLC chromatogram of <b>4.8</b> ( $\lambda_{\text{ex}} = 228$ nm, $\lambda_{\text{em}} = 545$ nm). (Bottom) Extracted mass spectrum averaged over 3.805–5.170 min retention time .....	62
<b>Figure 4.6.</b>	(Top) HPLC chromatogram of mixture of <b>4.6</b> and <b>4.7</b> ( $\lambda_{\text{ex}} = 228$ nm, $\lambda_{\text{em}} = 545$ nm). (Middle) Extracted mass spectrum at 13.435 min retention time. (Bottom) Extracted mass spectrum at 14.005 min retention time.....	64

<b>Figure 4.7.</b>	Energy level diagram of Tb <sup>3+</sup> (top left) and Eu <sup>3+</sup> (top right) illustrating transitions involved in excitation and emission pathways and corresponding excitation and emission wavelengths. Representative emission spectra of Tb <sup>3+</sup> (bottom left) and Eu <sup>3+</sup> (bottom right). Peak assignments correspond to the <i>j</i> -value of the final <sup>7</sup> F <sub><i>j</i></sub> state. Position of energy levels based on data reported in references 116 and 118.....	66
<b>Figure 4.8.</b>	Steady state excitation spectra monitoring at 612 nm emission wavelength. Spectra are normalized to the most intense peak. Inset is zoomed on the y-axis only. Energy levels involved in the transitions are indicated above the spectrum with the corresponding ion. Arrow indicates Tb <sup>3+</sup> -specific excitation at a Eu <sup>3+</sup> emission wavelength .....	69
<b>Figure 4.9.</b>	Steady state excitation spectra monitoring at 545 nm emission wavelength. Spectra are normalized to the second order scattering peak designated by the asterisk. Inset is zoomed on the y-axis only. Energy levels involved in the transitions are indicated above the spectrum with the corresponding ion.....	70
<b>Figure 4.10.</b>	Steady state emission spectra ( $\lambda_{\text{ex}} = 394 \text{ nm}$ ). Spectra are normalized to the most intense peak. Assignments are indicated above the spectra with the corresponding ion.....	73
<b>Figure 4.11.</b>	Steady state emission spectra ( $\lambda_{\text{ex}} = 487 \text{ nm}$ ). Spectra are normalized to the most intense peak. Assignments are indicated above the spectra with the corresponding ion.....	73
<b>Figure 4.12.</b>	Proposed Jablonski diagram of energy transfer from Tb <sup>3+</sup> to Eu <sup>3+</sup> consistent with my observations.....	76
<b>Figure 5.1.</b>	(Left) Structure of ditopic ligand <b>5.1</b> also shown in <b>Figure 2.1</b> . (Middle) Proposed coordination mode of ligand <b>5.1</b> . (Right) Experimentally-determined coordination mode of ligand <b>5.1</b> .....	78
<b>Figure 5.2.</b>	Undetected contaminants in <b>5.5</b> (left) and <b>5.15</b> (right) that were not observed by TLC, MS, or NMR characterization. Both isomers are shown but have not been uniquely identified .....	80
<b>Figure 5.3.</b>	Structure of a dimetallic Eu <sup>3+</sup> complex and illustration of the likely mechanism of luminescence pH-response also reported in Chapter 3. Reprinted with permission from Moore, J.D.; Lord, R.L; Cisneros, G.A.; Allen, M.J. <i>J. Am. Chem. Soc.</i> <b>2012</b> , <i>134</i> , 17372–17375. Copyright 2012 American Chemical Society.....	81
<b>Figure 5.4.</b>	Dimetallic complexes reported in Chapter 4.....	82

## LIST OF SCHEMES

<b>Scheme 2.1.</b> Two-step retrosynthesis of the 2-propanolyl-bridged ditopic ligand .....	28
<b>Scheme 2.2.</b> Proposed HBr elimination side reaction that inhibited formation of the desired product, <b>2.2</b> .....	28
<b>Scheme 2.3.</b> Attempted route to synthesize <b>2.8</b> using tris-BOC-cyclen ( <b>2.4</b> ) .....	30
<b>Scheme 2.4.</b> Bis-aminal-cyclen-based synthesis of <b>2.2</b> .....	31
<b>Scheme 2.5.</b> Syntheses of protected 1,3-dibromo-2-propanol and ligand intermediates.....	33
<b>Scheme 2.6.</b> Attempted synthesis of the protected propanonyl-bridged ligand.....	34
<b>Scheme 2.7.</b> Synthesis of benzyl-protected 1,3-dibromo-2-propanol, <b>2.13</b> .....	35
<b>Scheme 3.1.</b> Synthetic route to <b>3.1</b> . Reprinted with permission from Moore, J.D.; Lord, R.L.; Cisneros, G.A.; Allen, M.J. <i>J. Am. Chem. Soc.</i> <b>2012</b> , <i>134</i> , 17372–17375. Copyright 2012 American Chemical Society.....	44
<b>Scheme 5.1.</b> Attempted synthetic routes to synthesize protected ligands <b>5.6</b> and <b>5.12–5.15</b> .....	79

## CHAPTER 1. Multimetallic Lanthanide Complexes Toward Imaging Applications

Adapted with permission from Moore, J.D.; Allen, M.J. *Recent Patents on Nanomedicine* **2011**, *1*, 88–100. Copyright 2011 Bentham Science Publishers.

### Introduction

Multimetallic lanthanide ( $\text{Ln}^{3+}$ ) complexes are widely studied because of their magnetic and luminescent properties. Due to these properties, multilanthanide complexes are potentially useful in nanomedicine, provided the complexes are chemically and kinetically inert, non-toxic, monodisperse, and well characterized. While many multimetallic lanthanide complexes have been studied, few meet all of these requirements.<sup>1–4</sup> The focus of this chapter is discrete multilanthanide complexes reported during the last five years that exhibit covalently linked chelates known to bind lanthanide ions tightly ( $\log K_{\text{GdL}} > 18$ ). Generally, this category of coordination compounds falls in an intermediate molecular weight range (1–6 kDa) and exhibits relatively short metal–metal distances ( $<600$  nm). Characterization of these discrete complexes allows for structure–function relationships to be definitively analyzed, and these relationships are important for understanding and optimizing similar and larger systems including polymers and dendrimers.<sup>5–21</sup> The scope of lanthanide-containing materials is too vast to be adequately described in a single chapter; consequently, this chapter will not address dendrimeric, polymeric, or bioconjugated polylanthanide complexes. Reviews for these types of molecules are available elsewhere.<sup>1,4,22–27</sup>

A unique feature of the lanthanides is that the most stable oxidation state for all of these elements is +3, yet they display a wide range of magnetic and luminescent properties over a relatively narrow size range (the +3 ionic radii of elements 58–71 are in the range of 102–86 pm).<sup>28</sup> A consequence of these properties is that lanthanide ions tend to form nearly isostructural complexes that commonly exhibit coordination numbers of 8–10. From a synthetic perspective,

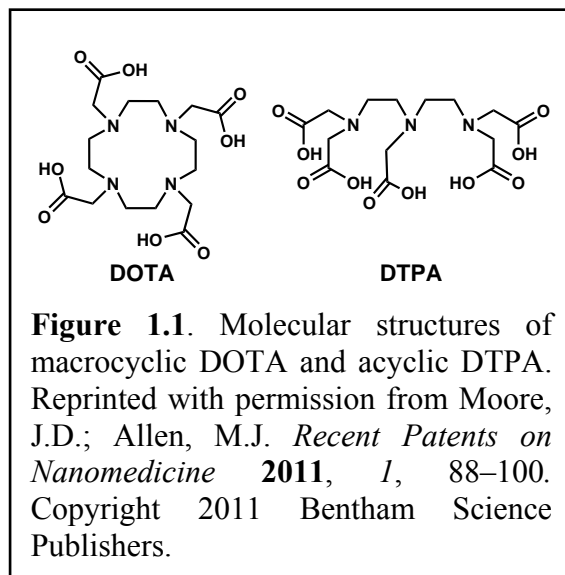
the near-isostructural nature of lanthanides is advantageous because a single ligand can be used to generate lanthanide complexes for a variety of medical applications including magnetic resonance imaging (MRI), optical imaging, and immunogenic assays. With such a wide variety of properties incorporated into almost isostructural elements a single ligand can generate a variety of complexes, accessing a host of different properties. Therefore, ligand design is a key focus for researchers interested in exploring applications of these elements.

Two applications for which multilanthanide complexes are studied include contrast agents for MRI and luminescent imaging probes. This chapter will cover these two topics with a brief introduction to each topic preceding a detailed discussion of the ligand design and multilanthanide complexes that have been investigated for each application. Chapter 1 will conclude with a summary of the contributions made to each field, the current state of multilanthanide research, a discussion of the future potential for this class of complexes, a description of how this work influenced the goals of my research, and a summary of the remaining chapters of my thesis.

### *Multimeric Ligand Design*

A variety of ligand motifs have been used to form multimetallic lanthanide complexes for medical applications. Discussion of the specific syntheses of multimeric ligands is beyond the scope of this article. The techniques employed have been developed in monomeric ligand syntheses that are thoroughly reviewed elsewhere.<sup>29</sup> As a result of the extensive research of monomeric polyamino polycarboxylates, the majority of multimeric ligands are derivatives of the monomeric chelators diethylenetriaminepentaacetic acid (DTPA) and 1,4,7,10-tetraazacyclododecane-1,4,7,10-tetraacetic acid (DOTA) (**Figure 1.1**). Both DOTA and DTPA form kinetically inert complexes with lanthanides under physiological conditions ( $k_d = 1.2 \times 10^3$

and  $21 \text{ s}^{-1}$  for GdDTPA and GdDOTA, respectively), and the gadolinium complexes of these ligands are clinically approved contrast agents for MRI.<sup>2,3</sup> While this review is not focused on monometallic lanthanide complexes, the basic chemistry of these complexes strongly influences the design of ligands for multilanthanide complexes. Thus, a brief discussion of the properties of monomeric complexes will be useful in understanding the design of their multimeric analogs.

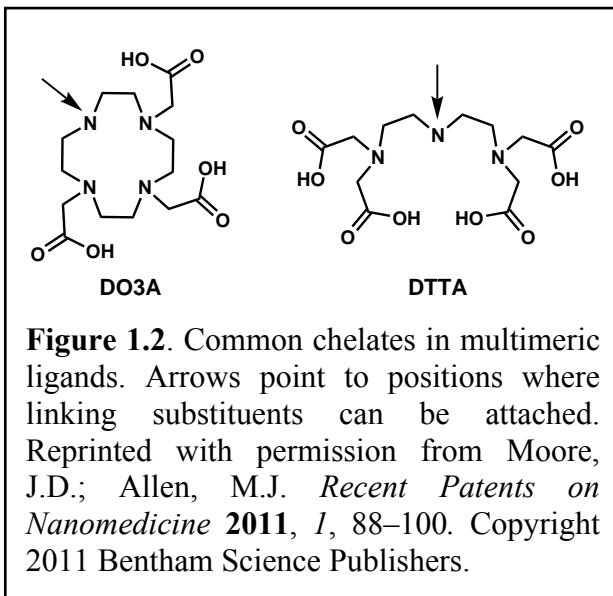


Most kinetically inert lanthanide complexes contain polydentate chelates with nitrogen- and oxygen-based donors.<sup>2,3</sup> The majority of these ligands are octadentate, leaving one coordination site for a solvent molecule or other ligand to bind to the metal ion. Two factors contribute to the inertness of these complexes: (1) the chelate effect and (2) electrostatic attraction. Furthermore, macrocyclic-based ligands such as DOTA gain additional stability over their acyclic counterparts due to the macrocyclic effect. Consequently, many multimeric ligands feature macrocyclic chelates, and a common scaffold for these chelates is 1,4,7,10-tetraazacyclododecane (cyclen).

Due to the success of GdDOTA as a contrast agent for MRI, N-functionalized-cyclen-based chelates are common in multilanthanide complexes. Cyclen has been functionalized with a variety of substituents including acetates, amides, phosphonates, alcohols, and ketones.<sup>30–33</sup> Due to the difference in basicity and nucleophilicity of its four nitrogen atoms, cyclen can be selectively functionalized such that one, two, or three nitrogens remain available for substitution

after one substituent is attached.<sup>29</sup> Thus, ligands can be designed in which three substituents serve as donors to the metal center while the remaining substituent covalently links multiple chelating moieties together (for example DO3A, **Figure 1.2**). The linking substituent is often designed with a donor atom such that eight donors are maintained and the kinetic stability of the chelate is minimally compromised.<sup>3</sup> This popular strategy was demonstrated in early contrast agent research by Tweedle and coworkers with the DO3A synthon.<sup>34</sup>

Although macrocyclic chelates are the most popular motifs used in multilanthanide complexes, acyclic chelates offer a different set of structural variations. A common acyclic chelate motif is diethylenetriaminetetraacetic acid (DTTA) (**Figure 1.2**). Multimeric ligands featuring this motif sometimes require sequential protection and deprotection steps to attach a linking moiety selectively.<sup>35</sup> The kinetic stability of the resulting lanthanide complexes is reduced relative to the parent DTPA complex when the linking moiety does not contain a donor atom, leaving the chelate with only seven metal-binding sites.<sup>35</sup> The reduced stability of seven-coordinate acyclic chelates has limited their use in multilanthanide complexes.



Of equal importance to chelate design is the choice of linking moieties to provide functionality. Linkers are used to determine the number of chelates, control metal–metal distance, rigidify the relative motion of metal ions, interact with analytes, and function as

antennas for absorbance and energy transfer. Linker structure and function will be discussed in detail in the following sections.

### Contrast Agents for MRI

The first application of multilanthanide systems that this chapter will describe is contrast agents for MRI, which is an important diagnostic technique for the medical field. Roughly 30% of images acquired in a clinical setting involve the administration of a contrast agent to increase the diagnostic information available from the images.<sup>2</sup> Contrast agents are paramagnetic substances that decrease the longitudinal ( $T_1$ ) and transverse ( $T_2$ ) relaxation times of water protons, thereby increasing contrast in images. Detailed reviews of relaxation theory have been published.<sup>3,36,37</sup> With seven unpaired electrons,  $Gd^{3+}$  is highly paramagnetic and especially well suited for use as a  $T_1$ -shortening contrast agent for MRI. However,  $Gd^{3+}$  is toxic as the free ion and, therefore, must be chelated in a kinetically inert ligand for use *in vivo*.<sup>38</sup>

In addition to kinetic inertness, a variety of other parameters can be tuned by changing ligand structure. These parameters ultimately influence a measurable value of contrast-agent efficiency called relaxivity, which has units of  $mM^{-1}s^{-1}$ . According to the Solomon–Bloembergen–Morgan (SBM) equations that describe the behavior of  $T_1$ -shortening contrast agents, optimal relaxivity ( $r_1$ ) is achieved when the condition in Equation 1.1 is satisfied:<sup>2,3</sup>

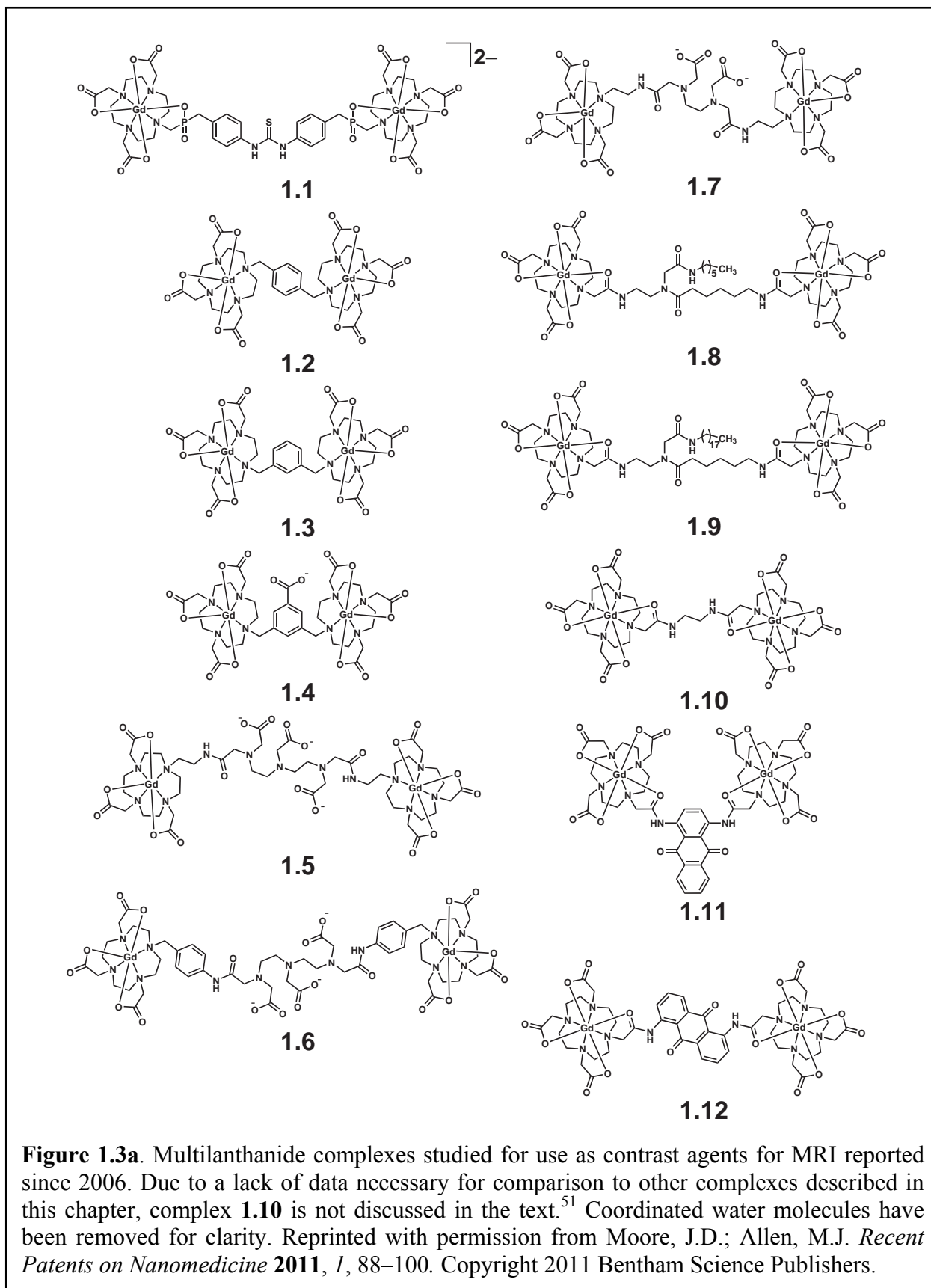
$$\text{Equation 1.1} \quad \omega_I = \frac{1}{\tau_R} + \frac{1}{\tau_m} + \frac{1}{T_{1e}}$$

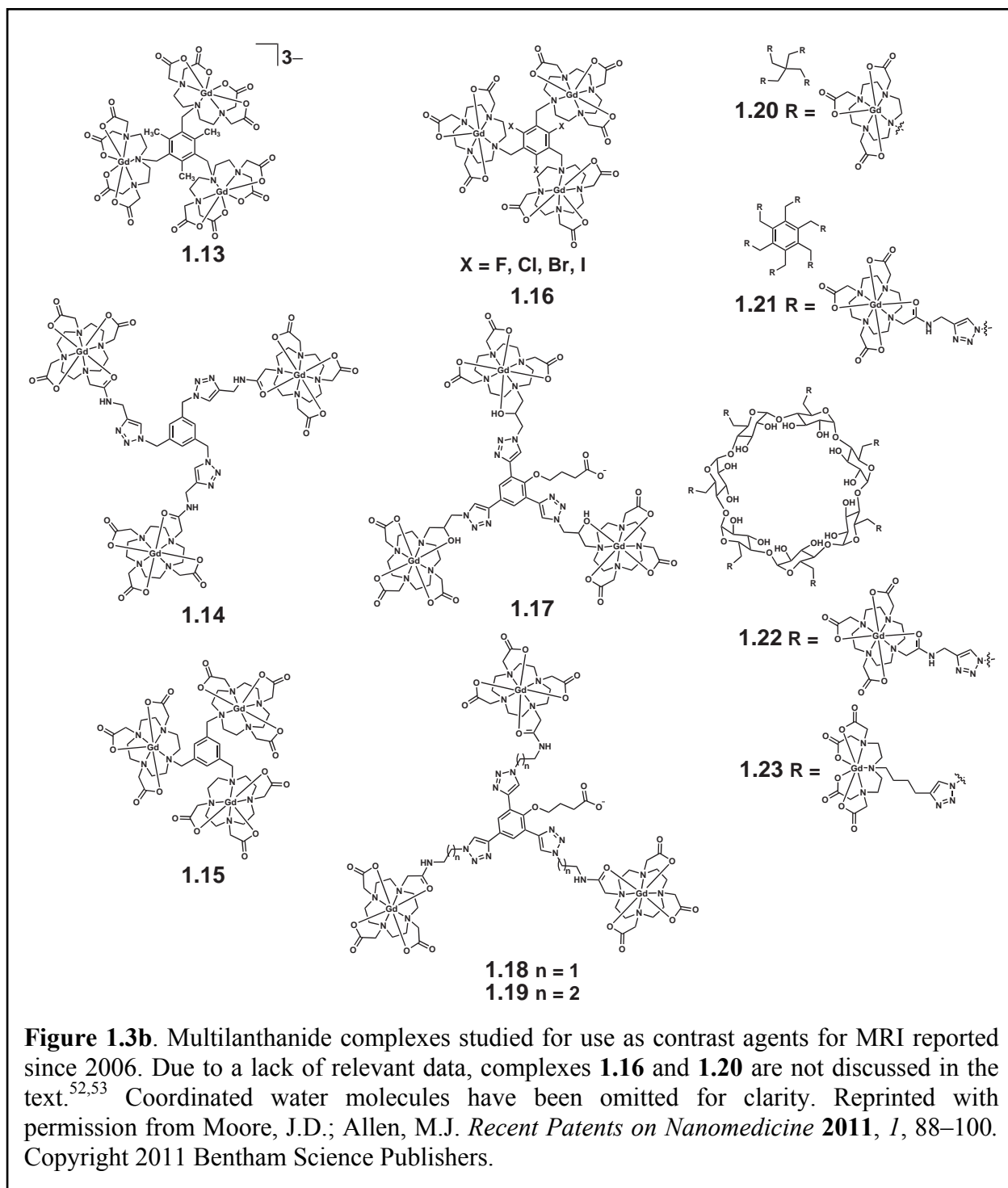
In Equation 1.1,  $\omega_I$  is the proton Larmor frequency,  $1/\tau_R$  is the rotational correlation rate,  $1/\tau_m$  is the bound-water exchange rate, and  $1/T_{1e}$  is the electronic relaxation rate of  $Gd^{3+}$ . A common magnetic field strength for the study of multilanthanide complexes is 0.47 T, which

corresponds to a proton Larmor frequency of 20 MHz, whereas a common clinical field strength is 1.5 T, which corresponds to a Larmor frequency of 64 MHz. While field strength influences relaxivity, the trends that I will elucidate from the studies of multilanthanide complexes are valid at clinical magnetic fields because at either field strength, the sum of  $1/\tau_R$ ,  $1/\tau_m$ , and  $1/T_{1e}$  must be on the order of  $10^7 \text{ s}^{-1}$  to achieve maximum relaxivity. Additionally, as magnet technology improves and higher field strengths become available, optimal values of these three parameters will need to be achieved through ligand design. The need to tune the structure of contrast agents for MRI to reach specific values of the three parameters listed above has resulted in decades of studies of monometallic lanthanide chelates, and several detailed reviews have been published on this topic.<sup>39–41</sup> Due to the multitude of studies focused on the relationship between the structural features of lanthanide chelates and their corresponding ability to function as contrast agents, a functional understanding of the effects of molecular structure on  $1/\tau_R$ ,  $1/\tau_m$ , and, to a lesser degree,  $1/T_{1e}$  has been developed. I will now describe the relationships between these parameters and the structure of multilanthanide complexes.

### *Rotational Correlation Rate*

The rotational correlation rate,  $1/\tau_R$ , describes the rotation of the Gd–H vector. Therefore, both the global and local motions of chelates affect the magnitude of  $1/\tau_R$ . The local component of  $1/\tau_R$  has been referred to as  $1/\tau_{l0}$  or  $1/\tau_R^*$  and has been analyzed as a separate component from the global  $1/\tau_R$  with the Lipari–Sazbo method.<sup>35,42,43</sup> While higher molecular weights result in slower values of  $1/\tau_R$  for monometallic chelates, this relationship is essentially nonexistent for multilanthanide complexes of intermediate molecular weight such as those shown in **Figures 1.3a** and **1.3b**. Studies on the behavior of intermediate to high molecular weight compounds with multiple lanthanide chelates indicate that the local motion of one chelate relative to another

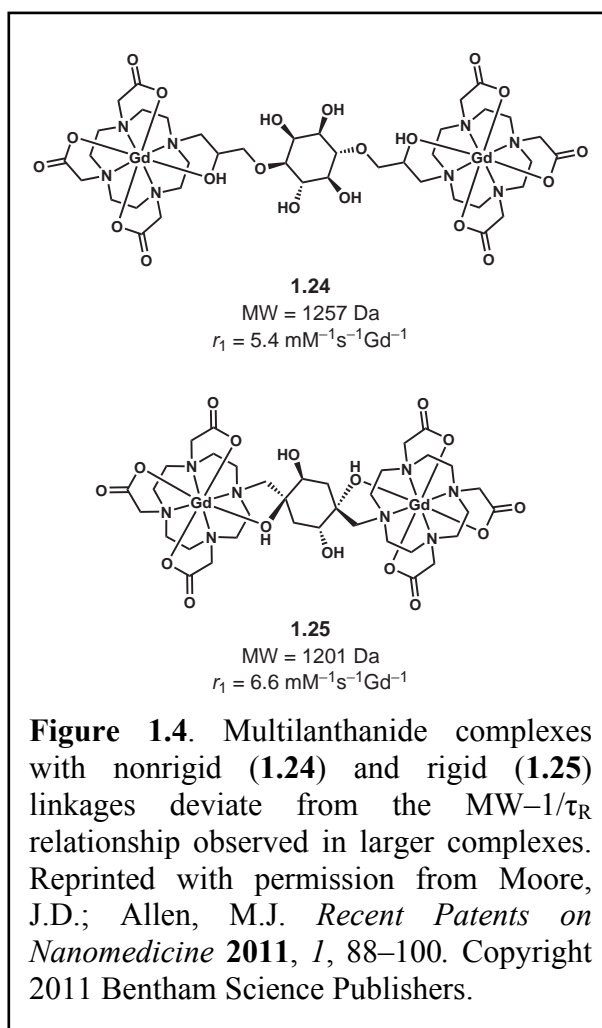




limits the degree to which a high molecular weight can decrease  $1/\tau_R$ . An early study demonstrated the influence of local motion on  $1/\tau_R$  and relaxivity using a cyclic moiety to bridge two DO3A-type chelates (**Figure 1.4**).<sup>34</sup> Relative to the more flexible linker on complex **1.24**, a

slightly higher relaxivity was achieved with **1.25**. However, inspection of molecular structure reveals that even the cyclic-linked structure retains some degree of freedom between chelates due to potential ring inversion suggesting that even more rigidity is needed in linker design.

Analysis of recently reported dimetallic complexes also reveals that  $1/\tau_R$  is not strictly dependent on molecular weight. Of the 23 complexes presented in this review, only 14 were reported with  $1/\tau_R$  values calculated by fitting nuclear magnetic resonance dispersion (NMRD) data at 298 K. (Values of  $1/\tau_R$  determined using  $^{17}\text{O}$ -NMR spectroscopy cannot be directly compared to NMRD-derived values because the  $^{17}\text{O}$ -NMR technique assesses  $1/\tau_R$  of the Gd–O vector, which is different than  $1/\tau_R$  of the Gd–H vector that is assessed using NMRD data.) Plotting  $1/\tau_R$  for these complexes against molecular weight reveals no apparent relationship (**Figure**



**1.5**).<sup>35,44–50</sup> The lack of a correlation between  $1/\tau_R$  and molecular weight may be due in part to the narrow molecular weight range (1100–6000 Da) of this class of compounds, but it is also attributable to the lack of a quantitative model to predict the degree to which the local motion of the chelates contributes to  $1/\tau_R$ . For instance, inspection of **1.2** and **1.3** suggests that steric repulsion between the chelates in **1.3** should restrict the local motion of the chelates relative to

the chelates in **1.2**.<sup>45</sup> Therefore,  $1/\tau_R$  might be expected to be slower for **1.3** than **1.2** due to a slower  $1/\tau_R^*$ . However,  $1/\tau_R$  is 36% slower for **1.2** than it is for **1.3**. The reason behind this apparent disagreement may be that the hydrodynamic radius of **1.2** is slightly larger than that of **1.3** due to para-versus meta-substitution of the linker. In cases where the hydrodynamic radius can be regarded as similar, such as for **1.3** and **1.4**, the molecular weight appears to correlate inversely with  $1/\tau_R$ .

Complexes **1.5–1.7** also show an inverse correlation between  $1/\tau_R$  and molecular weight.<sup>46</sup> In this case,  $1/\tau_R$  and

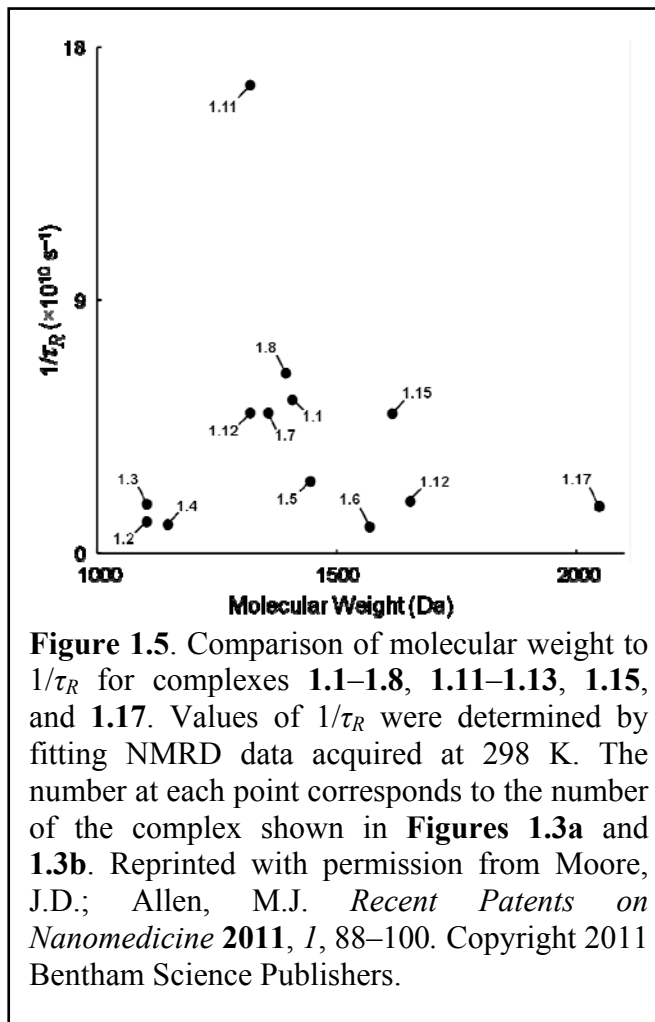


**Figure 1.5.** Comparison of molecular weight to  $1/\tau_R$  for complexes **1.1–1.8**, **1.11–1.13**, **1.15**, and **1.17**. Values of  $1/\tau_R$  were determined by fitting NMRD data acquired at 298 K. The number at each point corresponds to the number of the complex shown in **Figures 1.3a** and **1.3b**. Reprinted with permission from Moore, J.D.; Allen, M.J. *Recent Patents on Nanomedicine* **2011**, *1*, 88–100. Copyright 2011 Bentham Science Publishers.

relaxivity both follow the expected trends of decreasing and increasing, respectively, with increasing molecular weight. Although the authors refer to the rigidity of the structure of **1.6** relative to **1.5** as an explanation for its slower  $1/\tau_R$  and higher relaxivity, it is important to note that **1.6** also has the highest molecular weight of the three similar complexes.<sup>46</sup> The influence of molecular weight on  $1/\tau_R$  was not of particular interest to the study, which focused on  $\text{Ca}^{\text{II}}$  binding, but demonstrates the combined effect of rigidity and molecular weight on  $1/\tau_R$  in multimetallic species. The lessons learned from studying multilanthanide complexes indicate that the rigidity of macromolecular structure is paramount to achieving maximum relaxivity;

however, in spite of a qualitative understanding of the value of  $1/\tau_R$ ,  $1/\tau_R$  for new multilanthanide complexes is difficult to estimate. Further fundamental studies exploring the modulation of  $1/\tau_R$  and  $1/\tau_R^*$  are necessary to enable rational improvements to the design of multilanthanide and macromolecular complexes as contrast agents for MRI. These improvements include the use of ultra-high-field magnets that generate higher resolution images in shorter scan times, properties that are likely to improve clinical diagnosis.

### *Water-Exchange Rate*

Water-exchange-rate,  $1/\tau_m$ , is usually not the limiting factor in relaxivity for low to intermediate molecular weight contrast agents. However,  $1/\tau_m$  becomes limiting as magnetic field strength increases, and  $1/\tau_m$  will need to be modulated to generate effective contrast agents at ultra-high magnetic field strengths ( $\geq 7$  T). Methods of modulating  $1/\tau_m$  include changing ligand basicity or changing the number of coordinating atoms.<sup>54–56</sup> More basic chelates decrease Lewis acidity of coordinated lanthanide ions, which in turn results in weaker water–lanthanide interactions and a concomitant increase in  $1/\tau_m$ . Also, complexes formed from heptacoordinate chelates typically exhibit a faster  $1/\tau_m$  than complexes formed with octadentate chelates, consistent with an associative water-exchange mechanism allowed by the second available coordination site. As a point of reference,  $1/\tau_m$  values for GdDOTA and GdDTPA are  $4.1 \times 10^6$  s<sup>-1</sup> and  $3.3 \times 10^6$  s<sup>-1</sup>, respectively, an order of magnitude slower than optimal at 0.47 T and even less optimal at higher fields.<sup>57</sup> Therefore, a faster  $1/\tau_m$  is desirable regardless of field strength. Values of  $1/\tau_m$  are especially important for higher molecular weight complexes where  $1/\tau_R$  is near an optimal value and  $1/\tau_m$  begins to be the limiting factor in optimizing relaxivity.

The charge and denticity of a chelate are the primary structural features that affect  $1/\tau_m$ . As many synthetic strategies have centered upon DO3A- or DTTA-type chelating moieties, the

charge of the ligand is typically only determined by the charges of the substituents on the cyclen or ethylene triamine backbone. Consequently, many multimeric ligands carry three acetate groups per  $\text{Gd}^{3+}$  ion to form neutral complexes.

An alternative method to increase  $1/\tau_m$  is to sterically crowd the water-binding site.<sup>54-56</sup> Designing a ligand that introduces steric interference without eliminating the coordinated water molecule is a challenging task. As a result, little research has been conducted with an aim to modulate water exchange in multilanthanide complexes, although several multilanthanide complexes exhibit a faster water exchange rate compared to their monometallic counterparts. For instance, **1.1** exhibits a nearly optimal  $1/\tau_m$  value of  $1.9 \times 10^7 \text{ s}^{-1}$  at 0.47 T where  $\omega_I$  is  $2.0 \times 10^7 \text{ s}^{-1}$ .<sup>44</sup> Complexes **1.3**, **1.4**, **1.7**, and **1.15** have  $1/\tau_m$  values roughly an order of magnitude closer to  $\omega_I$  than GdDOTA.<sup>45,46,49</sup> The faster  $1/\tau_m$  for **1.3**, **1.4**, **1.7**, and **1.15** can be attributed to the associative exchange mechanism induced by the heptacoordinate chelates and is probably not due to steric crowding. However, the steric effect of packing several chelates close together is evidenced by the hydration number,  $q$ , of these complexes. Rather than the expected  $q = 2$ , heptacoordinate chelates **1.3**, **1.4**, and **1.7** are monohydrated at each lanthanide.<sup>45,46</sup>

Conversely, complexes **1.8**, **1.9**, **1.11**, and **1.12** have slower exchange rates than GdDOTA and GdDTPA which can be attributed to the substitution of an acetate with an amide attached to the linker.<sup>47,48</sup> Therefore, the Lewis acidity of  $\text{Gd}^{3+}$  in these complexes is likely greater compared to tetra- or pentaacetate analogues, leading to stronger water-Gd interactions. However, the Lewis acidity of the  $\text{Gd}^{3+}$  ions is not the only factor affecting the water-exchange rates observed for multilanthanide complexes.

Complex **1.13** is a unique example of a multilanthanide complex that contains three DTTA-based chelates.<sup>35</sup> Surprisingly, the water-exchange rate for **1.13** ( $1/\tau_m = 9.01 \times 10^6 \text{ s}^{-1}$ ) is

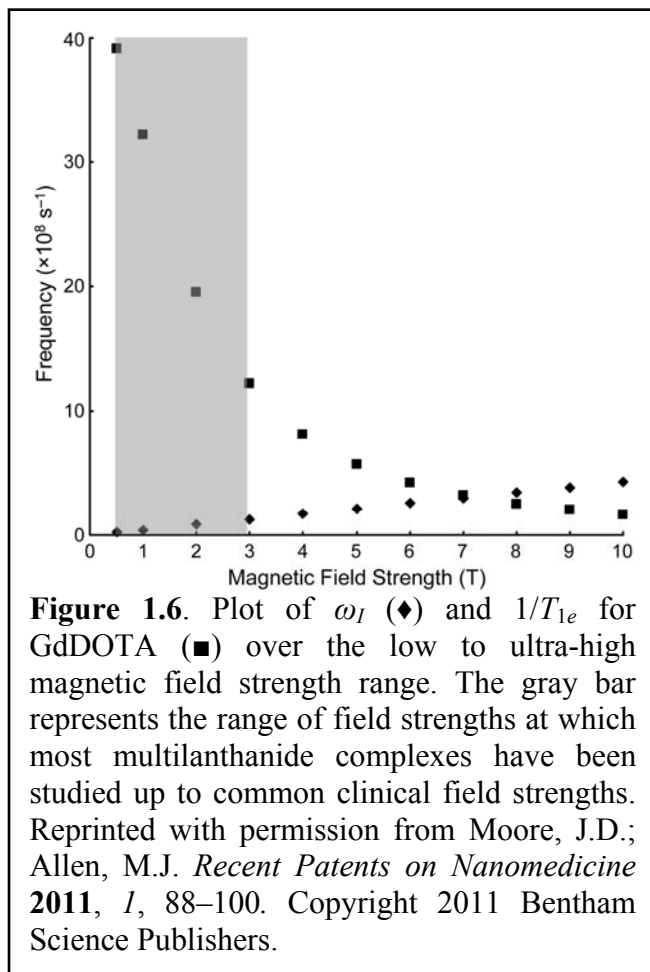
three times slower than that of the DO3A-based analog, **1.15** ( $1/\tau_m = 32 \times 10^6 \text{ s}^{-1}$ ), even though the  $\text{Gd}^{3+}$  ions in **1.13** are less Lewis acidic than those in **1.15**.<sup>35,49</sup> Further,  $1/\tau_m$  is slower in **1.13** than in **1.1**, **1.3**, **1.4**, and **1.7**, all of which are reported with  $q = 1$  and would be expected, therefore, to exchange water more slowly.<sup>35,44–46,49</sup> It is not obvious what structural features cause this difference in water-exchange rates and, in particular, what causes the water-exchange rate of **1.13** to be slower than what we might expect relative to the DO3A-based **1.15**. With this difference in mind, it would be intriguing to compare the water-exchange rates of the heptagadolinium  $\beta$ -cyclodextran-based **1.22** and **1.23** that presumably have high enough molecular weights that the water-exchange rates will contribute to relaxivity.<sup>58–60</sup> Complexes **1.22** and **1.23** differ in their chelates, and a comparison of their water-exchange rates would be useful to study the effect of chelate structure on relaxivity. However,  $1/\tau_m$  was not reported for these complexes.

In general, a challenge associated with directly studying water exchange in multilanthanide complexes is the complexity of synthesizing multimeric ligands. However, comparison of  $1/\tau_m$  to  $\omega_I$  at higher magnetic fields reveals that  $1/\tau_m$  may become limiting for many multilanthanide complexes.<sup>2,3</sup> Further, the relaxivity of macromolecular systems with  $1/\tau_R$  approaching  $\omega_I$  will be limited by  $1/\tau_m$  indicating a need to optimize  $1/\tau_m$  in these larger systems; therefore, there is a need in contrast agent research to address  $1/\tau_m$  modulation in multilanthanide systems.

### *$\text{Gd}^{3+}$ Electronic Relaxation Rate*

The potential of multilanthanide complexes to be used as contrast agents for MRI should be discussed noting that changes in electronic relaxation rate,  $1/T_{1e}$ , have been observed in multilanthanide complexes.<sup>61–63</sup> The electronic relaxation rate is typically estimated based on the

zero field splitting parameter,  $\Delta^2$ , and the electronic-relaxation correlation time,  $\tau_v$ .<sup>64</sup> Substituting the reported  $\Delta^2$  and  $\tau_v$  values for GdDOTA into Equation 1.2,<sup>64</sup> we calculated  $1/T_{1e}$  for field strengths from 0.5 to 10 T and plotted these values and  $\omega_I$  versus field strength (**Figure 1.6**). Equation 1.2 is considered to be valid only in the range where  $\omega_s^2\tau_v^2 \ll 1$ , where  $\omega_s$  is the electron Larmor frequency and  $S$  is the  $Gd^{3+}$  electron spin ( $S = 7/2$ ).<sup>64</sup> Therefore, these values are our best estimate due to the lack of empirical analysis of  $1/T_{1e}$  outside this range. Comparison of the two functions



shows that  $1/T_{1e}$  is 750% faster than optimum at 1.5 T. While  $1/T_{1e}$  is an order of magnitude closer to  $\omega_I$  than  $1/\tau_R$  for the monometallic GdDOTA,  $1/T_{1e}$  and  $1/\tau_R$  are on the same order of magnitude ( $10^9 \text{ s}^{-1}$ ) for several multilanthanide complexes. Of the complexes presented in this review, four have  $1/T_{1e}$ -limited relaxivity based on a comparison of  $1/\tau_R$ ,  $1/\tau_m$ , and  $1/T_{1e}$  values. It is likely that  $1/T_{1e}$  is also limiting for higher molecular weight complexes. While the need to understand and manipulate  $1/T_{1e}$  is apparent, studies of monometallic  $Gd^{3+}$ -containing complexes to determine structural features that influence electronic relaxation have been inconclusive. Interestingly, the study of multilanthanide complexes could contribute to the improvement of contrast agents through increasing our understanding of  $1/T_{1e}$ .

$$\text{Equation 1.2 } \frac{1}{T_{1e}} = \frac{\tau_v \Delta^2}{25} [4S(S+1) - 3] \left[ \frac{1}{1 + \omega_s^2 \tau_v^2} + \frac{4}{1 + 4\omega_s^2 \tau_v^2} \right]$$

Previous reports describing multilanthanide complexes have suggested a dipolar relaxation mechanism as an explanation for shorter  $1/T_{1e}$  values in multimetallic systems.<sup>62–63</sup> However, if a dipolar relaxation mechanism is responsible for modulating  $1/T_{1e}$  in multilanthanide complexes,  $1/T_{1e}$  will likely depend on Gd–Gd distances and could be studied with a series of identical chelates and variable-length linkers. The results of these studies would enable the rational synthesis of systems with optimized  $1/T_{1e}$  to fulfill the condition in Equation 1.1. Currently, the design of macromolecular lanthanide-containing complexes for contrast agents is essentially limited to attempts to optimize  $1/\tau_R$  and  $1/\tau_m$ .

Although previous studies of dinuclear complexes **1.5–1.7** did not focus on electronic-relaxation rate,<sup>46</sup> I made an effort to elucidate a relationship between the distance separating the chelates (estimated by the number of atoms between Gd<sup>3+</sup> ions) and  $1/T_{1e}$  (calculated from reported  $\Delta^2$  and  $\tau_v$  values and Equation 1.2). My choice to compare only complexes **1.5–1.7** is based on the similarity in structure of the chelates and linkers. Other complexes were not considered part of the series due to the lack of structural similarity or published data. In complexes **1.5–1.7**,  $1/T_{1e}$  decreases from complex **1.7** (16-atom-separation) to complex **1.5** (19-atom-separation) to complex **1.6** (24-atom separation) (**Table 1.1**).

**Table 1.1.** Comparison of the distance between Gd<sup>3+</sup> chelates to calculated electronic relaxation times at 0.47 T.<sup>46</sup> Reprinted with permission from Moore, J.D.; Allen, M.J. *Recent Patents on Nanomedicine* **2011**, *1*, 88–100. Copyright 2011 Bentham Science Publishers.

Complex	Atom Separation	$T_{1e}$ (ps)
<b>1.7</b>	16	41.5
<b>1.5</b>	19	58.5
<b>1.6</b>	24	87.0

The purpose of this observation is not to make conclusions or a quantitative assessment of the data but to present the possibility that, with further study of multimetallic and in particular dimetallic lanthanide complexes, a method to modulate and understand  $1/T_{1e}$  could be developed. Currently, the absence of empirical data and direct experimental techniques to interrogate  $1/T_{1e}$  represents a challenging opportunity for exploration. Gaining a fundamental understanding of  $1/T_{1e}$  is necessary to improve contrast agents for current clinical fields and to understand how effective high-field contrast agents can be synthesized.

### *Hydration Number*

Another important factor in determining relaxivity is the hydration number of the lanthanide,  $q$ . Based on the SBM equations,  $r_1$  scales directly with  $q$ .<sup>3</sup> As mentioned, the disadvantage of chelates with a hydration number greater than one (with a few exceptions, see reference 65) is that these complexes tend to be kinetically labile and, therefore, toxic. Despite this limitation, researchers have synthesized multilanthanide complexes with linking moieties that do not contribute a coordinating atom, resulting in  $q = 2$  chelates. This design has resulted in some of the highest relaxivity multilanthanide complexes such as **1.13** ( $r_1 = 15.70 \text{ mM}^{-1}\text{s}^{-1}\text{Gd}^{-1}$ , 310 K, 0.47 T).<sup>35</sup> However, these dihydrated metal ions will likely be limited to preclinical studies because of their labile nature.

### **PARACEST MRI**

In the last decade, paramagnetic chemical exchange saturation transfer (PARACEST) agents have been developed for MRI.<sup>66-68</sup> A PARACEST agent is a molecule that has exchangeable protons (for example alcohols, amides and metal-bound water) that are shifted by a paramagnet. Paramagnetic substances such as lanthanide ions are able to shift some exchangeable protons 100 parts per million (ppm) or more.<sup>66-68</sup> Detailed reviews on the

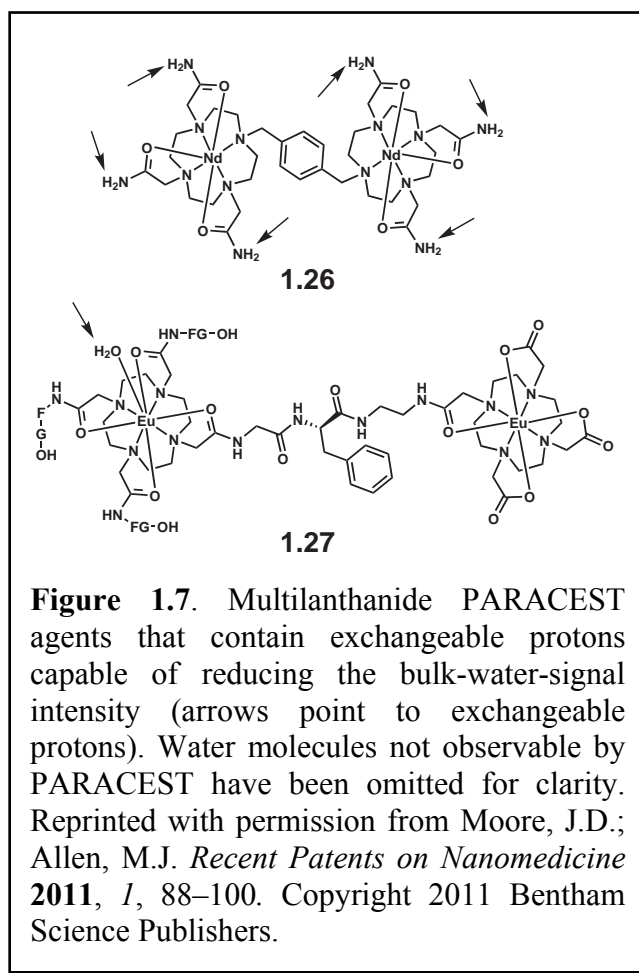
mechanism of PARACEST and lanthanide-based PARACEST agents are available;<sup>66-69</sup> therefore, I will only briefly describe the features of PARACEST agents that are relevant to multilanthanide systems.

PARACEST imaging relies on the exchange of one or more protons from a paramagnetic complex with protons from the bulk water. A PARACEST image is generated by subtracting two maps of bulk-water-peak intensity: a reference map acquired without a presaturation pulse and a map acquired after a presaturation pulse at the resonance frequency of the exchanging protons. The PARACEST image is the difference in bulk-water-peak-intensity between the reference and presaturated maps. Because the PARACEST phenomenon causes a decrease in bulk-water peak intensity, the scale of a PARACEST image represents the degree of bulk-water-peak suppression.

The efficiency of a PARACEST agent is determined by two factors: (1) the proton-exchange rate,  $k_{ex}$ , and (2) the difference between the exchanging-proton and bulk-water chemical shifts,  $\Delta\omega$ .<sup>66-69</sup> For a paramagnetic substance to effectively transfer saturated protons to the bulk water,  $k_{ex}$  should be less than or equal to  $|\Delta\omega|$ .<sup>66-69</sup> Therefore, greater differences in chemical shift (large  $\Delta\omega$ ) allow for faster proton-exchange rates. PARACEST imaging is advantageous compared to  $T_1$ - and  $T_2$ -based MRI because there is no background signal in a PARACEST image. However, like other MR imaging techniques, PARACEST imaging is insensitive and requires a high concentration (mM) of agent to generate satisfactory images. Therefore, an agent with a large number of exchangeable protons is desirable for decreasing the concentration of agent required.<sup>70,71</sup>

Of reported PARACEST agents, only two dimetallic lanthanide complexes fit the category of complexes described in this review. Complex **1.26 (Figure 1.7)** contains 12 amide

protons with chemical shifts that are shifted 12 ppm from the bulk water peak.<sup>72</sup> Although this shift is small and partial overlap with the bulk water peak exists, a PARACEST effect was observed to reduce the bulk water signal by 30% for a 10 mM solution of complex **1.26**.<sup>72</sup> With complex **1.27**, PARACEST is due to the exchange of coordinated and bulk water molecules (**Figure 1.7**).<sup>73</sup> The chemical shift of the coordinated water protons is shifted 45 ppm from the bulk water signal, and a 30% reduction in the bulk-water signal was observed for a 10 mM solution of complex **1.27**.<sup>73</sup> This result is similar to the PARACEST effect observed for a EuDOTA tetra(amide) mononuclear analog,<sup>29</sup> indicating that the effect is not augmented by the presence of the second chelate. A potentially more useful molecule may contain two covalently linked amide-based chelates and, therefore, double the number of exchanging water molecules. These preliminary successes of multilanthanide complexes as PARACEST agents provide proof-of-concept that this class of complexes can be used as PARACEST agents. Further exploration of ligands designed to have more highly shifted exchangeable proton peaks is an important direction of future research in this field. Additionally, water exchange in some multilanthanide complexes has been shown to be slower than their monometallic counterparts studied for  $T_1$ -based MRI. Thus,



we expect that these ligands could be useful for making PARACEST agents with lanthanides other than  $Gd^{3+}$ . The use of these multimeric ligands in PARACEST agents has not been reported, but the water-exchange rates reported for their  $Gd^{3+}$  complexes indicate that their complexes with other lanthanides could be useful as PARACEST contrast agents for MRI. Studies of multilanthanide systems will likely lead to an understanding of how a sufficient chemical shift of a large number of exchangeable protons can be achieved. This understanding has the potential to be applied to macromolecules that contain many exchangeable protons and, therefore, produce highly sensitive PARACEST contrast agents.

### **Multilanthanide-based Luminescent Probes**

While lanthanides other than  $Gd^{3+}$  are used in PARACEST imaging, they also lend themselves to optical imaging. Lanthanides exhibit luminescent behavior that results from 4f electronic transitions.<sup>74</sup> These transitions are Laporte forbidden and result in narrow, low intensity emission bands compared to organic fluorophores. The narrow line width of lanthanide emission peaks generates characteristic emission spectra that enable identification of lanthanide-based probes. Additionally, the lifetimes of lanthanide emissions can be on the order of micro- to milliseconds, much longer than organic molecules including biomolecules.<sup>74-79</sup> These exceptionally long luminescence lifetimes are the key advantage to lanthanide-based probes for medical applications.<sup>74-79</sup> Background autofluorescence from organic biomolecules decays much faster than lanthanide luminescence such that a delay between excitation and detection in an imaging experiment will eliminate non-lanthanide-based background fluorescence. The possibility that zero-background images could be acquired using luminescent lanthanide probes makes their study a worthwhile pursuit to the medical field. Luminescent lanthanide complexes that are responsive to medically relevant biochemical events could become useful diagnostic

probes based on specific molecular-level interactions. Probes based on these interactions have the potential to improve the precision, accuracy, and ease-of-use of diagnostic assays. Further, use of kinetically inert complexes such as those discussed in this review might allow diagnoses *in vivo*.

Multilanthanide complexes with  $\text{Eu}^{3+}$  and  $\text{Tb}^{3+}$  have been studied due to their long luminescence lifetimes (110 to 400  $\mu\text{s}$ ) and their intense emission bands (relative to other lanthanides) in the visible region. For *in vivo* imaging emission in the visible region may be viewed as a limitation due to minimal tissue penetration of emitted wavelengths that require invasive detection methods.  $\text{Yb}^{3+}$  complexes emitting in the near-IR region have also been reported to address the issue of improving the tissue depth at which luminescence can be detected.<sup>80</sup> However, due to the similar coordination chemistry throughout the lanthanide series, the study of  $\text{Eu}^{3+}$  and  $\text{Tb}^{3+}$  complexes is necessary to determine many structural parameters and provide proof-of-concept for detecting a response. Other lanthanides are typically not strong emitters and have not been reported multilanthanide complexes for these applications, presumably for this reason.

### *Ligand Design*

Although considerations to prevent lanthanide toxicity using polydentate chelates are necessary for luminescent probes, three other factors also must be considered for the design of multilanthanide complexes for luminescence-related applications. First, OH and NH oscillators are efficient quenchers of  $\text{Ln}^{3+}$  luminescence; therefore, to preserve long  $\text{Ln}^{3+}$  luminescent lifetimes, polydentate chelates must not contain OH or NH oscillators in the inner coordination sphere of the metal ion.<sup>75-77,81</sup> Second, the low quantum efficiency of  $\text{Ln}^{3+}$  ions can be improved with ligands containing organic fluorophores (antennas) that absorb and transfer energy to  $\text{Ln}^{3+}$

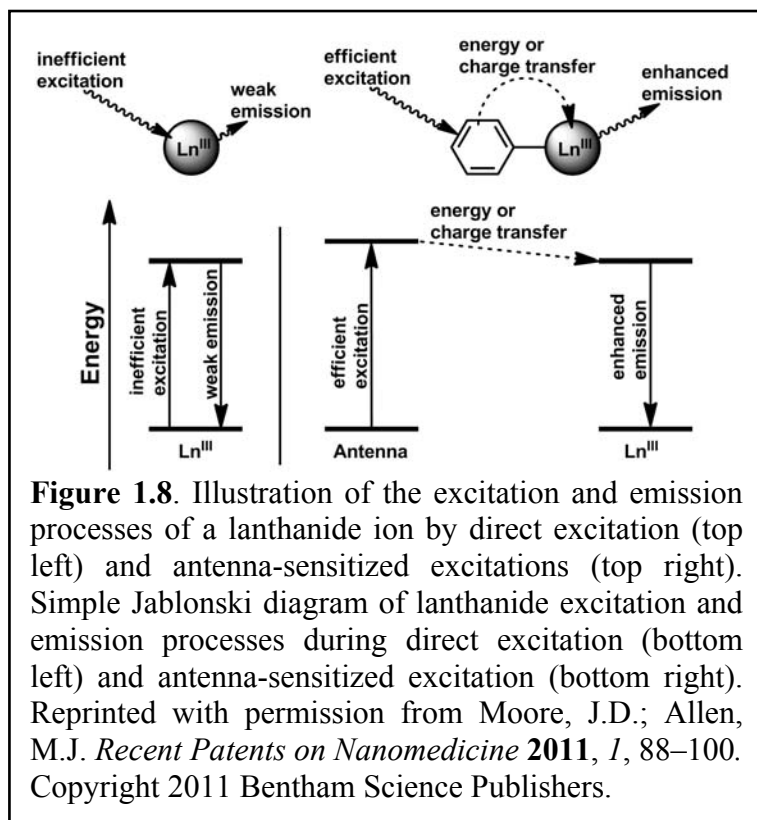
excited states.<sup>75-77,81,82</sup> Third, without interactions with substrates, luminescent lanthanide complexes have little use in medicine; therefore, ideally, the emission intensity or wavelength will change upon the interaction of a substrate with the complex.  $\text{Ln}^{3+}$  ions are strong Lewis acids and are capable of binding to a wide variety of anions; however, useful sensing applications require that binding be specific, which requires control of the  $\text{Ln}^{3+}$  coordination sphere through judiciously designed ligands. Alternatively, a complex can be designed to bind to an analyte of interest and detection can take place after unbound complex has been washed or diffused away. This strategy has not been reported for multilanthanide systems and represents an unexplored area of future research.

The synthesis of multimeric ligands tends to be more challenging than the synthesis of monomeric ligands; however, the sensitivity of  $\text{Ln}^{3+}$  luminescent probes can be increased by a simple additive effect when multiple  $\text{Ln}^{3+}$  ions are present in one complex. Another possible advantage of multilanthanide complexes is  $\text{Ln}^{3+}$ -sensitized luminescence.<sup>80</sup> In these systems, interactions at each lanthanide can be interrogated separately for ratiometric sensing, wherein the response of the probe can be determined without determining the concentration of the probe.<sup>83</sup> Further, some multilanthanide complexes are known to display different properties than their monometallic analogs such as a response to or cleavage of DNA and RNA for reasons that are not well understood.<sup>48,83,84</sup> Yet, while the study of interactions between multilanthanide luminescent probes and DNA is still in its infancy, this class of compounds has the potential to generate useful tools for gene sensing or for therapy in the medical field.

### *Antennas*

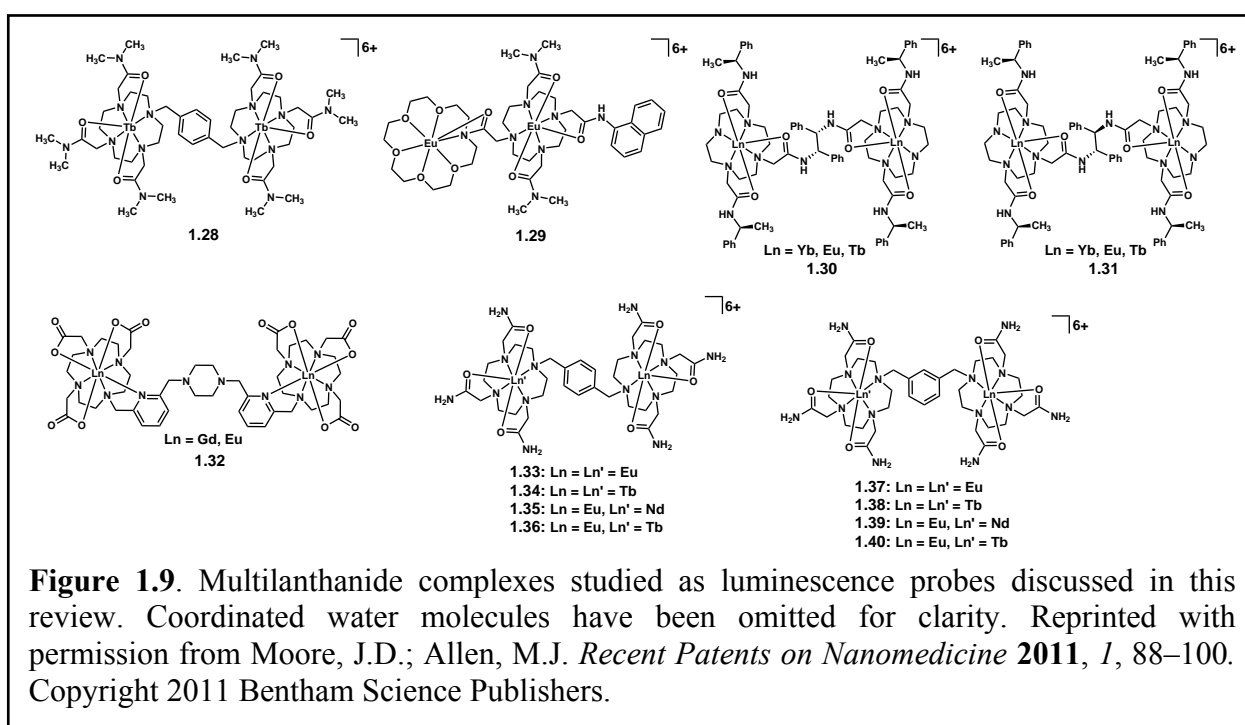
Ligands appended with organic fluorophores improve the quantum yield of lanthanide complexes. This improvement is due to more efficient excitation of the chromophore relative to

direct excitation of the lanthanide, as illustrated in **Figure 1.8**. The specific processes involved in the transfer of energy from the ligand excited state to the lanthanide excited state depend on the relative energies of the donor and acceptor states and detailed reviews of this phenomenon are available elsewhere.<sup>75,77,78,81</sup> Nearly all multilanthanide complexes synthesized for medical sensing



applications contain an antenna in the linker (**Figure 1.9**). Complexes **1.28** and **1.30–1.40** contain aromatic groups that function as antennas within these linkers.<sup>83–87</sup> The efficiency of energy transfer depends in part on the  $\text{Ln}^{3+}$ –antenna distance; therefore, antennas that coordinate to the  $\text{Ln}^{3+}$  ion such as the pyridyl ligands in **1.32** are expected to better sensitize  $\text{Ln}^{3+}$  emission than those that transfer energy through space. An additional requirement for the antenna is that the excited energy state must be higher than the  $\text{Ln}^{3+}$  excited state and must be sufficiently higher in energy to prevent back energy transfer. Therefore, the antenna excited state should lie at least  $1200\text{ cm}^{-1}$  above the emissive lanthanide excited state.<sup>88</sup> Many conjugated systems other than those shown in **Figure 1.9** could be used as antennas as long as the excited-state energy level of the antenna is matched to the lanthanide. Due to the wide variety of possible antenna-lanthanide combinations, the study of multilanthanide luminescent probes is expected to expand

in the future. Another interesting observation in multilanthanide luminescent probes is that a single fluorophore is capable of sensitizing two  $\text{Ln}^{3+}$  ions as demonstrated in complexes **1.28** and **1.33–1.40**.<sup>83–85</sup> The knowledge gained from studying how multiple lanthanide ions are sensitized by a single antenna is likely to indicate how macromolecular systems can be designed with multiple lanthanide ions excited by a single antenna. This type of design would be advantageous over multiple-antenna-containing systems by minimizing the complexity of the macromolecular structure.



### Luminescence Sensing

Adding functionality to multilanthanide complexes brings additional complexity to the design and synthesis of multimeric ligands. The majority of multilanthanide luminescent probes have been synthesized with tetraamide chelates (**Figure 1.9**). Tetraamide chelates are strong Lewis acids that are potentially useful as anion sensors due to strong binding to negatively charged substrates relative to their neutral counterparts. Dimetallic lanthanide complexes are of

particular interest because they have been reported to exhibit different anion-binding characteristics than their monometallic analogs.<sup>83,84</sup> Sensing anions may be useful in determining ion concentrations, which can be indicators of metabolism and homeostasis in cells, and understanding cellular processes may facilitate identification of cellular abnormalities that could be used to understand and diagnose disease. For example, complexes **1.28–1.31** and **1.33–1.36** bind anions such as phosphates and dicarboxylates through Lewis acid–Lewis base interactions.<sup>83–85,87,89</sup> Alternatively, the sensing of cations, especially toxic species such as  $\text{Hg}^{\text{II}}$ , is of interest for determining contaminant levels *in vivo* and *ex vivo*. For this reason, complex **1.32** was studied, and it was found to show a change in luminescence in the presence of the  $\text{Hg}^{\text{II}}$  cation.<sup>86</sup> The luminescence response is due to the pyridyl groups that leave the  $\text{Ln}^{3+}$  coordination sphere to bind to  $\text{Hg}^{\text{II}}$ .<sup>86</sup> Of all substrates that have been studied with multilanthanide complexes, perhaps the most intriguing and potentially useful to the medical field is DNA. Complex **1.39** was reported to show luminescence changes in the presence of DNA.<sup>83</sup> This exciting result indicates that the development of gene-specific medical assays may be possible. However, how the interaction with DNA is effected by the structural characteristics of complex **1.39** is not well understood. While further investigation of the interaction of DNA with **1.39** is underway, studies exploring DNA-binding with new multilanthanide complexes will be useful to elucidate the structural features that are responsible for the DNA interaction.

As mentioned, sensitizing multiple  $\text{Ln}^{3+}$  ions using one fluorophore has been demonstrated.<sup>83–85</sup> While double  $\text{Ln}^{3+}$  sensitization is fundamentally interesting, it could be especially useful with heterometallic complexes. Hetero-multimetallic complexes would be ideal for ratiometric sensing where one  $\text{Ln}^{3+}$  emission remains constant while the others change in response to a substrate. Ratiometric sensing would eliminate the need to know the concentration

of the probe, making *in vivo* analysis of substrates such as cations, anions, and DNA possible where the probe concentration is unknown.

### **Literature Summary**

The study of multilanthanide complexes is a necessary endeavor in pursuit of advanced medical diagnostics. Substantial contributions have been made to the fields of MRI and luminescence imaging by studying multilanthanide complexes. Continued study of these complexes will facilitate our understanding of the fundamental relationship between chemical structure and imaging properties. This knowledge is needed to enable the rational design of optimized complexes for medical applications. These complexes will likely contribute to the field of medical imaging in the form of ultra-high field contrast agents for MRI, activatable probes for MRI, and luminescent *in vivo* molecular imaging for personalized medicine.

### **Research Approach**

While considerable effort has been exerted in studying multilanthanide systems with the complexes shown above, there were only a few examples where the distance between lanthanide ions was within what is required for Ln–Ln interactions (through space dipole–dipole interactions are a function of the inverse distance to the sixth power and orbital coupling essentially requires that the ions be touching or bridged). Though many examples of bridged lanthanide complexes are reported, few have been studied for and satisfy the aqueous stability requirements necessary for medical applications. There was also a lack of understanding and focus on the cumulative effects of binding two lanthanides within a few angstroms of each other, though extensive work in solid-state and extended-solid systems has been published on Ln–Ln interactions. The absence of an available system to probe the effects of inter-lanthanide distance and study the properties of bridged complexes in an aqueous environment, where novel

properties may be especially useful, lead me to design and synthesize a new ditopic ligand and corresponding lanthanide complexes.

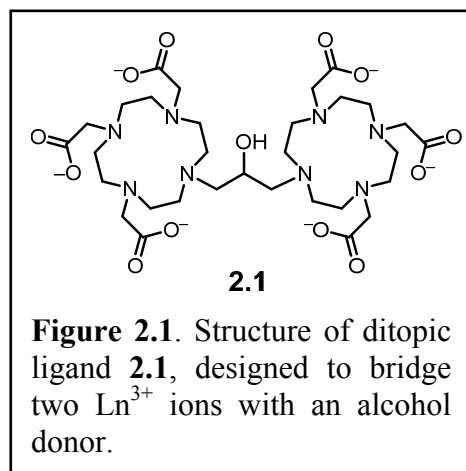
In Chapter 2, I will illustrate the important features of the ligand and discuss the rationale behind the ligand design that lead me to expect that aqueous-stable, bridged, dimetallic lanthanide complexes could be generated with this ligand. I will also discuss the expected properties and potential applications of the resulting complexes that guided my selection of lanthanide ion used in the complexes I have made. In Chapter 3, I will present the luminescence behavior of the  $\text{Eu}^{3+}$  complex pertaining to pH-sensing applications along with optimized structures and a possible mechanism of pH-response. Chapter 4 will describe further structural analyses of dimetallic lanthanide complexes and the discovery of intramolecular lanthanide-lanthanide energy transfer phenomena. In Chapter 5, I will summarize the results reported in the Chapters 2–4 and relate these results to previously reported dimetallic complexes mentioned in Chapter 1. I will also discuss the potential applications of this work for sensing and imaging applications. I will conclude in Chapter 6 by discussion the impact that these results may have on our fundamental understanding of and future work on aqueous lanthanide-based systems, particularly in dimetallic and multimetallic lanthanide complexes. Finally, I will close with a few suggestions for future experiments and alterations to the ligand for new dimetallic lanthanide complexes.

## CHAPTER 2: Ligand Design and Synthetic Attempts

### Ligand Design

The structure of the ligand I designed is based on several considerations. First, the potential applications of the resulting metal complexes would require kinetic and thermodynamic stability. Second, the study of lanthanide–lanthanide (Ln–Ln) interactions would require a close proximity for metal binding sites. Third, the position of an alcohol between the binding sites would facilitate a bridge between the  $\text{Ln}^{3+}$  ions, leading to unique properties (relative to monometallic complexes) in a discrete dimetallic complex. The combination of these considerations led me to propose a ligand containing two 1,4,7,10-tetraazacyclododecane-1,4,7-triyl)triacetate (DO3A) moieties bridged by a 2-propanolyl linker (**Figure 2.1**).

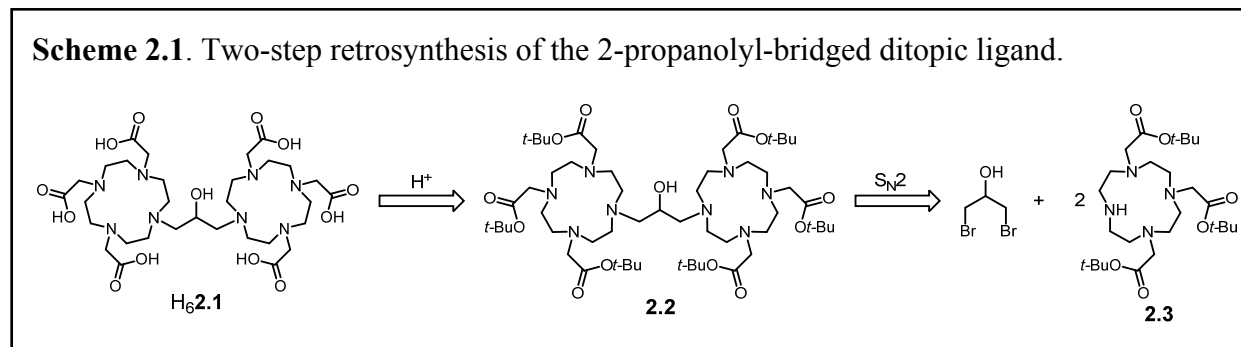
The ligand is composed of three components: cyclen macrocycles, carboxylate arms, and a 2-propanolyl linker. Cyclen-based polyaminopolycarboxylate chelates take advantage of the chelate and macrocyclic effects to generate highly kinetically and thermodynamically stable complexes with  $\text{Ln}^{3+}$  ions.<sup>2, 3, 39</sup> Though cyclen has been functionalized with many substituents containing



functional groups that coordinate to lanthanides,<sup>34, 44, 47, 48, 86</sup> often called ‘arms’, carboxylates were chosen because they are known to be the strongest-binding organic donors and give the ligand and overall charge of  $-6$ , which results in a neutral complex when bridging two  $\text{Ln}^{3+}$  ions if the alcohol remains protonated. Finally, because  $\text{Ln}^{3+}$  prefer coordination within a five-membered ring, the choice of a 2-propanolyl linker places an alcohol donor in an ideal position to form fused five-membered rings with two  $\text{Ln}^{3+}$  ions, facilitating a desired alcohol bridge.

## Synthetic Approach

My initial retrosynthetic analysis of **2.1** suggested that a two-step synthetic route could yield the desired product (**Scheme 2.1**). The first reaction would require two nucleophilic



substitutions to 1,3-dibromo-2-propanol with commercially available DO3A-tris-*tert*-butyl ester, **2.3**, generating protected ligand **2.2**. The *tert*-butyl ester protecting groups could be removed from **2.2** with trifluoroacetic acid to yield H<sub>6</sub>**2.1**. The experimental conditions for the first reaction were varied, and a list of the attempted conditions is described in **Table 2.1**; however, no evidence for the formation of the desired product **2.2** was observed by thin layer chromatography (TLC), NMR spectroscopy, or mass spectrometry. Mass analysis of the reaction mixtures listed in **Table 2.1** revealed that a possible side reaction was occurring after one substitution of 1,3-dibromo-2-propanol to yield a species with 571 *m/z* through an unknown mechanism (**Scheme 2.2**). I hypothesized that the formation of these side products could be limited by reducing the reaction temperature; however, only a trace amount of **2.2** was detected when the reaction was carried out at ambient temperature. The second substitution likely requires a higher temperature to overcome steric interference caused

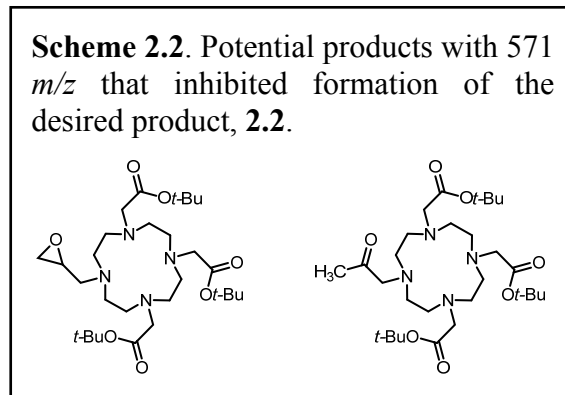


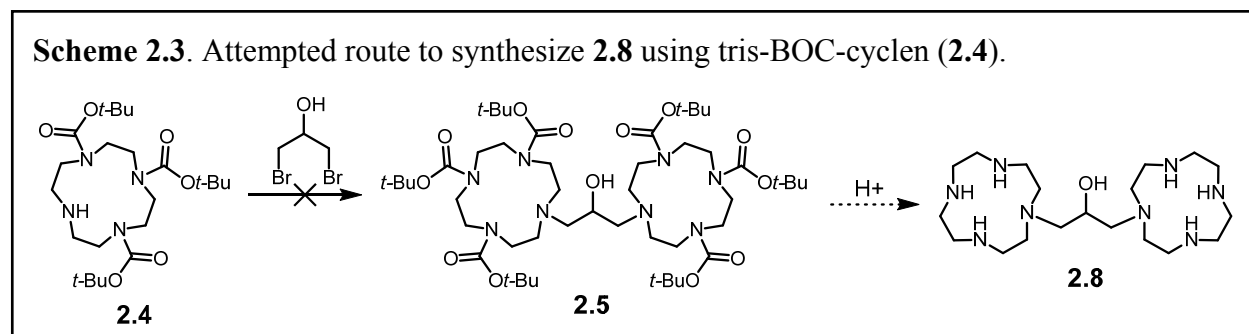
Table 2.1. Experimental conditions for attempts to synthesize 2.2.

Notebook Page	Electrophile	Base*	Solvent	Temperature (°C)	Time	Notes
JDMII_055	1,3-dibromo-2-propanol	TEA	CH <sub>3</sub> CN	22	30 m	no product observed
JDMII_055	1,3-dibromo-2-propanol	TEA	CH <sub>3</sub> CN	82	2 h	no product observed
JDMII_061	1,3-dibromo-2-propanol	TEA	DMSO	82	120 h	no product observed
JDMII_075	1,3-dibromo-2-propanol	DIEA	CH <sub>3</sub> CN	82	72 h	no product observed
JDMII_087	1,3-dibromo-2-propanol	Cs <sub>2</sub> CO <sub>3</sub>	CH <sub>3</sub> CN	55	72 h	no product observed
JDMII_091	1,3-dibromo-2-propanol	Cs <sub>2</sub> CO <sub>3</sub>	CH <sub>3</sub> CN	82	360 h	no product observed
JDMII_112	1,3-dibromo-2-propanol	K <sub>2</sub> CO <sub>3</sub>	CH <sub>3</sub> CN	22	24 h	no product observed
JDMII_112	1,3-dibromo-2-propanol	K <sub>2</sub> CO <sub>3</sub>	CH <sub>3</sub> CN	72	26 h	no product observed
JDMII_117	1,3-dibromo-2-propanol	Cs <sub>2</sub> CO <sub>3</sub>	CH <sub>3</sub> CN	22	24 h	trace product observed
JDMII_134	1,3-dibromo-2-propanol	NaHCO <sub>3</sub>	CH <sub>3</sub> CN	82	24 h	no product observed
JDMII_145	epichlorohydrin	Na <sub>2</sub> CO <sub>3</sub>	CH <sub>3</sub> CN	72	168 h	trace product observed
JDMIII_067_A	1,3-dibromo-2-propanol	none	CH <sub>3</sub> CN	22	24 h	no product observed
JDMIII_067_B	1,3-dibromo-2-propanol	none	CHCl <sub>3</sub>	22	24 h	no product observed
JDMIII_067_C	1,3-dibromo-2-propanol	none	1:1 CHCl <sub>3</sub> /H <sub>2</sub> O	22	24 h	no product observed
JDMIII_109	1,3-dichloroacetone	K <sub>2</sub> CO <sub>3</sub>	CH <sub>3</sub> CN	22	5 m	electrophile decomposed
JDMIII_123	1,3-dibromoacetone	K <sub>2</sub> CO <sub>3</sub>	CH <sub>3</sub> CN	22	10 m	electrophile decomposed

\*TEA = triethylamine, DIEA = di-isopropylethylamine

by the first macrocycle; consequently, I modified my proposed synthesis to account for this limitation. In my second and third synthetic attempts (**Scheme 2.3** and **2.4**, respectively), I used more compact macrocycles in an attempt to reduce steric interference in the second substitution. I reasoned that less steric interference would enable the use of lower temperatures and minimize side reactions. The following syntheses also represent a shift in strategy toward adding the carboxylate arms after forming the propanolyl-bridged di-cyclen skeleton, **2.8** (**Scheme 2.3**).

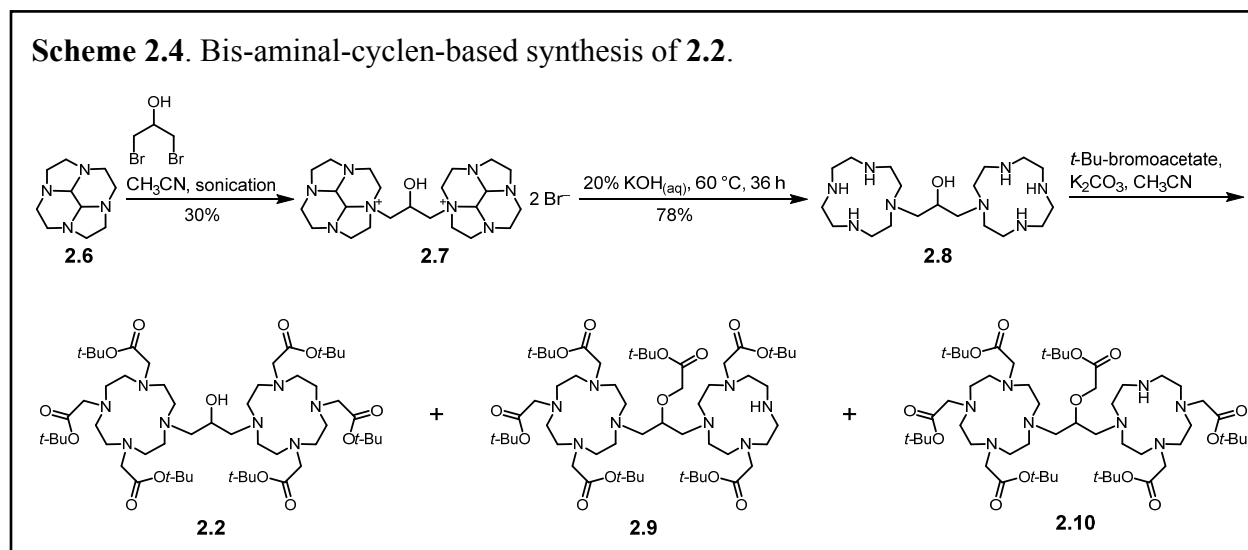
One less-hindered cyclen-containing nucleophile that I used was (1,4,7-tris-butoxycarbamate)1,4,7,10-tetraazacyclododecane (**2.4**), illustrated in **Scheme 2.3**. Due to the decreased steric bulk of the *tert*-butoxycarbamate (BOC) protecting groups compared to the *tert*-butyl acetate arms, the reaction between **2.4** and 1,3-dibromo-2-propanol was expected to proceed at lower temperature than with **2.3**, potentially reducing the elimination side reaction. However, the desired product, **2.5**, was not observed at ambient temperature or upon heating at reflux in acetonitrile, and the elimination product was observed after heating.



A more successful approach to making the bis-cyclen propanol skeleton, **2.8**, was via the reaction of *cis*-decahydro-2a,4a,6a,8a-tetraazacyclopentacenaphthylene (**2.6**) with 1,3-dibromo-2-propanol (**Scheme 2.4**). The reaction proceeded at ambient temperature in acetonitrile to form a di-ammonium bromide salt that precipitated from the reaction mixture and could be isolated by filtration. This result was expected based on the work of Le Baccon and coworkers who reported similar reactions with other alkyl dibromides.<sup>90a</sup> Deprotection of **2.7** was carried out in 20%

aqueous KOH by heating to 60 °C for 3 days.<sup>90b</sup> Isolation of pure **2.8** was achieved by direct extraction of the reaction solution with chloroform. Alkylation of **2.8** was attempted under multiple conditions with a range of bases, solvents, alkylating agents, and temperatures. In general, reactions carried out at temperatures between 20 and 45 °C resulted in incomplete alkylation. Reactions carried out at higher temperatures resulted in over alkylation. The over-alkylated products were not separable from **2.2**. More importantly, observation of a seven-arm product forced me to consider that the alcohol might be alkylated, possibly producing **2.9** and **2.10** (Scheme 2.4). Therefore, I had no way of knowing whether the observed six-arm product was the result of alkylation at the six secondary amine positions or at five secondary amines and the alcohol. Despite my initial assumption that *O*-alkylation was unlikely, the structures of the six-arm products **2.2**, **2.9**, and **2.10** could not be deconvoluted or positively identified. Subsequently, I devised several approaches to mask the alcohol so that only the *N*-alkylated product could be obtained, which I will describe in the next three sections.

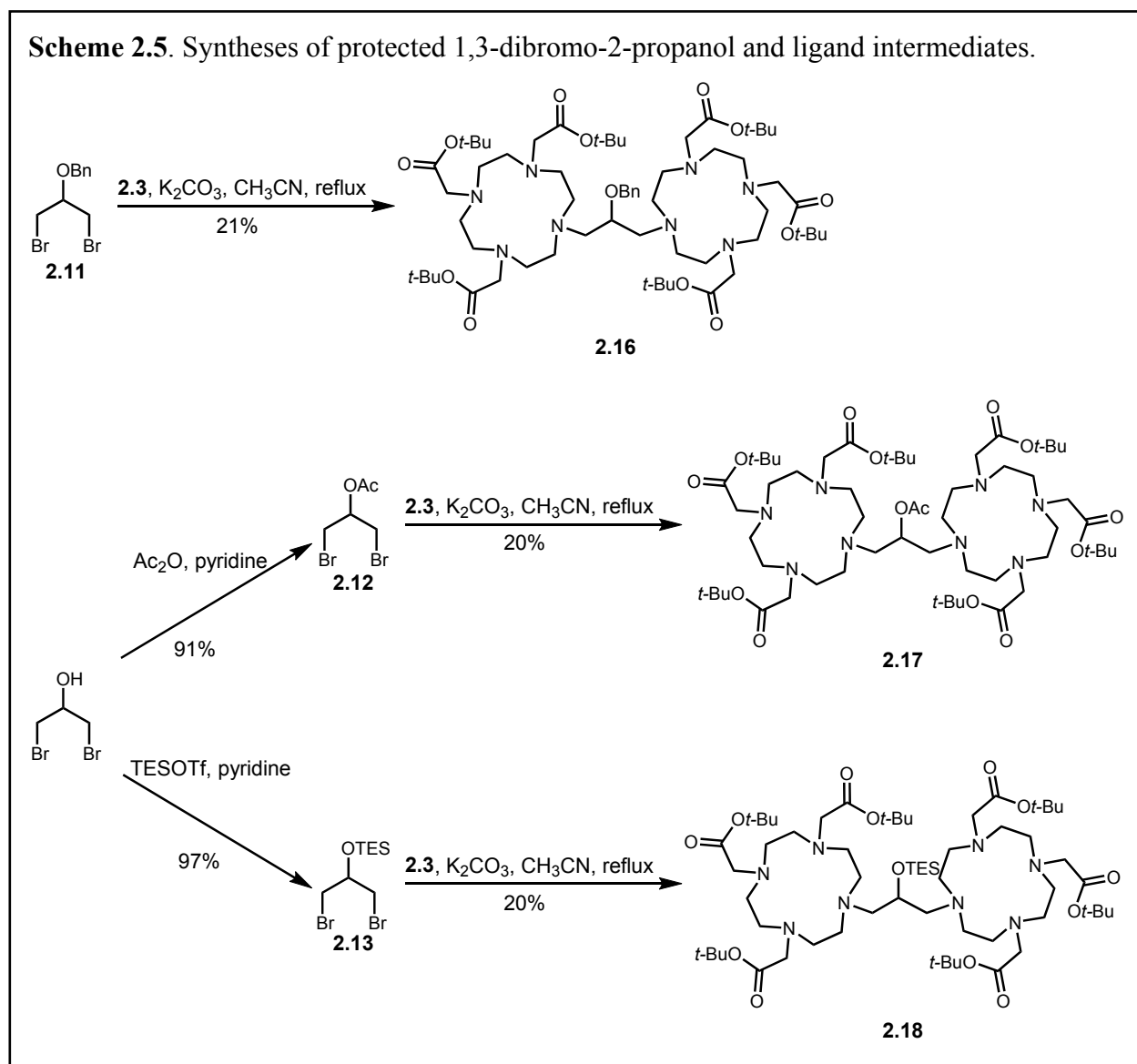
### Selective *O*-protection



I considered the C–N bonds from the cyclen moieties to the propanol bridge to be the key bonds for the formation of ligand **2.1**. Therefore, it appeared that compound **2.8**, in which those bonds were already formed, would be the most viable starting point. However, selective protection of the alcohol in the presence of six secondary amines posed a significant challenge due to the nucleophilicity of the amines. Thus, I first attempted to mask the alcohol using the tetrahydropyranyl protecting group that can be installed under acid-catalyzed conditions. To achieve an acidic solution of compound **2.8**, approximately 10 equivalents of acid were required. Adding this amount of acid resulted in the precipitation of the protonated form of **2.8** from solvents including CH<sub>3</sub>CN, CHCl<sub>3</sub>, MeOH, EtOH, and tetrahydrofuran, with which the protecting group reagent, dihydropyran (DHP), is miscible. In retrospect, I think this reaction might be possible in dimethylformamide (DMF) or dimethylsulfoxide (DMSO) where both DHP and the salt of **2.8** might be soluble.

I also attempted selective *O*-protection with trimethylsilyl chloride (TMSCl) because silylamide moieties are labile and can be removed during a workup. I found isolation of the trimethylsilylether to be impossible, and I could not detect such a product with mass spectrometry or NMR spectroscopy. Attempts to treat compound **2.8** with TMSCl immediately followed by *tert*-butylbromoacetate under basic conditions were unsuccessful in yielding protected ligand **2.2** or its TMS ether derivative. At this point, it was clear that continuing to use compound **2.8** as an intermediate would require a more complex strategy to prevent *O*-alkylation—global protection, selective *O*-deprotection, orthogonal *O*-protection, and selective *N*-deprotection might be necessary. While exploring this iterative protecting group strategy, I synthesized three precursors—**2.11**, **2.12**, and **2.13**—to protected ligand **2.2** by protecting 1,3-

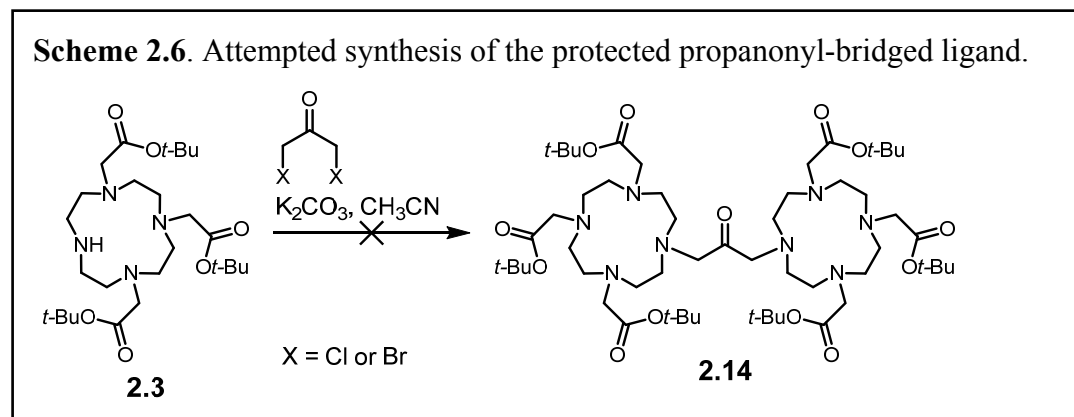
dibromo-2-propanol (**Scheme 2.5**). Although the iterative strategy might have been successful, the success of less convoluted routes caused me to abandon the iterative approach.



### Propanone as an Alternative Bridge

In a simultaneous effort to remove the possibility of side reactions, I attempted to bridge two DO3A moieties using a 2-propanonyl bridge (**Scheme 2.6**). There were several reasons to consider this strategy: first, the halo-carbon sites of 1,3-dihaloacetone were expected to be more electrophilic than those of 1,3-dihalo-2-propanol; second, the methyne carbon and alcohol

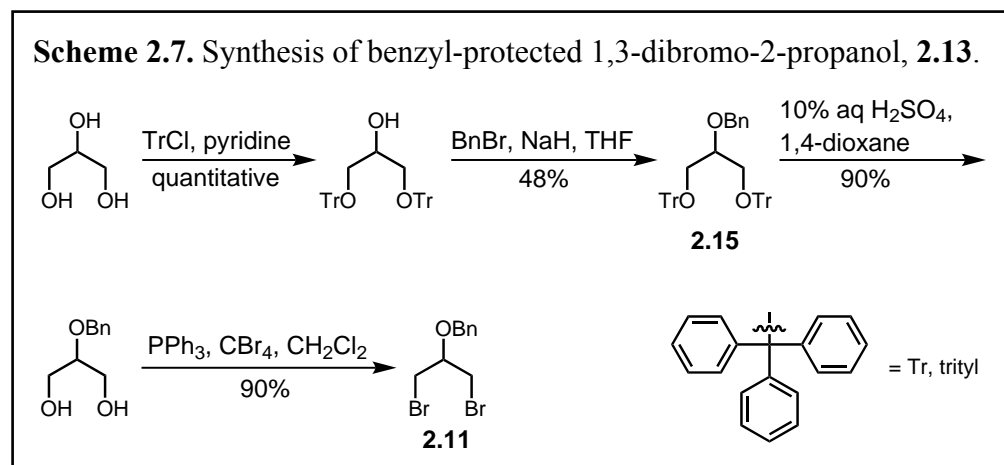
oxygen atoms involved in side product formation from 1,3-dibromo-2-propanol are masked in the ketone analog; and third, like alcohols, ketones are known to coordinate to lanthanides. To install such a bridge, I reacted 1,3-dichloroacetone or 1,3-dibromoacetone with protected DO3A, **2.3**, under basic conditions. The reaction mixtures immediately turned dark brown upon addition of either 1,3-dihaloacetone to **2.3**. The desired product **2.14** could not be detected by mass spectrometry despite the consumption of the electrophile. Due to this surprising result, I exposed 1,3-dichloroacetone and 1,3-dibromoacetone to a series of bases, including nucleophilic ( $\text{NH}_4\text{OH}$ ,  $\text{H}_2\text{O}$ , **2.3**, and **2.4**) and non-nucleophilic (TEA, DIEA, and  $\text{K}_2\text{CO}_3$ ) examples. In each case, the reaction mixture turned brown and the ketone was consumed. These results suggested that dihaloacetones were unstable in the presence of base and could not be used to successfully form **2.14**. Therefore, this method and any other approaches to synthesize **2.14** were not pursued further.



### Protecting Dibromopropanol Prior to Alkylation

After searching for a protecting group that could mask the alcohol during alkylation, I suspected that a benzyl ether was the only protecting group that could withstand the harsh conditions used to convert **2.7** to **2.8**. Installation of the benzyl group directly on 1,3-dibromo-2-propanol was not possible, and the 1,3-dibromo-2-propylbenzylether needed to be synthesized in

four steps (**Scheme 2.7**).<sup>91</sup> After using trityl groups to protect the primary alcohols of glycerol, the secondary alcohol was protected as a benzyl ether, yielding **2.15**. Trityl deprotection followed by bromination yielded the desired 1,3-dibromo-2-propylbenzylether, **2.11**. The reactions in **Scheme 2.4** were repeated, substituting **2.11** for 1,3-dibromo-2-propanol. Over alkylation of **2.8** was observed, but the desired protected ligand, **2.16**, was isolated. However, Pd-catalyzed hydrogenation of the benzyl ether was unsuccessful. Simultaneous hydrolysis of the benzyl ether and the six *tert*-butyl ester groups with HBr produced an uncharacterizable black tar. This result, coupled with the success of other routes, caused me to abandon the synthesis of an *O*-protected bis-cyclen skeleton in favor of protecting-group methods described in the following section.



### Revisiting the 2.3 Nucleophile

The goal of the previous methods was to avoid the elimination product that hampered the route using **2.3** to substitute 1,3-dibromo-2-propanol. However, with the 1,3-dibromo-2-propylbenzylether in hand, I reacted it with **2.3** to probe the effect of the protecting group on the outcome of the reaction with respect to elimination. Though the elimination product was detected, the desired product was produced in sufficient quantity to isolate. This success was surprising because I had supposed that adding a protecting group to the alcohol would increase

the steric bulk around the electrophilic sites and thereby hinder the substitution reaction. Based on my experiments with 1,3-dibromo-2-propylbenzylether, the presence of an *O*-protecting group on 1,3-dibromo-2-propanol has little impact on substitution reactions at the adjacent carbon atoms. Therefore, I synthesized a series of 1,3-dibromo-2-propanol derivatives containing protecting groups that could be more easily removed than the benzyl group.

One such protecting group was the acetate ester, which was easily installed under mildly basic conditions using acetic anhydride to yield **2.14** (**Scheme 2.5**). However, the acyl group was prone to acyl transfer to **2.3** during the subsequent reaction, resulting in low yields of **2.17** and challenging purification. Elimination was also observed with the acyl protecting group. Because the side reaction was still competing with substitution, I explored electron-donating protecting groups rather than electron-withdrawing groups. The most electron-donating protecting groups for alcohols are silyl ethers. The trimethylsilyl ether decomposed during alkylation of **2.3**, but the triethylsilyl (TES) ether proved to be robust enough to withstand the alkylation and purification conditions to yield the desired protected ligand, **2.18**, in 20% yield after purification by chromatography (**Scheme 2.5**). Though the yield did not improve relative to using **2.14**, the TES protecting group made purification easier due to the lack of acetylated **2.3**.

## Experimental Procedures

Commercially available chemicals were of reagent-grade purity or better and were used without further purification unless otherwise noted. Water was purified using a PURELAB Ultra Mk2 water purification system (ELGA). Tri-*tert*-butyl-2,2',2''-(1,4,7,10-tetraazacyclododecane-1,4,7-triyl)triacetate (**2.3**) was prepared according to a published procedure.<sup>92</sup> (1,4,7-tris-butoxycarbamate)1,4,7,10-tetraazacyclododecane (**2.4**) was purchased (Macrocyclics Inc.) and used without further purification. *Cis*-decahydro-2a,4a,6a,8a-tetraazacyclopentacenaphthylene (**2.6**) was prepared according to a published procedure.<sup>90a</sup> [[2-bromo-1-

(bromomethyl)ethoxy)methyl]-benzene (**2.11**) was prepared according to a published procedure.<sup>91</sup> [(1,3-Dibromopropan-2-yl)oxy]triethylsilane (**2.13**) and {[1,3-di(DO3A-*tert*-butyl ester)-2-yl]oxy}triethylsilane (**2.18**) were prepared according to the procedures listed in Chapter 3 for compounds **3.2** and **3.3**, respectively.<sup>93</sup>

Flash chromatography was performed using silica gel 60, 230–400 mesh (EMD Chemicals). Analytical thin-layer chromatography (TLC) was carried out on ASTM TLC plates precoated with silica gel 60 F<sub>254</sub> (250 μm layer thickness). TLC visualization was accomplished by charring with potassium permanganate stain (3 g KMnO<sub>4</sub>, 20 g K<sub>2</sub>CO<sub>3</sub>, 5 mL 5% w/v aqueous NaOH, 300 mL H<sub>2</sub>O) or by charring with ceric ammonium molybdate stain (4 g cerium(IV) sulfate hydrate complex with sulfuric acid, 100 g ammonium molybdate tetrahydrate, 900 mL H<sub>2</sub>O, 100 mL concd H<sub>2</sub>SO<sub>4</sub>). A sonicator (Fisher FS60H) cooled with a homemade heat-exchanger to maintain ambient temperature was used for ultrasonic agitation.

<sup>1</sup>H NMR spectra were obtained using a Varian Unity 400 (400 MHz) spectrometer, and <sup>13</sup>C NMR spectra were obtained using a Varian Unity 400 (101 MHz) spectrometer. Chemical shifts are reported relative to residual solvent signals (CDCl<sub>3</sub>: <sup>1</sup>H: δ 7.26, <sup>13</sup>C: δ 77.23; H<sub>2</sub>O: <sup>1</sup>H: δ 4.79; H<sub>2</sub>O/CH<sub>3</sub>CN: <sup>1</sup>H: δ 4.79, <sup>13</sup>C: δ 1.30; CD<sub>3</sub>CN: <sup>1</sup>H: δ 1.94, <sup>13</sup>C: 1.30). <sup>1</sup>H NMR data are assumed to be first order, and the apparent multiplicity is reported as “s” = singlet, “d” = doublet, “quin” = quintet, and “m” = multiplet. Italicized elements are those that are responsible for the shifts. High-resolution electrospray ionization mass spectra (HRESIMS) were obtained using an electrospray time-of-flight high-resolution Waters Micromass LCT Premier XE mass spectrometer.

8a,8a''-(2-hydroxypropane-1,3-diyl)bis(decahydro-2H-2a,4a,6a,8a-tetraazacyclopenta-acenaphthylenium) bromide (**2.7**): A solution of **2.6** (584.7 mg, 3.010 mmol, 2.2 equiv) and 1,3-

dibromo-2-propanol (298.1 mg, 1.369 mmol, 1.0 equiv) in anhydrous acetonitrile (5.5 mL) was prepared and sonicated at ambient temperature under Ar. A pale brown solid slowly precipitated over the course of the reaction. After 15 days, the reaction mixture was filtered through Whatman #1 filter paper. The precipitate was washed with acetonitrile ( $5 \times 15$  mL). The precipitate was transferred to a flask and trace solvent was removed under reduced pressure, yielding 245.2 mg (30%) of **2.7** as a pale brown solid.  $^1\text{H}$  NMR (400 MHz,  $\text{D}_2\text{O}$ ,  $\delta$ ): 2.38–2.50 (m, 4H), 2.68–2.93 (m, 10H), 3.11–3.24 (m, 7H), 3.43–4.15 (m, 18H), 4.91–4.99 (m, 1H).

1,3-di(1,4,7,10-tetraazacyclododecan-1-yl)propan-2-ol (**2.8**): A solution of KOH (20% aqueous, 25 mL) and **2.7** (524.1 mg, 0.8642 mmol) was heated to 60 °C. After 72 h, the solution was cooled to ambient temperature, filtered, and extracted with  $\text{CHCl}_3$  ( $3 \times 25$  mL). The organic layers were combined, dried over  $\text{MgSO}_4$ , filtered, and concentrated under reduced pressure, yielding 270.9 mg (78%) of **2.8** as a white solid.  $^1\text{H}$  NMR (400 MHz,  $\text{D}_2\text{O}$ ,  $\delta$ ): 2.47–2.87 (m,  $\text{CH}_2$ , 36H), 3.73–3.81 (m,  $\text{CH}$ , 1H);  $^{13}\text{C}$  NMR (101 MHz,  $\text{D}_2\text{O}/\text{CH}_3\text{CN}$ ,  $\delta$ ): 43.8 ( $\text{CH}_2$ ), 45.0 ( $\text{CH}_2$ ), 45.5 ( $\text{CH}_2$ ), 53.1 ( $\text{CH}_2$ ), 59.5 ( $\text{CH}_2$ ), 57.9 ( $\text{CH}$ ); HRESIMS ( $m/z$ ):  $[\text{M} + \text{H}]^+$  calcd for  $\text{C}_{19}\text{H}_{44}\text{N}_8\text{O}$ , 401.3716; found, 401.3707.

1,3-dibromopropan-2-yl acetate (**2.12**): A solution of 1,3-dibromo-2-propanol (1.0 mL, 2.2 g, 0.010 mol, 1.0 equiv), acetic anhydride (9.5 mL, 1.0  $\times$  10 g, 0.10 mol, 10 equiv), and anhydrous pyridine (8.1 mL, 7.9 g, 0.10 mol, 10 equiv) was stirred at ambient temperature under Ar. A precipitate formed after 1 h. After 3 h, the reaction mixture was filtered, concentrated to ~5 mL under reduced pressure, and purified by silica gel chromatography (9:1 hexanes/ethyl acetate) to yield 2.31 g (91%) of **2.12** as a colorless liquid.  $^1\text{H}$  NMR (400 MHz,  $\text{CDCl}_3$ ,  $\delta$ ): 2.13 (s, 3H,  $\text{COOCH}_3$ ), 3.60–3.61 (d,  $J = 5.4$ , 4H,  $\text{CH}_2\text{Br}$ ), 5.10–5.16 (quin,  $J = 5.4$ , 1H,

CH<sub>2</sub>CHCH<sub>2</sub>); <sup>13</sup>C NMR (101 MHz, CDCl<sub>3</sub>, δ): 21.0 (CH<sub>3</sub>), 31.56 (CH<sub>2</sub>), 170.0 (CO); TLC: R<sub>f</sub> = 0.48 (9:1 hexanes/ethyl acetate).

{[1,3-di(DO3A-*tert*-butyl ester)-2-yl]oxy}benzyl ether (**2.16**): A mixture of **2.3** (100.0 mg, 0.1943 mmol, 2.2 equiv), **2.11** (27.2 mg, 0.088 mmol, 1.0 equiv), and K<sub>2</sub>CO<sub>3</sub> (61.0 mg, 0.442 mmol, 5 equiv) in anhydrous acetonitrile (5 mL) under Ar was heated at 65 °C. After 72 h, the reaction mixture was cooled to ambient temperature and filtered through Whatman 4 paper to remove inorganic solids. The filtrate was concentrated under reduced pressure leaving a viscous yellow residue. The residue was dissolved in CHCl<sub>3</sub> (2 mL) and purified by silica gel chromatography (9:1 CHCl<sub>3</sub>/MeOH) to yield 20.8 mg (21%) of **2.16** as an off-white solid. <sup>1</sup>H NMR (400 MHz, CDCl<sub>3</sub>, δ): 1.23–1.47 (m, CH<sub>3</sub>, 54H), 2.23–3.43 (m, 47H), 4.60–4.63 (m, 4H), 7.18–7.35 (m, phenyl CH); <sup>13</sup>C NMR (101 MHz, CDCl<sub>3</sub>, δ): 24.1–28.4 (m, CH<sub>3</sub>), 45.9–59.9 (m, CH<sub>2</sub>), 55.8 (CH), 82.6 (C(CH<sub>3</sub>)<sub>3</sub>), 82.9 (C(CH<sub>3</sub>)<sub>3</sub>), 126.6, 127.3, 126.4, 170.7, 172.6; TLC: R<sub>f</sub> = 0.36 (9:1 CHCl<sub>3</sub>/MeOH).

{[1,3-di(DO3A-*tert*-butyl ester)-2-yl]oxy}acetyl ester (**2.17**): A mixture of **2.3** (1.132 g, 2.200 mmol, 2.2 equiv), **2.12** (259.9 mg, 1.000 mmol, 1.0 equiv), and K<sub>2</sub>CO<sub>3</sub> (691.1 mg, 5.000 mmol, 5.0 equiv) in anhydrous acetonitrile (10 mL) under Ar was heated at 70 °C. After 72 h, the reaction mixture was cooled to ambient temperature and filtered through Whatman 4 paper to remove inorganic solids. The filtrate was concentrated under reduced pressure leaving a viscous yellow residue. The residue was dissolved in CHCl<sub>3</sub> (5 mL) and purified by silica gel chromatography (stepwise gradient CHCl<sub>3</sub> to 85:15 CHCl<sub>3</sub>/MeOH to MeOH) to yield 237.4 mg (21%) of **2.17** as an off-white solid. <sup>1</sup>H NMR (400 MHz, CD<sub>3</sub>CN, δ): 1.15–1.60 (m, CH<sub>3</sub>, 54H), 1.91–3.74 (m, 51H), 5.31–5.48 (m, CH, 1H); <sup>13</sup>C NMR (101 MHz, CD<sub>3</sub>CN, δ): 22.1 (CH<sub>3</sub>),

27.8–28.3 (m, CH<sub>3</sub>), 48.0–54.0 (m, CH<sub>2</sub>), 58.3 (CH), 56.9–58.7 (CH<sub>2</sub>), 82.8–83.2 (m), 172.2, 173.9, 174.6; TLC:  $R_f$  = 0.24 (9:1 CHCl<sub>3</sub>/MeOH).

### Expected Applications

A fused-ring configuration bridging two Ln<sup>3+</sup> ions would be advantageous from the standpoint of generating a contrast agent for MRI with a di-Gd<sup>3+</sup> complex because the Gd–H vectors would be locked together, eliminating the detrimental effects of internal motion on relaxivity. With the internal motion eliminated, the rotational correlation time of the complex would be strictly a function of the hydrodynamic radius of the complex, which was expected to be greater than that of monometallic complexes. This bridged, dimetallic platform may also allow the effects of metal–metal distance on important parameters such as the electronic relaxation times ( $T_{1e}$  and  $T_{2e}$ ) to be probed in a bridged environment, which could then be compared to previously reported, distance-only systems.<sup>refs</sup> A necessary feature of contrast agents for MRI is the presence of an exchangeable water molecule bound to the Gd<sup>3+</sup> ion.<sup>1999</sup>  
caravan chem. rev Gadolinium(III) is 9 coordinate in nearly all examples with similar ligands. As such, I expected that each Gd<sup>3+</sup> ion chelated by **2.1** would contain one bound water molecule. However, as I will detail in Chapter 3, luminescence-decay measurements indicated that there were no water molecules coordinated to the Eu<sup>3+</sup> analog. Given this result, I did not pursue further studies on the contrast-enhancing behavior of Gd<sub>2</sub>**2.1**.

The alcohol bridge forced by this ligand might also provide a highly shifted, exchangeable proton that would allow complexes with lanthanides other than Gd<sup>3+</sup> to be used as paramagnetic chemical exchange saturation transfer (PARACEST) agents. However, after many PARACEST experiments in a variety of water-containing solvent systems, no suppression of the bulk water signal was observed. A likely reason for this result is that the proton-exchange rate

was too rapid, at the pH of my measurements, for a separate proton signal to be observed on the NMR time-scale. A fast exchange rate should be expected for a bridging alcohol because the  $pK_a$  of the alcohol proton should be lowered by coordinating the oxygen to two  $\text{Ln}^{3+}$  ions. The data presented in Chapter 3 suggested that the  $pK_a$  was substantially lower than that of an unbound alcohol, corroborating my explanation.

In addition to magnetic imaging properties, many lanthanides exhibit fluorescent and phosphorescent behavior under irradiation from UV or visible light. The luminescence spectrum and lifetime (or decay-rate) of a complex can be used to approximate symmetry and determine water-coordination number, and luminescent  $\text{Ln}^{3+}$  complexes also offer potential use as optical imaging probes. After finding that the  $\text{Ln}_2\mathbf{2.1}$  complexes were shielded from water, which is often advantageous for  $\text{Ln}^{3+}$ -based luminescent probes, I began to explore the luminescence properties of  $\text{Eu}_2\mathbf{2.1}$ . One hypothesis I developed was that the luminescence-decay rate of  $\text{Eu}_2\mathbf{2.1}$  would depend on the protonation state of the bridging alcohol. Therefore, the luminescence-decay rate could be used as a readout of pH. In Chapter 3, I describe the testing of this hypothesis.

### CHAPTER 3: Concentration-Independent pH Detection with a Luminescent Dimetallic Eu<sup>3+</sup>-Based Probe

Adapted with permission from Moore, J.D.; Lord, R.L.; Cisneros, G.A.; Allen, M.J. *J. Am. Chem. Soc.* **2012**, *134*, 17372–17375. Copyright 2012 American Chemical Society.

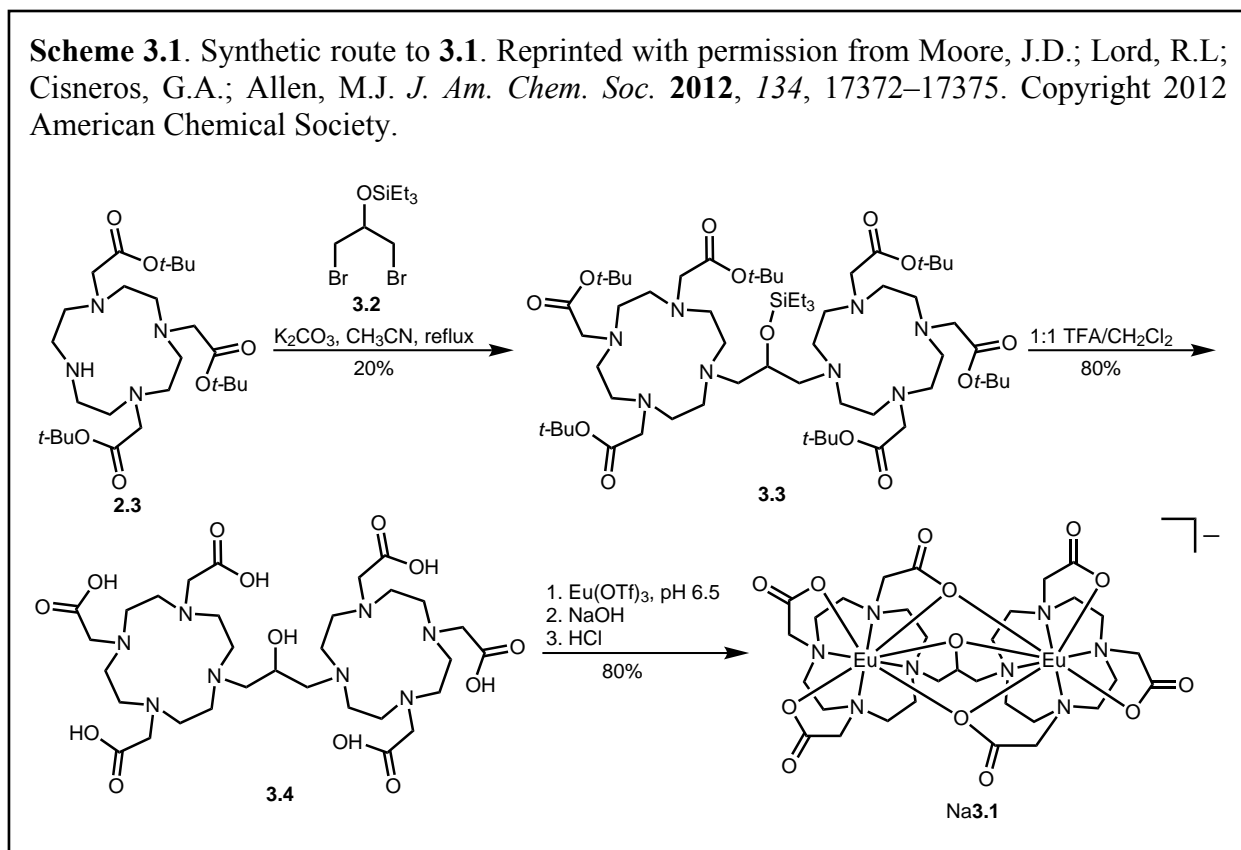
#### Introduction

Molecular imaging with fluorescence microscopy is a powerful tool in biochemical and biomedical research. Organic fluorescent probes that respond to the presence of specific molecular analytes are limited by photobleaching, broad emission bands (~100 nm), small Stokes shifts (<20 nm), and short-lived emissions (<100 ns). Lanthanide-based probes overcome many of the limitations associated with organic fluorophores because they offer atomic-based emissions that do not photobleach, emit line-like bands (<20 nm bandwidth), have large Stokes shifts, and exhibit long luminescence lifetimes (ms). Due to these advantages, many examples of lanthanide-based probes have been reported for the detection of biologically important cations,<sup>94</sup> anions,<sup>95</sup> neutral species,<sup>96</sup> proteins and peptides,<sup>97</sup> and DNA.<sup>98</sup> Many of these probes rely on the ratio of two emission peaks to determine analyte concentration, but the luminescence-decay rate of Eu<sup>3+</sup>-containing complexes should enable the determination of analyte concentration without knowledge of probe concentration or extinction coefficient. Reports describing time-resolved microscopy,<sup>99</sup> luminescence-lifetime imaging,<sup>100</sup> and phosphorescence-quenching microscopy<sup>101</sup> demonstrate that luminescence-decay rates can be determined from microscopy and are, therefore, a useful parameter for sensing applications. Lanthanide-based probes often exhibit low sensitivity that can be addressed by the use of antennae or through the use of multimetallic complexes that increase sensitivity additively.<sup>102</sup> In targeting the multimetallic strategy, I synthesized a new dimetallic Eu<sup>3+</sup>-containing complex, **3.1**, that responds to pH over a physiologically relevant range of 4 to 8 by a new mechanism, based on luminescence-decay

rates, that is independent of the probe concentration and selective for only proton concentration. To my knowledge, no system of this type has been reported to respond to pH by luminescence-decay rate.

I hypothesized that bridging two  $\text{Eu}^{3+}$  ions with an alcohol would decrease electron density on the bridging oxygen and increase the acidity of the alcohol compared to an uncoordinated alcohol. I anticipated that the acid–base equilibrium of the bridging oxygen would result in a pH-dependent change in the luminescence-decay rate because the luminescence-decay rate of  $\text{Eu}^{3+}$  increases with the number of hydroxyl oscillators coordinated to the metal ion.<sup>103</sup> I expected this change to be independent of the concentration of **3.1** because luminescence-decay rate is not dependent on metal concentration. Further, I expected that this mechanism would be selective for protons because hydroxyl oscillators have the correct vibrational energy levels to efficiently quench  $\text{Eu}^{3+}$  luminescence. Here, I present the synthesis, characterization, and spectroscopic and computational analyses of dimetallic  $\text{Eu}^{3+}$ -containing complex **3.1**. Additionally, I propose a mechanism for the pH-dependent luminescence-decay rate supported by our experimental and computational data.

My complex design incorporates two  $\text{Eu}^{3+}$ -containing 2,2',2''-(1,4,7,10-tetraazacyclododecane-1,4,7-triyl)triacetate complexes bridged by an *iso*-propanol linker that is positioned to form two *ortho*-fused five-membered rings containing the two metal ions. The synthesis of **3.1** was completed in four steps (**Scheme 3.1**). Briefly, 1,3-dibromo-2-propanol was converted to triethylsilyl ether **3.2**, which was used to alkylate two equivalents of 1,4,7,10-tetraazacyclododecane-1,4,7-tris(*tert*-butyl acetate) yielding the protected ligand **3.3**. I found it imperative that the alcohol be protected for the success of this alkylation. Ligand **3.4** was obtained by global deprotection of **3.3** with trifluoroacetic acid (TFA), and  $\text{Eu}^{3+}$  complexation



was achieved by addition of an aqueous solution of  $\text{Eu}^{3+}$  trifluoromethanesulfonate (OTf) to ligand **3.4** at pH 6.5. Dialysis yielded dimetallic  $\text{Eu}^{3+}$ -containing complex **3.1**. A xylenol orange test indicated that there was no unchelated  $\text{Eu}^{3+}$  ions present at pH 5.8 even after storing in solution at ambient temperature for 24 h.<sup>104</sup>

### Experimental Procedures

Commercially available chemicals were of reagent-grade purity or better and were used without further purification unless otherwise noted. Water was purified using a PURELAB Ultra Mk2 water purification system (ELGA). Tri-*tert*-butyl-2,2',2''-(1,4,7,10-tetraazacyclododecane-1,4,7-triyl)triacetate (DO3A-*tert*-butyl ester) was prepared according to a published procedure.<sup>92</sup>

Flash chromatography was performed using silica gel 60, 230–400 mesh (EMD Chemicals). Analytical thin-layer chromatography (TLC) was carried out on ASTM TLC plates

precoated with silica gel 60 F<sub>254</sub> (250 μm layer thickness). TLC visualization was accomplished by charring with potassium permanganate stain (3 g KMnO<sub>4</sub>, 20 g K<sub>2</sub>CO<sub>3</sub>, 5 mL 5% w/v aqueous NaOH, 300 mL H<sub>2</sub>O) or by charring with ceric ammonium molybdate stain (4 g cerium(IV) sulfate hydrate complex with sulfuric acid, 100 g ammonium molybdate tetrahydrate, 900 mL H<sub>2</sub>O, 100 mL concd H<sub>2</sub>SO<sub>4</sub>).

<sup>1</sup>H NMR spectra were obtained using a Varian Unity 400 (400 MHz) spectrometer, and <sup>13</sup>C NMR spectra were obtained using a Varian Unity 400 (101 MHz) spectrometer. Chemical shifts are reported relative to residual solvent signals (CDCl<sub>3</sub>: <sup>1</sup>H: δ 7.26, <sup>13</sup>C: δ 77.23; H<sub>2</sub>O: <sup>1</sup>H: δ 4.79). <sup>1</sup>H NMR data are assumed to be first order, and the apparent multiplicity is reported as “t” = triplet, “q” = quartet, “quin” = quintet, and “m” = multiplet. Italicized elements are those that are responsible for the shifts. High-resolution electrospray ionization mass spectra (HRESIMS) were obtained using an electrospray time-of-flight high-resolution Waters Micromass LCT Premier XE mass spectrometer.

[(1,3-Dibromopropan-2-yl)oxy]triethylsilane (**3.2**): To a solution of 1,3-dibromopropan-2-ol (3.0 mL, 6.4 g, 0.030 mol, 1 equiv), pyridine (4.8 mL, 4.6 g, 59 mmol, 2 equiv), and anhydrous dichloromethane (290 mL) under Ar at 0 °C was added triethylsilyl trifluoromethanesulfonate (12 mL, 15 g, 55 mmol) at a rate of 3 mL/h via syringe pump. The resulting reaction mixture was allowed to warm to ambient temperature after 6 h at 0 °C. Stirring was continued at ambient temperature for 2 h. Volatiles were removed under reduced pressure, and the resulting residue was purified by silica gel chromatography (hexanes) to yield 9.45 g (97%) of **3.2** as a colorless oil. <sup>1</sup>H NMR (400 MHz, CDCl<sub>3</sub>, δ): 0.65 (q, *J* = 8.0 Hz, SiCH<sub>2</sub>, 6H), 0.98 (t, *J* = 8.0 Hz, CH<sub>3</sub>, 9H), 3.44–3.54 (m, BrCH<sub>2</sub>, 4H), 4.01 (quin, *J* = 5.2 Hz, CH, 1H); <sup>13</sup>C NMR (101 MHz, CDCl<sub>3</sub>, δ): 5.1 (CH<sub>2</sub>), 7.0 (CH<sub>3</sub>), 35.7 (CH<sub>2</sub>), 71.3 (CH); TLC: *R*<sub>f</sub> = 0.35

(hexanes). Anal. Calcd for  $C_9H_{20}Br_2OSi$ : C, 32.54; H, 6.07; N, 0.00. Found: C, 32.62; H, 5.96; N, 0.00.

{[1,3-Di(DO3A-*tert*-butyl ester)-2-yl]oxy}triethylsilane (**3.3**): A mixture of DO3A-tris-*tert*-butyl ester (10.01 g, 19.43 mmol, 2.2 equiv), **3.2** (2.93 g, 8.83 mmol, 1 equiv), and  $K_2CO_3$  (6.12 g, 0.440 mol, 5 equiv) in anhydrous acetonitrile (80 mL) under Ar was heated at reflux. The reaction mixture turned yellow–brown after 2 h and was stirred at reflux for 72 h. The reaction mixture was cooled to ambient temperature and filtered through Whatman 4 paper to remove inorganic solids. The filtrate was concentrated under reduced pressure leaving a viscous yellow residue. The residue was dissolved in  $CHCl_3$  (80 mL), and the resulting organic phase was washed with saturated aqueous  $NaHCO_3$  ( $3 \times 80$  mL). The organic layer was concentrated under reduced pressure to  $\sim 10$  mL and purified by silica gel chromatography (stepwise gradient  $CHCl_3$  to 9:2  $CHCl_3/MeOH$ ) to yield 2.00 g (20%) of **3.3** as an off-white solid.  $^1H$  NMR (400 MHz,  $CDCl_3$ ,  $\delta$ ): 0.46–0.66 (m,  $SiCH_2$ , 6H), 0.77–0.97 (m,  $CH_2CH_3$ , 9H), 1.16–1.61 (m,  $CH_3$ , 54H), 2.02–4.58 (m, 52H);  $^{13}C$  NMR (101 MHz,  $CDCl_3$ ,  $\delta$ ): 5.6 ( $CH_2$ ), 5.7 ( $CH_2$ ), 5.9 ( $CH_2$ ), 7.0–7.3 (m,  $CH_3$ ), 27.8–28.5 (m,  $CH_3$ ), 49.5–53.0 (m,  $CH_2$ ), 55.7–57.4 (m,  $CH_2$ ), 66.2–66.9 (m, CH), 80.0–83.2 (m), 169.1–171.1 (m), 172.7; TLC:  $R_f = 0.44$  (9:2  $CHCl_3/MeOH$ ); HRESIMS ( $m/z$ ):  $[M + H]^+$  calcd for  $C_{61}H_{119}N_8O_{13}Si$ , 1199.8666; found, 1199.8649.

1,3-Di[1,4,7,10-tetraazacyclododecanyl(1,4,7-triacetate)]propan-2-ol (**3.4**): To a solution of **3.3** (1.58 g, 1.32 mmol, 1 equiv) in  $CH_2Cl_2$  (10 mL) was added a solution of water (0.5 mL) in trifluoroacetic acid (TFA) (10 mL). The resulting solution was stirred for 24 h. The solution was concentrated under reduced pressure, and the resulting residue was dissolved in methanol (2 mL) and added to diethyl ether (11 mL) in a centrifuge tube. The product precipitated as an off-white solid and was centrifuged and washed with diethyl ether ( $5 \times 11$  mL). Solvent was removed

under reduced pressure to yield 1.15 g (80%) of **3.4** • 2.7 TFA • 2 H<sub>2</sub>O. <sup>1</sup>H NMR (400 MHz, D<sub>2</sub>O, 45 °C, δ): 2.75–4.17 (m, CH<sub>2</sub>, 48H), 4.50–4.62 (m, CH, 1H); HRESIMS (*m/z*): [M + Na]<sup>+</sup> calcd for C<sub>31</sub>H<sub>56</sub>N<sub>8</sub>NaO<sub>13</sub>, 771.3865; found, 771.3878; Anal. Calcd for C<sub>31</sub>H<sub>56</sub>N<sub>8</sub>O<sub>13</sub> • 2.7 C<sub>2</sub>HF<sub>3</sub>O<sub>2</sub> • 2 H<sub>2</sub>O: C, 40.01; H, 5.78; N, 10.25. Found: C, 39.76; H, 5.73; N, 10.58.

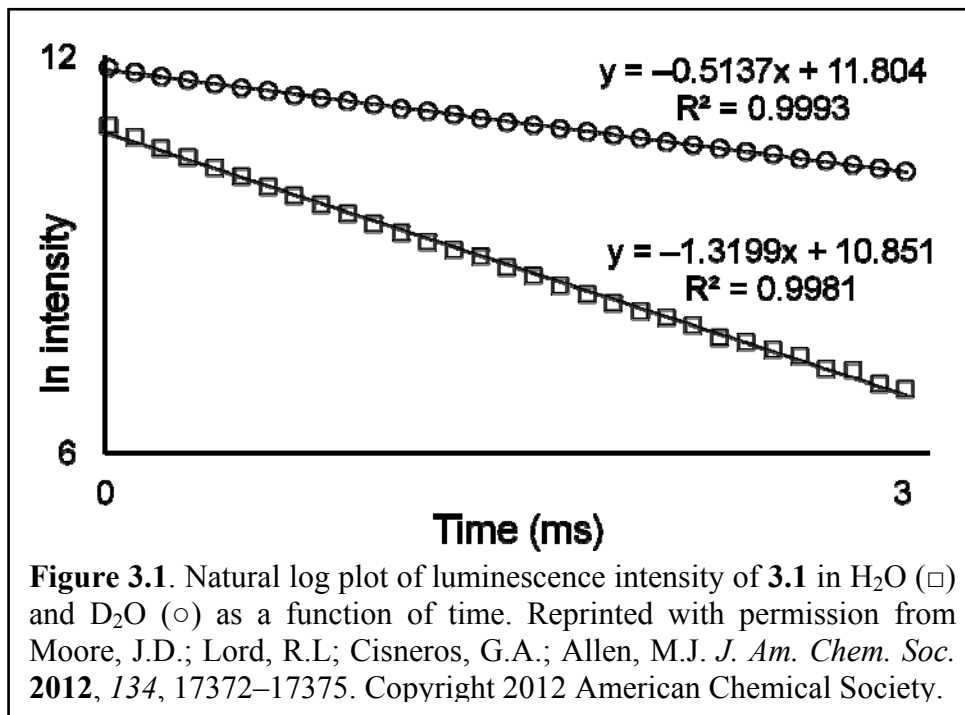
Sodium{1,3-bis[europium(1,4,7,10-tetraazacyclododecanyl(1,4,7-triacetate))]propan-2-oxide} (Na**3.1**): A solution of **3.4** • 2.7 TFA • 2 H<sub>2</sub>O (103 mg, 0.0950 mmol, 1 equiv) in water (10 mL) was adjusted to pH 6.5 with 1 M NaOH. An aqueous solution of Eu(OTf)<sub>3</sub> (5.0 mL, 52 mM, 2.7 equiv) was added to the solution of **3.4**. The pH of the solution was maintained at 6.5 with 1 M NaOH while stirring for 18 h. Upon observation of constant pH for 6 h, the pH of the solution was adjusted to 11 with 1 M NaOH to precipitate excess europium. The solution was filtered through a 0.2 μm syringe filter, neutralized to pH 7 with 1 M HCl, and dialyzed in 500 Da molecular weight cut-off tubing against water. The dialysate was transferred to a vial and concentrated under reduced pressure to yield 107 mg (80%) of Na**3.1** • 0.5 NaOTf • 3 H<sub>2</sub>O as a white solid. HRESIMS (*m/z*): [M]<sup>-</sup> calcd for Eu<sub>2</sub>C<sub>31</sub>H<sub>49</sub>N<sub>8</sub>O<sub>13</sub>, 1043.1816; found, 1043.1830. Anal. Calcd for Eu<sub>2</sub>C<sub>31</sub>H<sub>49</sub>N<sub>8</sub>O<sub>13</sub>Na • 0.5 CF<sub>3</sub>SO<sub>3</sub>Na • 3 H<sub>2</sub>O: C, 31.30; H, 4.58; N, 9.27. Found: C, 31.43; H, 4.81; N, 9.04.

#### *Determination of the q Value of 3.1*

Luminescence-decay measurements were acquired using a HORIBA Jobin Yvon Fluoromax-4 spectrofluorometer in decay by delay scan mode using the phosphorescence lifetime setting. All decay measurements were acquired with a 395 nm excitation wavelength, a 595 nm emission wavelength, excitation and emission slit widths of 5 nm, a flash count of 100, an initial delay of 0.01 ms, a max delay of 3 ms, and a delay increment of 0.1 ms. The natural log plot of the intensity was plotted against time, and the slope was used as the decay rate (**Figure**

**3.1**). The decay rates of **3.1** in H<sub>2</sub>O (pH 5.4) and D<sub>2</sub>O were used in equation 1, which was derived by Horrocks and coworkers to calculate  $q$ .<sup>103</sup> We accounted for quenching due to an inner-sphere hydroxyl oscillator that we expected to be present at pH 5.4 by subtracting the term  $0.45n_{\text{OH}}$ , where  $n=1$ .<sup>103</sup>

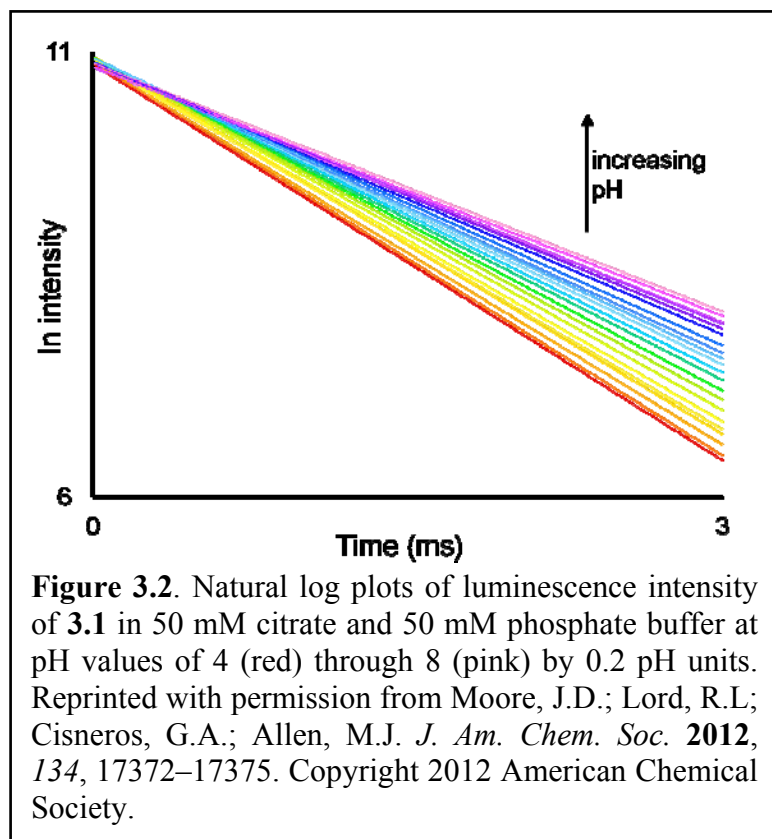
equation 3.1:



#### *Luminescence-Decay Measurements and Spectra of 3.1 at Different pH Values*

Buffer solutions (50 mM citrate and 50 mM phosphate) were prepared from pH 4 to 8 by 0.2 pH units for a total of 21 buffer solutions. Each sample was prepared by mixing **3.1** (18 μL, of a 0.50 or 1.0 mM in water) with buffer (232 μL). The luminescence decay of each sample was measured within 5 minutes of sample preparation. All decay measurements were acquired with a 395 nm excitation wavelength, a 595 nm emission wavelength, excitation and emission slit widths of 5 nm, a flash count of 100, an initial delay of 0.01 ms, a max delay of 3 ms, and a delay increment of 0.1 ms. The natural log plot of the intensity was plotted against time, and the

slope was used as the decay rate. Spectra were acquired on each of the 21 samples with an excitation wavelength of 395 nm, excitation slit width of 5 nm, and emission slit width of 1 nm (Figure 3.2).



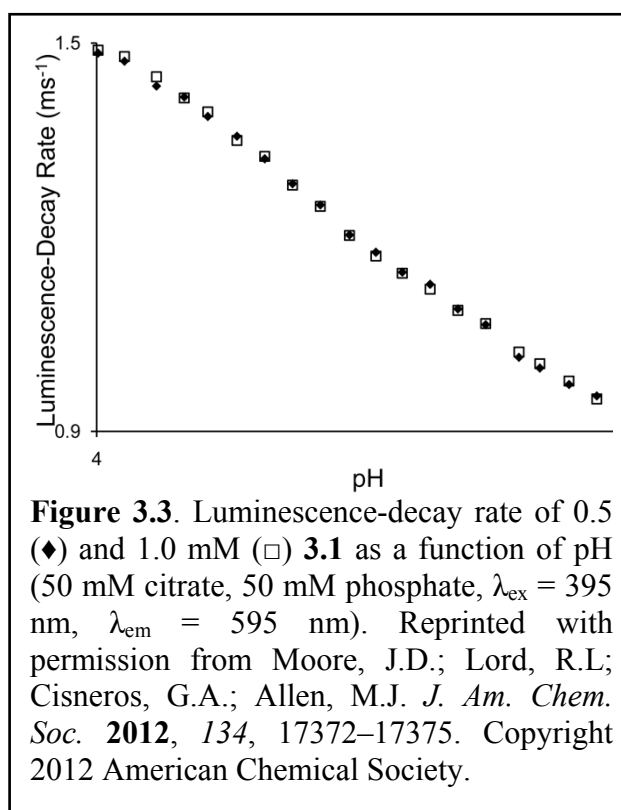
## Results and Discussion

### *Water Coordination Analysis*

To assess the coordination environment of the  $\text{Eu}^{3+}$  ions, the number of water molecules coordinated to the  $\text{Eu}^{3+}$  ion,  $q$ , was determined using the method developed by Horrocks and coworkers.<sup>103</sup> Complex **3.1** was found to have a  $q$  value of 0 in the absence of buffer (pH 5.4), suggesting that no water was bound to the  $\text{Eu}^{3+}$  ions. When I considered possible structures to satisfy this data, I was unable to construct a structure lacking a bridge between  $\text{Eu}^{3+}$  ions that contained no water molecules bound to the  $\text{Eu}^{3+}$  ions. This  $q$  data indicated that the  $\text{Eu}^{3+}$  ions are bridged by an alcohol donor from the ligand. Because coordinated OH oscillators influence the

luminescence-decay rate of  $\text{Eu}^{3+}$  ions, I hypothesized that there would be a decrease in the luminescence-decay rate of **3.1** with increasing pH above 5.4 due to deprotonation of the bridging alcohol.

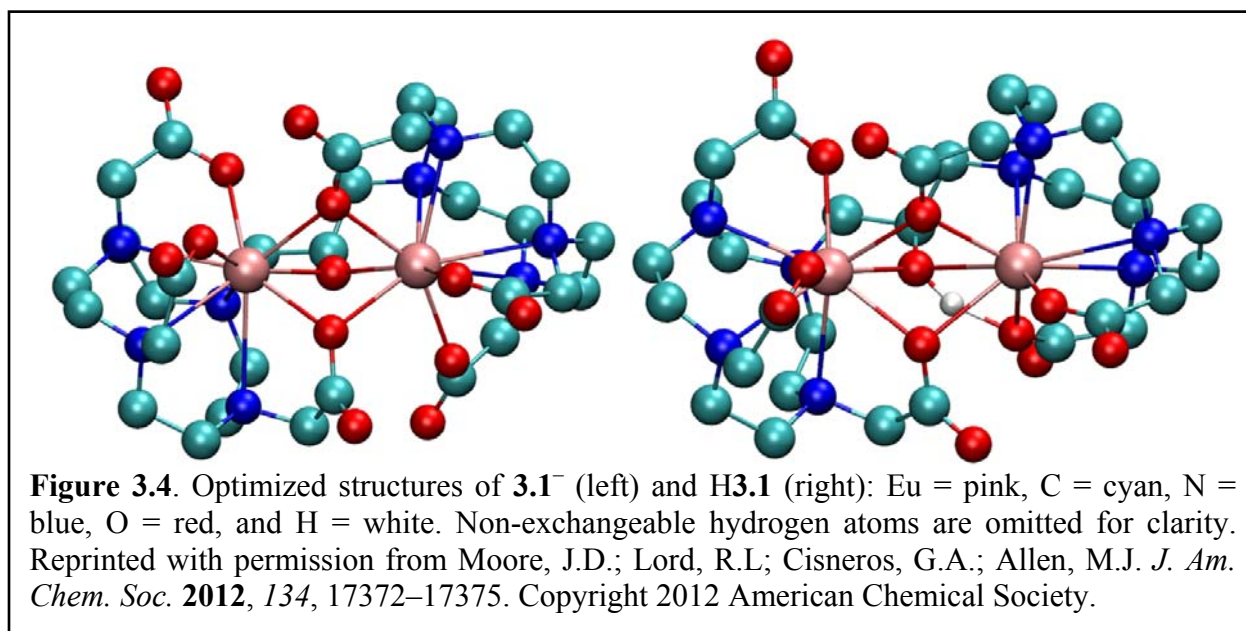
To test this hypothesis, I prepared 0.5 mM solutions of **3.1** in a series of buffers from pH 4.0 to 8.0 in increments of 0.2 pH units. The luminescence-decay rate of each solution was determined and plotted against pH values (**Figure 3.3**). I confirmed that the pH response is independent of the concentration of **3.1** by repeating the luminescence-decay rate measurements with 1 mM solutions of **3.1**. These experiments resulted in identical pH-dependent changes in luminescence-decay rates. The resulting plot supports my hypothesis that the luminescence-decay rate depends on pH and indicates that the pH response extends over a biologically relevant range of 4 to 8. The second derivative of this plot was used to estimate the  $\text{p}K_{\text{a}}$  of the protic source at 5.8, placing the maximum sensitivity of the probe very close to the pH of diseased tissue.<sup>105</sup>



### Optimized Structure Analysis

Structures of  $\text{H3.1}$  and  $\text{3.1}^-$  were optimized with Gaussian 09 at the PBE0/SDDall level (small core for all atoms) using the default convergence criteria.<sup>106</sup> The optimized structures suggest that the alcohol bridges the  $\text{Eu}^{3+}$  ions and that two carboxylate oxygens are also bridging

(**Figure 3.4**). This tri-bridged structure is consistent with a 9-coordinate  $\text{Eu}^{3+}$  environment that is saturated by the ligand and corroborates the luminescence-decay data that indicate the absence of water molecules bound to  $\text{Eu}^{3+}$ . Interestingly, to obtain a suitable initial guess for the optimization, it was necessary to include the two bridging carboxylates. To achieve this, the

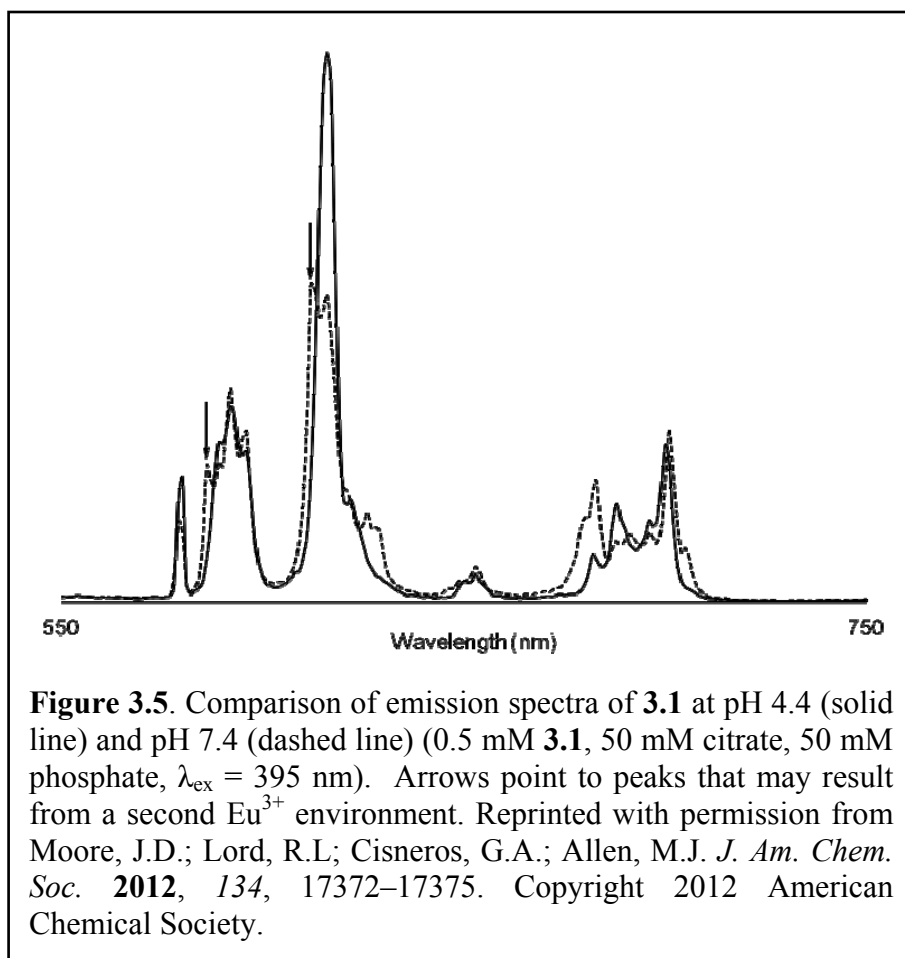


orientation of the carboxylate arms on the two chelates had to be in opposite conformations from each other ( $\Delta$  vs  $\Lambda$ ) to minimize the bridged structure. Further, the steric constraints of the ligand prevent a bridge as small as alkoxide without two bridging carboxylates. These structures corroborate both the exceptionally long luminescence lifetime at higher pH values and the luminescence quenching that results from lowering pH.

### *Emission Spectra*

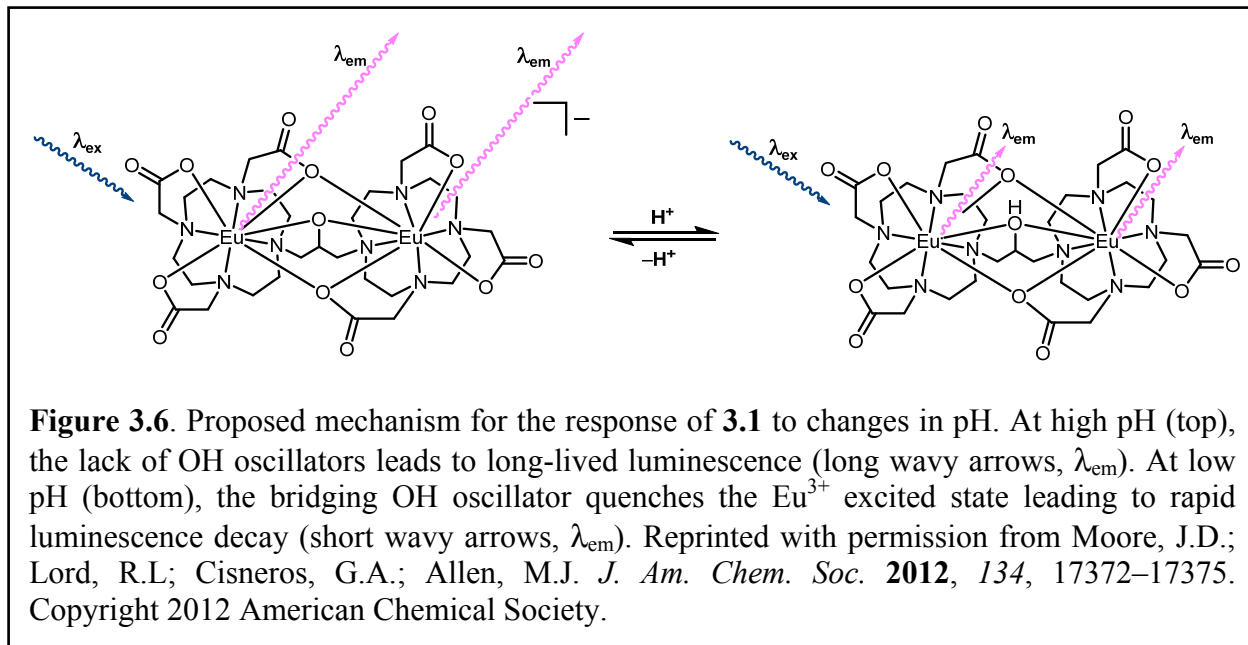
To further elucidate the mechanism of the pH response, I compared the emission spectra of **3.1** at different pH values (**Figure 3.5** and Appendix B, **Figure B.2**). At pH 4.4, I observed that the multiplicity of the  $\Delta J = 1$  manifold (centered at 592 nm) is at the maximum of three peaks. This high multiplicity indicates that the symmetry around the  $\text{Eu}^{3+}$  ions is low. However,

the spectrum would indicate that the symmetry of the left and right chelates is similar because I do not observe greater than  $2J+1$  peaks for any manifold in the spectrum. Surprisingly, the spectrum of **3.1** at pH 7.4 contains four peaks in the  $\Delta J = 1$  manifold and two major peaks in the  $\Delta J = 2$  manifold. The source of these additional peaks at high pH is not immediately obvious. One explanation that is consistent with all other data is that the loss of the intramolecular hydrogen bond at high pH values increases the flexibility of the ligand, resulting in a change in conformation about one or both of the  $\text{Eu}^{3+}$  ions. Previous studies of similar monometallic  $\text{Eu}^{3+}$  complexes by Horrocks and coworkers demonstrated that interconverting isomers can be observed by luminescence spectroscopy.<sup>107</sup>



## Summary and Conclusions

The spectroscopic and computational data suggest a novel mechanism of pH response wherein protonation of the bridging alkoxide under acidic conditions introduces a hydroxyl oscillator in the  $\text{Eu}^{3+}$  coordination sphere (**Figure 3.6**). The inner-sphere hydroxyl oscillator quenches the  $\text{Eu}^{3+}$  excited state resulting in a faster luminescence-decay rate. Further, because coordination of other cations to the alkoxide will not produce oscillators with the proper energy to quench the  $\text{Eu}^{3+}$  emission, I expect that this system will specifically respond to proton concentration. Moreover, this process is reversible such that continuous monitoring of pH is possible. To my knowledge, no other system of this kind has been reported to respond to pH by luminescence-decay rate.



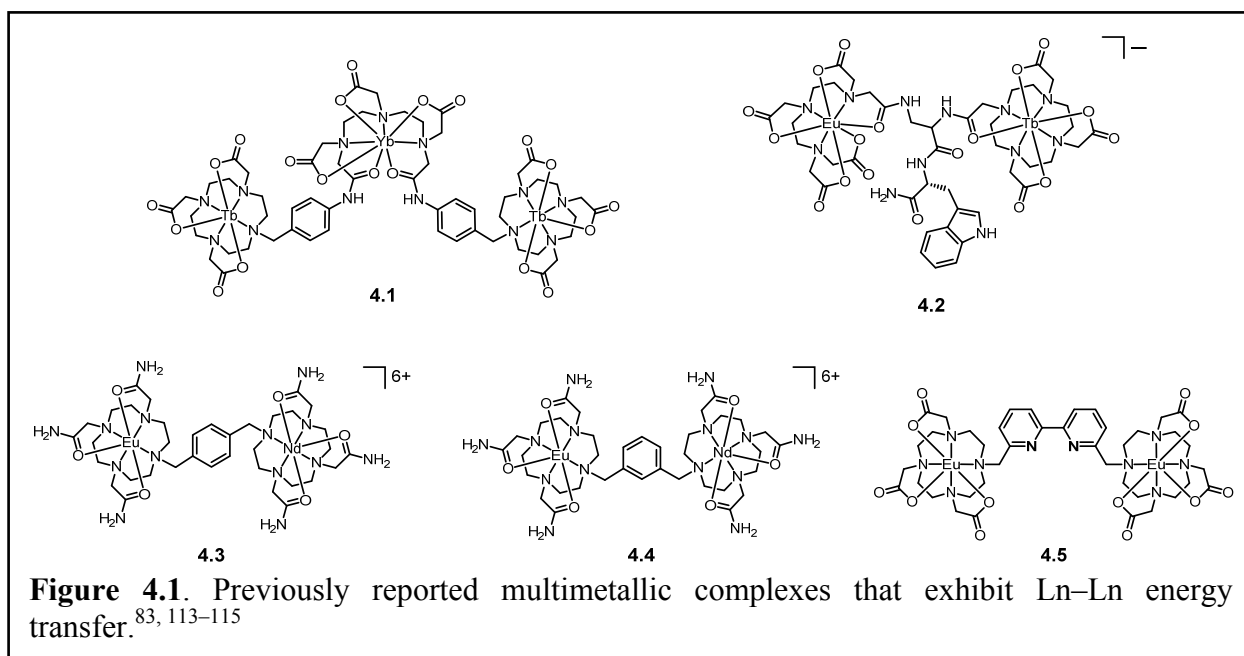
I have demonstrated a concentration-independent luminescence response to pH achieved through the protic equilibrium of an alkoxide in **3.1**. My characterization indicates that the  $\text{Eu}^{3+}$  ions have no coordinated water molecules resulting in relatively slow luminescence-decay rates, especially at pH values above 7. The absence of coordinated water molecules makes this system

less sensitive to changes in the composition of the surrounding media relative to systems that contain coordinated water molecules. Spectral changes with pH are indicative of a change in the coordination sphere in agreement with my proposed mechanism. Computationally optimized structures also are consistent with my experimental observations. Complex **3.1** represents a unique system using a new mechanism by which pH can be detected and offers a useful method for concentration-independent, non-invasive, continuous pH imaging. I expect that this research is a step toward powerful tools for biomedical and biochemical research because pH is often an indicator of disease.

## CHAPTER 4: Tb<sup>3+</sup> to Eu<sup>3+</sup> Energy Transfer in a Heterodimetallic Complex

### Introduction

Lanthanide–lanthanide (Ln–Ln) energy transfer is a well-known phenomenon in extended solids,<sup>108</sup> glasses,<sup>109</sup> concentrated solution,<sup>110</sup> clusters,<sup>111</sup> and aggregate homo- and heterometallic lanthanide-containing systems.<sup>112</sup> However, to date, examples of this phenomenon have been reported for only five discrete molecular complexes in aqueous medium (**Figure 4.1**). The first example was reported by Faulkner and Pope in 2003 for Tb<sup>3+</sup>/Yb<sup>3+</sup> heterotrimetallic complex **4.1**.<sup>113</sup> The second example was reported in 2006 by Tremblay and Sames for a Tb<sup>3+</sup>/Eu<sup>3+</sup> complex **4.2**.<sup>114</sup> The third and fourth examples were reported in 2011 by Andolina and Morrow for Eu<sup>3+</sup>/Nd<sup>3+</sup> heterodimetallic complexes **4.3** and **4.4**.<sup>83</sup> The fifth example was reported by Nonat and coworkers in 2012 for a homodimetallic Eu<sup>3+</sup> complex **4.5**.<sup>115</sup>



Three requirements must be satisfied for spontaneous energy transfer to occur: (1) a donor ion must absorb excitation energy into an excited state; (2) an acceptor ion must have an excited state slightly lower in energy than the donor excited state; and (3) the donor and acceptor

ions must be physically close enough to facilitate a positive overlap integral between the excited states. Complex **4.1** contains Tb<sup>3+</sup> as the donor and Yb<sup>3+</sup> as the acceptor; **4.2** contains Tb<sup>3+</sup> as the donor and Eu<sup>3+</sup> as the acceptor; and **4.3** and **4.4** contain Eu<sup>3+</sup> as the donor and Nd<sup>3+</sup> as the acceptor. Unlike complexes **4.1–4.4**, complex **4.5** contains two Eu<sup>3+</sup> ions, one serving as the donor and the other as the acceptor. **Table 4.1** outlines the energy levels of the donor and acceptor ions in complexes **4.1–4.4** and the absorption and emission wavelengths expected during energy transfer. Based on the values in **Table 4.1**, the energy state requirements (1) and (2) are satisfied with the metal pairs in **Figure 4.1**. Further, the distance requirement is likely satisfied in these complexes. Without crystallographic evidence for the donor–acceptor distance, we can only assume that the metal ions are close enough to provide a pathway for energy transfer; however, data consistent with energy transfer could be considered evidence of a metal–metal distance ( $d$ ) of less than 10 Å.<sup>116</sup> Such data is has been used to make molecular measurements in proteins and other complex molecules.<sup>117</sup> These studies assume that energy transfer occurs via the dipole–dipole Förster mechanism, in which the efficiency of energy transfer is proportional to  $d^{-6}$  and can be effective up to 10 Å.<sup>116</sup>

**Table 4.1.** Summary of energy states involved in energy transfer for lanthanides used in **4.1–4.4**.

Ln <sup>3+</sup>	Donor State	Donor State Energy (cm <sup>-1</sup> )	$\lambda_{\text{ex}}^*$ (nm)	Acceptor State	Acceptor State Energy (cm <sup>-1</sup> )	$\lambda_{\text{em}}^*$ (nm)
Tb <sup>3+</sup>	<sup>5</sup> D <sub>4</sub>	20,408	490	—	—	—
Eu <sup>3+</sup>	<sup>5</sup> D <sub>0</sub>	17,241	580	<sup>5</sup> D <sub>0</sub>	17,241	580, 595, 615, 650, 720
Nd <sup>3+</sup>	—	—	—	<sup>4</sup> F <sub>3/2</sub>	11,111	900, 1060, 1350
Yb <sup>3+</sup>	—	—	—	<sup>2</sup> F <sub>3/2</sub>	10,204	980

\*wavelength values can vary  $\pm 5$  nm

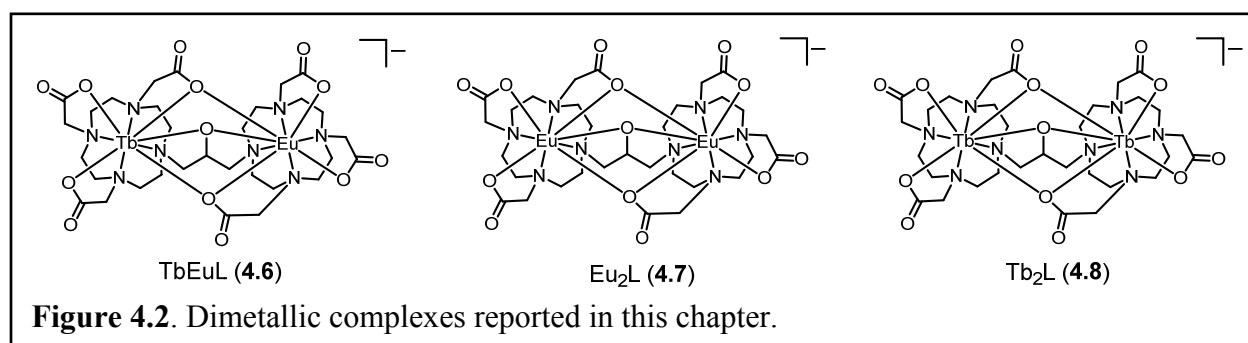
The method used to demonstrate energy transfer in the studies of **4.1** and **4.3–4.5** was a comparison of the luminescence-decay rate of the donor ion in the absence and presence of the acceptor.<sup>83, 113, 115</sup> In this approach, the donor is treated as being quenched by the acceptor. A faster decay rate in the presence of the acceptor suggests Ln–Ln energy transfer. However, Eu<sup>3+</sup>

and  $\text{Tb}^{3+}$  are also quenched by CH, NH, and OH oscillators. This fact limits the interpretation of luminescence-decay rate differences, particularly when the molecular structure is changed by removing the acceptor ion. An orthogonal technique to observe energy transfer is to acquire steady state excitation and emission spectra of the complex. While the decay data presented in studies of **4.1** and **4.3–4.5** indicate that energy transfer occurs in these systems, the authors do not report excitation and emission spectra associated with such a process. Emission spectra for **4.2** were reported and show simultaneous emission from  $\text{Tb}^{3+}$  and  $\text{Eu}^{3+}$ ; however, the spectra were acquired with ligand-sensitized excitation. No evidence of  $\text{Eu}^{3+}$  emission with direct  $\text{Tb}^{3+}$  excitation or  $\text{Tb}^{3+}$  luminescence-decay data was presented.<sup>114</sup> Ultimately, for Ln–Ln energy transfer to prove practically useful, the energy transfer process needs to be efficient enough to produce acceptor-based emission spectra from donor-based excitation. To satisfactorily characterize the presence of Ln–Ln energy transfer, I propose that both steady state spectra and luminescence-decay data must be reported to completely identify the energy transfer process.

To this end, I synthesized  $\text{Tb}^{3+}$ - and  $\text{Eu}^{3+}$ -containing heterodimetallic complex **4.6** (**Figure 4.2**). My previous work, described in Chapter 3, indicated that the structure of the homodimetallic  $\text{Eu}^{3+}$  analog was bridged by three oxygen atoms (**Figures 3.4** and **3.6**). Due to the similar ionic radii of  $\text{Tb}^{3+}$  and  $\text{Eu}^{3+}$ , I expected the structure of **4.6** to be similarly bridged. Using  $\text{Tb}^{3+}$  and  $\text{Eu}^{3+}$ , I hypothesized that energy transfer from  $\text{Tb}^{3+}$  to  $\text{Eu}^{3+}$  would empirically confirm the optimized structure and provide a platform for tuning the excitation, emission, and lifetime properties of lanthanide-based probes.

A discrete molecule exhibiting efficient Ln–Ln energy transfer could be useful for fundamental studies of energy transfer mechanisms as well as for fluorescence imaging. Many lanthanide-based luminescent probes have been developed because of the narrow absorption and

emission bands of these ions.<sup>116</sup> Additionally, lanthanide ions exhibit microsecond to millisecond luminescence lifetimes, allowing typically weak lanthanide-based emission bands to be observed after background organic-based fluorescence decays.<sup>116</sup> Further,  $\text{Nd}^{3+}$ ,  $\text{Sm}^{3+}$ ,  $\text{Ho}^{3+}$ ,  $\text{Er}^{3+}$ , and  $\text{Yb}^{3+}$  emit in the near-IR region, which may allow background fluorescence to be avoided completely and may also provide probes that can be observed through opaque tissue. Introducing a system wherein the excitation, emission, and lifetime properties can be selected simply by choosing the metal ions to chelate in a ligand may offer new capabilities to biological and medical imaging, providing a boon to research and diagnostic medicine.



## Experimental Procedures

### General Procedures

Commercially available chemicals were of reagent-grade purity or better and were used without further purification unless otherwise noted. Water was purified using a PURELAB Ultra Mk2 water purification system (ELGA). Preparation of 1,3-di[1,4,7,10-tetraazacyclododecanyl-(1,4,7-triacetate)]propan-2-ol, **3.4**, was carried out according to my published procedure.<sup>Moore, JACS 2012</sup> Purification of metal complexes was carried out using reverse-phase high-performance liquid chromatography (HPLC) with a binary gradient ( $\text{H}_2\text{O}/\text{CH}_3\text{CN}$ ) using two Shimadzu Prominence LC20AT HPLC pumps, SIL-20AHT autosampler, RF10AXL fluorescence detector ( $\lambda_{\text{ex}} = 394 \text{ nm}$ ,  $\lambda_{\text{em}} = 616 \text{ nm}$  for **4.7** and  $\lambda_{\text{ex}} = 228 \text{ nm}$ ,  $\lambda_{\text{em}} = 545 \text{ nm}$  for **4.8**) fitted with a

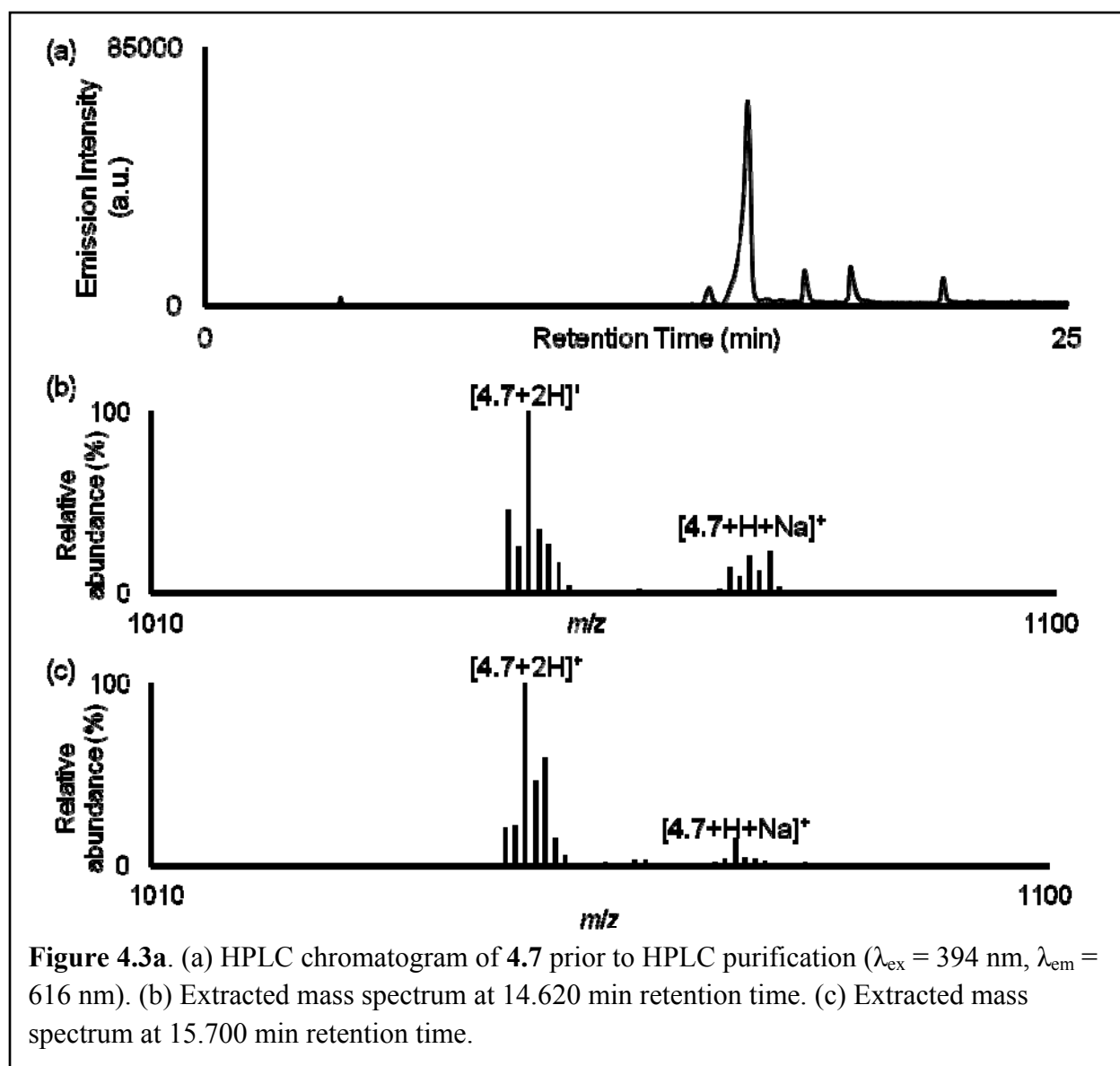
Pinnacle PFP column (10 mm × 250 mm, Restek). Centrifugation was carried out using a Fisher Scientific Centric centrifuge (Model 255) operated at speed setting 8 for 5 minutes. All samples were filtered through Millex-LG hydrophilic PTFE syringe filters (4 mm or 25 mm).

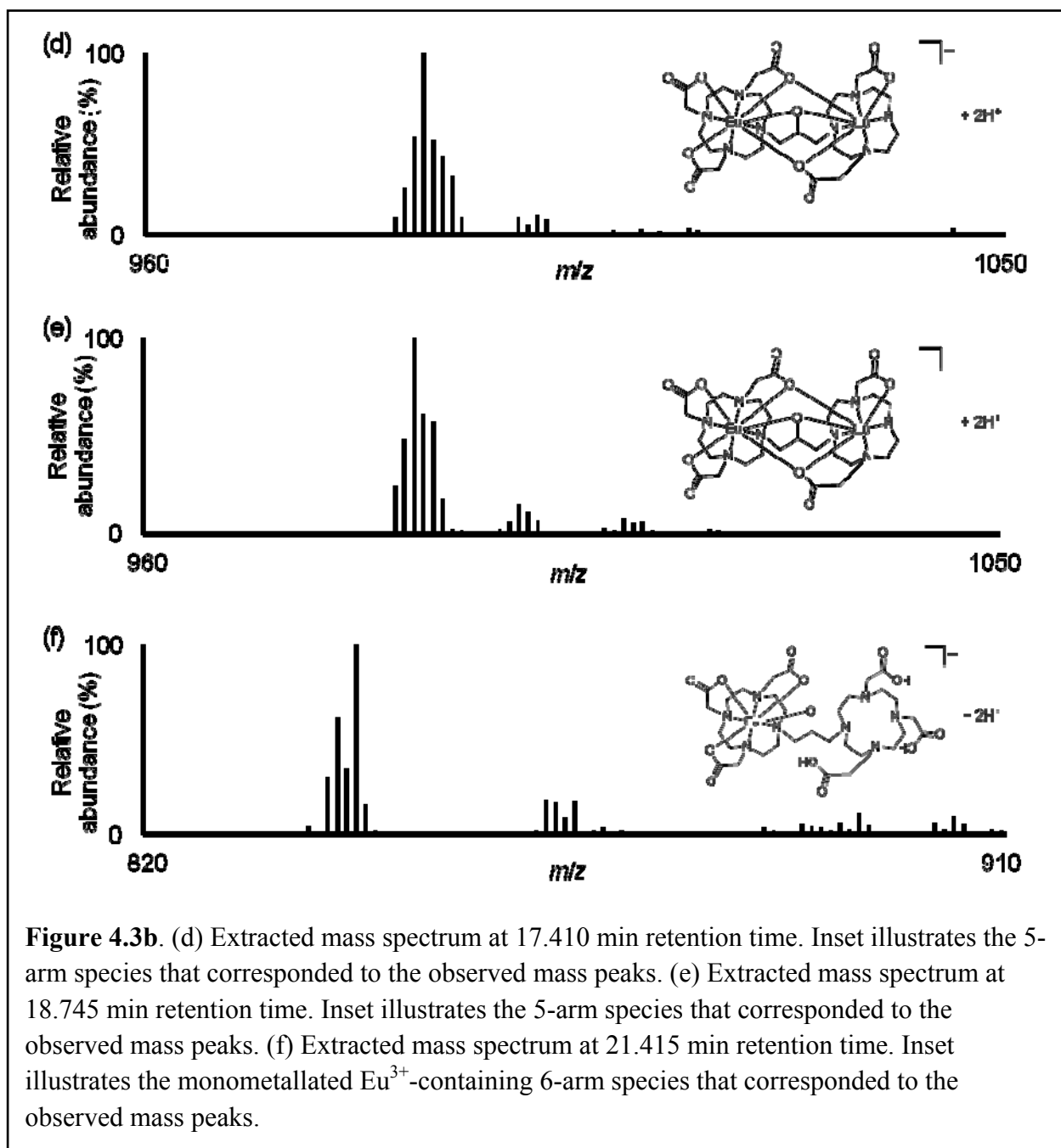
Purity and identification of HPLC-purified compounds was determined by HPLC-coupled electrospray ionization mass spectrometry (ESIMS) using a Pinnacle PFP column (4 mm × 250 mm, Restek) and an electrospray Shimadzu LCMS2010EV spectrometer. High-resolution electrospray ionization mass spectra (HRESIMS) were obtained using an electrospray time-of-flight high-resolution Waters Micromass LCT Premier XE mass spectrometer and were acquired without use of a column.

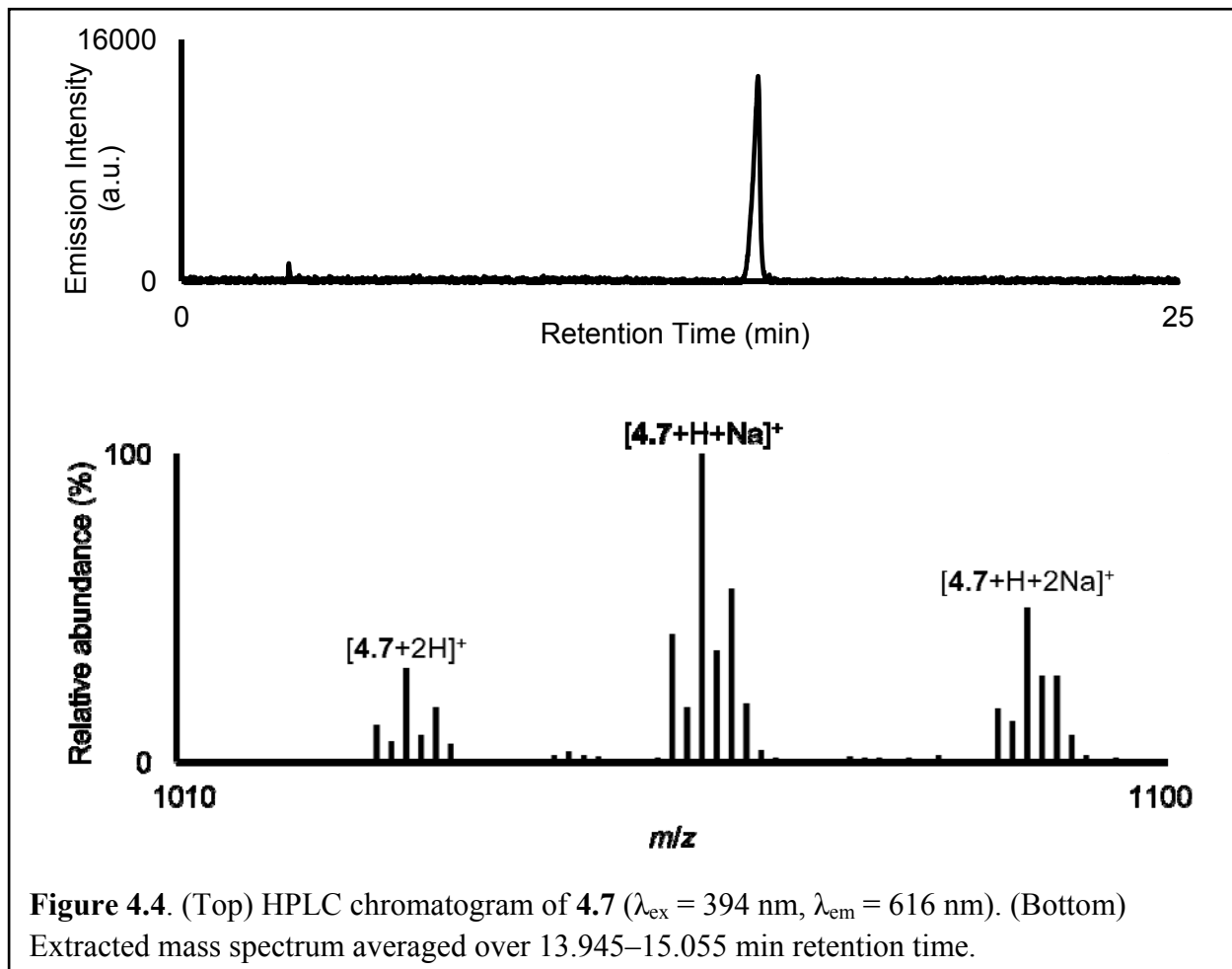
### *Syntheses of Metal Complexes*

Ammonium{1,3-bis[europium-(1,4,7,10-tetraazacyclododecanyl-(1,4,7-triacetate))]propan-2-oxide} (NH<sub>4</sub>**4.7**): A solution of 1,3-di[1,4,7,10-tetraazacyclododecanyl-(1,4,7-triacetate)]propan-2-ol (**4.9**) (1.17 mL, 57.07 mM, 0.0668 mmol, 1 equiv) was added to a flask, and the pH of the solution was adjusted to 6.5 with NH<sub>4</sub>OH (5% aqueous solution). To the resulting solution of **4.9** was added an aqueous solution of europium triflate (49.58 mM, 4.00 mL, 0.200 mmol, 3 equiv). The resulting solution was stirred at ambient temperature for 12 h while the pH was maintained at 6.5 with NH<sub>4</sub>OH (5% aqueous solution). After 12 h, the pH was raised to 10 with NH<sub>4</sub>OH (1 mL, 30% aqueous solution) to precipitate excess europium as insoluble hydroxide. After stirring for 12 h, the resulting mixture was centrifuged and the supernatant was separated. The solid was washed with NH<sub>4</sub>OH (5 mL, 5% aqueous solution); the mixture was centrifuged; and the supernatant was removed. This washing procedure was repeated three times. The combined supernatants were filtered through a 0.2 μm syringe filter to remove any remaining Eu(OH)<sub>3</sub>. The solution was concentrated under reduced pressure. HPLC-

MS analysis indicated that the solution contained both 5- and 6-arm metal complexes (**Figures 4.3a** and **4.3b**). Therefore, the desired 6-arm product was purified by collecting the HPLC eluent at 14.5 minutes (4 mL/min, 5 to 15% CH<sub>3</sub>CN/H<sub>2</sub>O over 4 min). The combined fractions were concentrated, and the solvent was removed under reduced pressure to yield 47.6 mg (64%) of NH<sub>4</sub>4.7. Purity was confirmed by HPLC-MS analysis (4 mL/min, 5 to 15% CH<sub>3</sub>CN/H<sub>2</sub>O over 4 min) (**Figure 4.4**). HRESIMS ( $m/z$ ): [M]<sup>-</sup> calcd for Eu<sub>2</sub>C<sub>31</sub>H<sub>49</sub>N<sub>8</sub>O<sub>13</sub>, 1043.1816; found, 1043.1830.







Ammonium{1,3-bis[terbium-(1,4,7,10-tetraazacyclododecanyl-(1,4,7-triacetate))]propan-2-oxide} ( $\text{NH}_4$ **4.8**): An aliquot of **4.9** (57.07 mM, 2.30 mL, 0.131 mmol, 1 equiv) was added to a flask, and the pH of the solution was adjusted to 6.5 with  $\text{NH}_4\text{OH}$  (5% aqueous solution). To the solution of **4.9** was added a solution of terbium triflate (183.9 mg, 0.3083 mmol, 2.3 equiv) in water (1 mL). The resulting solution was stirred at ambient temperature for 12 h while the pH was maintained at 6.5 with  $\text{NH}_4\text{OH}$  (5% aqueous solution). After 12 h, the pH was raised to 10 with  $\text{NH}_4\text{OH}$  (1 mL, 30% aqueous solution) to precipitate excess terbium as insoluble hydroxides. After stirring for 12 h, the resulting mixture was centrifuged, and the supernatant was separated. The solid was washed with  $\text{NH}_4\text{OH}$  (5 mL, 5% aqueous solution); the mixture was centrifuged; and the supernatant was removed. This washing procedure was repeated three

times. The combined supernatants were filtered through a 0.2  $\mu\text{m}$  syringe filter to remove any remaining  $\text{Tb}(\text{OH})_3$ . The solution was concentrated under reduced pressure. HPLC-MS analysis indicated that the solution contained both 5- and 6-arm metal complexes. Therefore, the desired 6-arm product was purified by collecting the HPLC eluent at 4.3 minutes (4 mL/min, 10%  $\text{CH}_3\text{CN}/\text{H}_2\text{O}$ ). The combined fractions were concentrated, and the solvent was removed under reduced pressure to yield 27.2 mg (18%) of  $\text{NH}_4\mathbf{4.7}$ . Purity was confirmed by HPLC-MS analysis (1 mL/min, 10%  $\text{CH}_3\text{CN}/\text{H}_2\text{O}$ ) (**Figure 4.5**). HRESIMS ( $m/z$ ):  $[\text{M}+\text{H}]^+$  calcd for  $\text{Tb}_2\text{C}_{31}\text{H}_{49}\text{N}_8\text{O}_{13}$ , 1061.2083; found, 1061.2072.

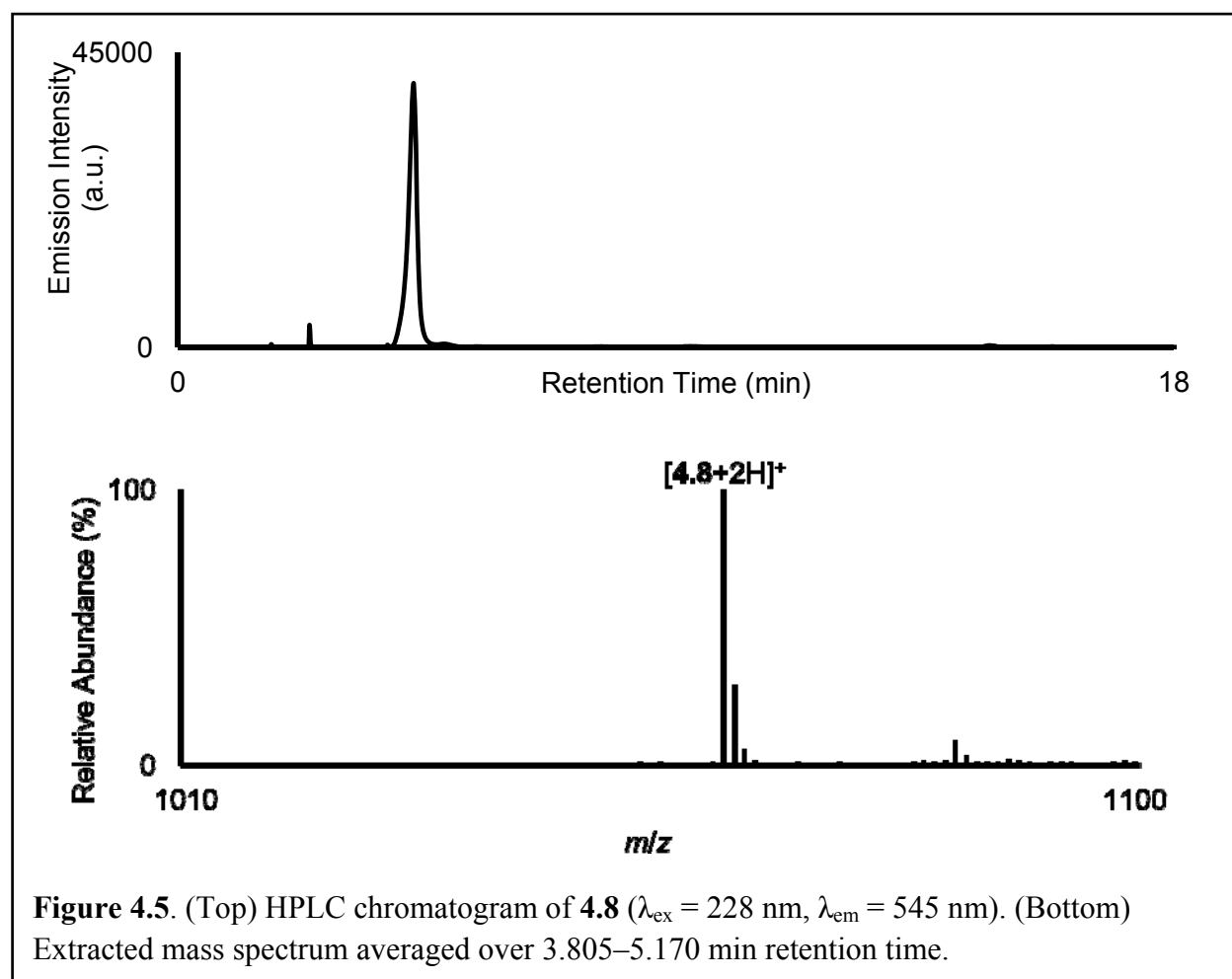


**Figure 4.5.** (Top) HPLC chromatogram of **4.8** ( $\lambda_{\text{ex}} = 228 \text{ nm}$ ,  $\lambda_{\text{em}} = 545 \text{ nm}$ ). (Bottom) Extracted mass spectrum averaged over 3.805–5.170 min retention time.

Ammonium{1-[europium-(1,4,7,10-tetraazacyclododecanyl-(1,4,7-triacetate)), 3-[terbium-(1,4,7,10-tetraazacyclododecanyl-(1,4,7-triacetate))]propan-2-oxide} (**4.6**): A solution of **4.9** in water (1.00 mL, 57.07 mM, 0.057 mmol, 1 equiv) was added to a flask, and the pH of the solution was adjusted to 6.5 with NH<sub>4</sub>OH (5% aqueous solution). To the solution of **4.9** was added a solution of europium triflate (1.15 mL, 49.58 mM, 0.057 mmol, 1 equiv). The resulting solution was stirred at ambient temperature for 10 min while the pH was maintained at 6.5 with NH<sub>4</sub>OH (5% aqueous solution). To the resulting solution was added a solution of terbium triflate (1.58 mL, 36.04 mM, 0.057 mmol, 1 equiv). The resulting solution was stirred at ambient temperature for 12 h while the pH was maintained at 6.5 with NH<sub>4</sub>OH (5% aqueous solution). After 12 h, the pH was raised to 10 with NH<sub>4</sub>OH (1 mL, 30% aqueous solution) to precipitate excess europium and terbium as insoluble hydroxides. After stirring for 12 h, the resulting mixture was centrifuged and the supernatant was separated. The solid was washed with NH<sub>4</sub>OH (5 mL, 5% aqueous solution); the mixture was centrifuged; and the supernatant was removed. This washing procedure was repeated three times. The combined supernatants were filtered through a 0.2 μm syringe filter to remove any remaining Eu(OH)<sub>3</sub> and Tb(OH)<sub>3</sub>. The solution was concentrated under reduced pressure. HPLC-MS analysis indicated that the solution contained both 5- and 6-arm metal complexes including complexes **4.6** and **4.7**. Complexes **4.6** and **4.7** could not be separated, likely due to structural similarities. Therefore, the 6-arm products, **4.6** and **4.7**, were isolated as an inseparable mixture by collecting the HPLC eluent at 13.9 minutes (4 mL/min, 5 to 15% CH<sub>3</sub>CN/H<sub>2</sub>O over 4 min). The combined fractions were concentrated and the solvent was removed under reduced pressure to yield 28.34 mg of a mixture of NH<sub>4</sub>**4.6** and NH<sub>4</sub>**4.7** (**Figure 4.6**). No evidence of **4.8** was observed, likely due to the order of addition of the metals.

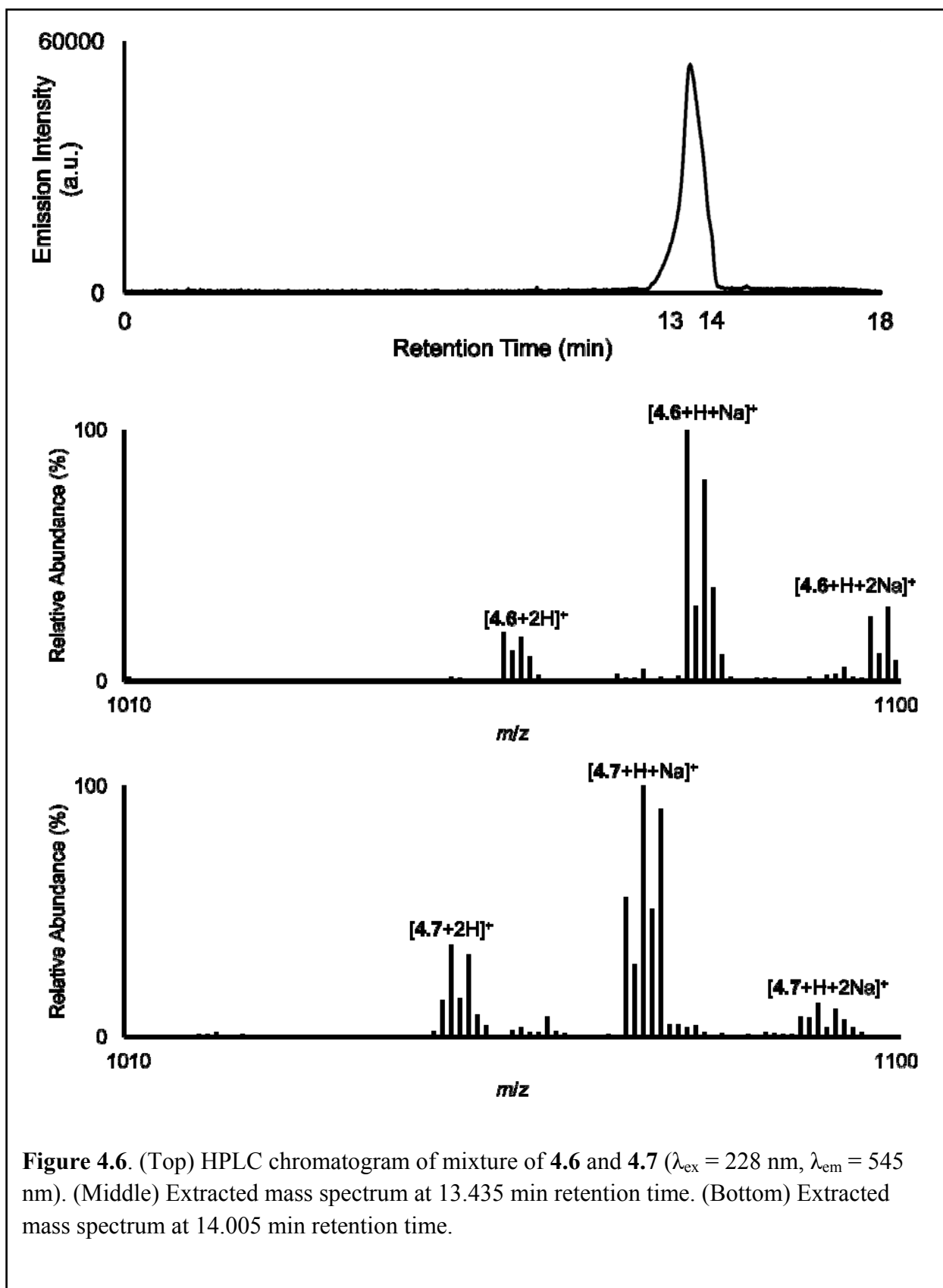


**Figure 4.6.** (Top) HPLC chromatogram of mixture of 4.6 and 4.7 ( $\lambda_{\text{ex}} = 228$  nm,  $\lambda_{\text{em}} = 545$  nm). (Middle) Extracted mass spectrum at 13.435 min retention time. (Bottom) Extracted mass spectrum at 14.005 min retention time.

### *Steady State Luminescence Spectra and Luminescence-Decay Rate Measurements*

Luminescence excitation and emission spectra were acquired using a HORIBA Jobin Yvon Fluoromax-4 spectrofluorometer equipped with a 400 W xenon lamp in fluorescence mode. Excitation spectra were acquired by scanning from 200 to 540 nm excitation wavelength (increment = 1 nm, excitation slit width = 1 nm, emission slit width = 5 nm). Excitation spectra for all complexes were acquired at 545 and 612 nm emission wavelengths, corresponding to the emission maxima of  $\text{Tb}^{3+}$  and  $\text{Eu}^{3+}$ , respectively. Emission spectra were acquired with 394 and 487 nm excitation wavelengths, corresponding to the excitation maxima specific to  $\text{Eu}^{3+}$  and  $\text{Tb}^{3+}$ , respectively. Emission spectra were acquired by scanning from 430 to 725 nm excitation wavelength (increment = 1 nm, excitation slit width = 5 nm, emission slit width = 1 nm).

Samples of **4.6**, **4.7**, and **4.8** were prepared by dissolving the solids in water (1 mL) and transferring a 250  $\mu\text{L}$  aliquot of the resulting solutions to a 2 mm  $\times$  2 mm  $\times$  32 mm quartz cuvette. A mixture of homodimetallic complexes **4.7** and **4.8** was prepared by mixing 125  $\mu\text{L}$  aliquots of the individual mixtures prepared above. The pH of all samples was approximately 7.5 as measured with pH paper.

## **Results and Discussion**

### *Spectral Assignment of $\text{Tb}^{3+}$ and $\text{Eu}^{3+}$ Complexes*

Luminescence emissions from  $\text{Tb}^{3+}$  originate from depopulation of the  $^5\text{D}_4$  energy level to the  $^7\text{F}$  manifold (**Figure 4.7**). The  $^5\text{D}_j$  and  $^7\text{F}_j$  levels of  $\text{Tb}^{3+}$  are almost exclusively composed of  $4f^8$  orbitals that are shielded from bonding and crystal field perturbations and require minimal nuclear reorganization energy upon excitation, resulting in minimal variation in emission wavelengths (<10 nm) and relative intensities of each transition, regardless of coordination environment. Therefore,  $\text{Tb}^{3+}$  emission spectra are predictable, and commonly observed

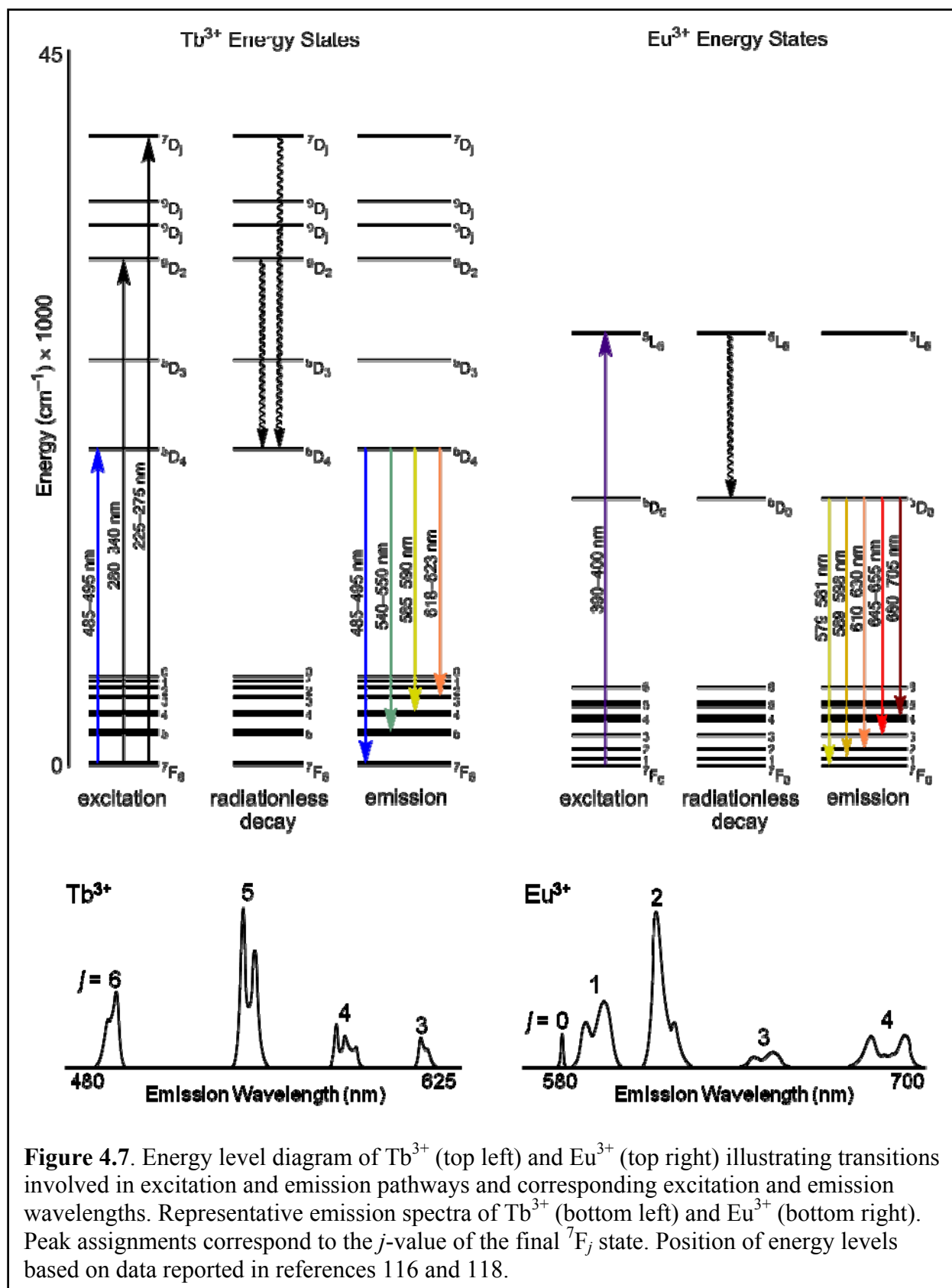


**Figure 4.7.** Energy level diagram of  $Tb^{3+}$  (top left) and  $Eu^{3+}$  (top right) illustrating transitions involved in excitation and emission pathways and corresponding excitation and emission wavelengths. Representative emission spectra of  $Tb^{3+}$  (bottom left) and  $Eu^{3+}$  (bottom right). Peak assignments correspond to the  $j$ -value of the final  $7F_j$  state. Position of energy levels based on data reported in references 116 and 118.

transitions at 490, 545, 590, and 620 nm are reliably assigned to depopulation of the  $^5D_4$  state to the  $^7F_j$  manifold, where  $j = 6, 5, 4,$  and  $3,$  respectively (**Figure 4.7**).<sup>116, 118</sup> The  $^5D_4 \rightarrow ^7F_j$  transitions almost always appear with intensity decreasing in order of  $j = 5 > 6 > 4 > 3$  (**Figure 4.7**).

All modes of  $Tb^{3+}$  excitation ultimately result in population of and emission from the  $^5D_4$  level. Therefore, excitation spectra are typically acquired by scanning excitation wavelength and monitoring the emission intensity of the  $^5D_4$  to  $^7F_5$  transition at 545 nm because it provides the highest sensitivity. The  $^5D_4$  level of  $Tb^{3+}$  can be populated through multiple pathways including indirect and direct excitation of  $Tb^{3+}$ . Indirect excitation will not be discussed here because it does not occur in molecules such as  $Tb_2L$ , **4.6**, which lack donor fluorophores. Direct excitation of  $Tb^{3+}$  can be achieved by stimulation of transitions from  $^7F_6$  to  $^7D_j$ ,  $^9D_2$ , and  $^5D_4$  levels using 225–275, 280–340, or 490 nm radiation, respectively (**Figure 4.7**). The  $^7D$  and  $^9D$  are composed of the  $4f^7 5d^1$  orbitals that are more strongly affected by bonding interactions than the  $4f^8$  orbitals. As a result, the nuclear reorganization energy is greater for transitions to the  $^7D$  and  $^9D$  levels than the  $^5D_4$  level, resulting in broad transitions in the UV range of the excitation spectra, denoted by the wide range of wavelengths for these transitions (**Figure 4.7**). Non-radiative decay from the  $^7D$  and  $^9D$  states results in population of the  $^5D_4$  level. The excitation of the  $^7F_6 \rightarrow ^5D_4$  transition is inefficient, resulting in weak emission, but appears consistently between 485 and 495 nm, making it a useful signature for  $Tb^{3+}$  excitation.

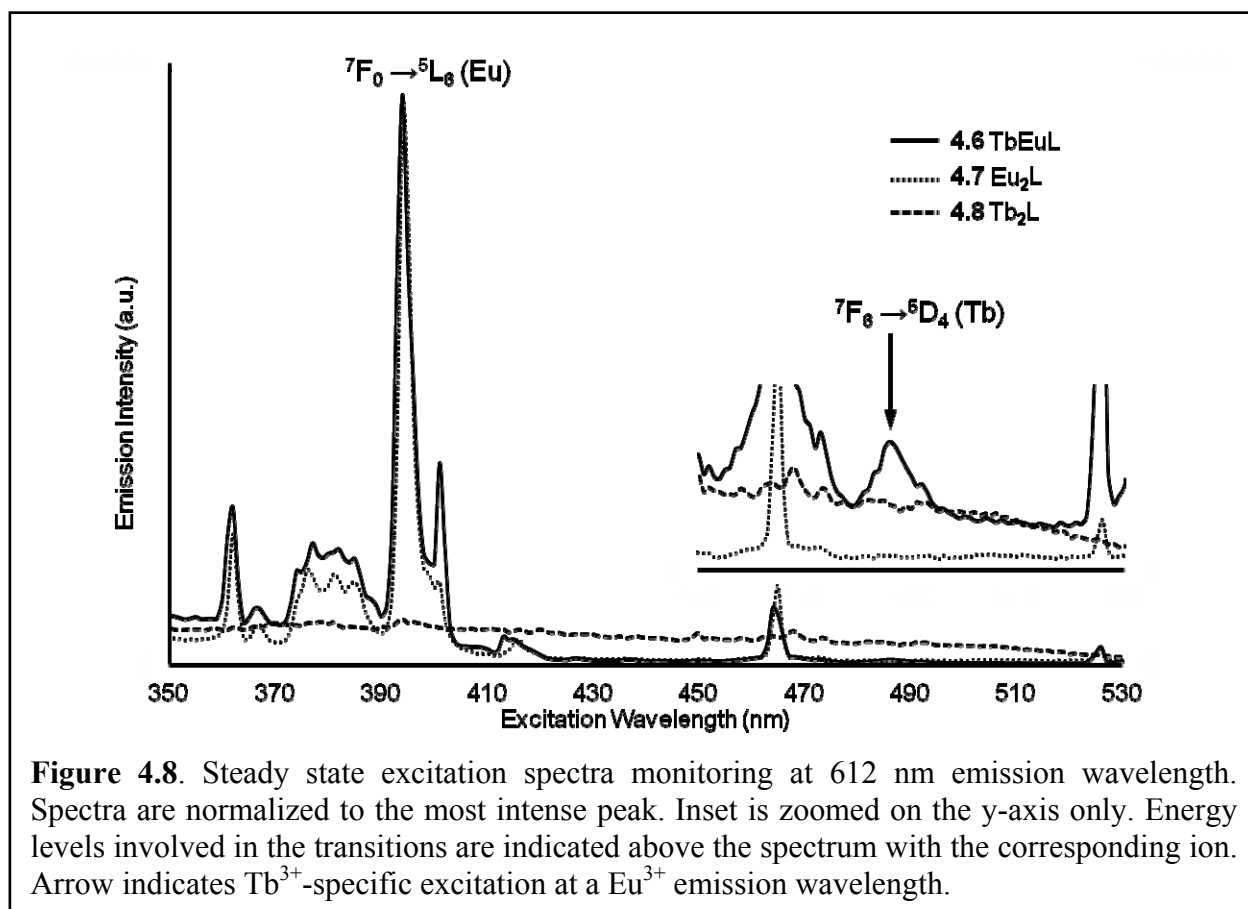
Luminescence emissions from  $Eu^{3+}$  originate from depopulation of the  $^5D_0$  energy level to the  $^7F$  manifold. Similarly to  $Tb^{3+}$ , the  $^5D_j$  and  $^7F_j$  levels of  $Eu^{3+}$  are almost exclusively composed of  $4f^8$  orbitals that are shielded from bonding and crystal field perturbations and require minimal nuclear reorganization energy upon excitation, resulting in minimal variation in

emission wavelengths (<20 nm) and relative intensities of each transition, regardless of coordination environment. Therefore,  $\text{Eu}^{3+}$  emission spectra are predictable, and commonly observed transitions at 580, 594, 615, 650, and 700 nm are reliably assigned to depopulation of the  $^5\text{D}_0$  state to the  $^7\text{F}_j$  manifold, where  $j = 0, 1, 2, 3,$  and  $4$ , respectively (**Figure 4.7**).<sup>116, 118</sup> For complexed  $\text{Eu}^{3+}$ , the  $^5\text{D}_4 \rightarrow ^7\text{F}_j$  transitions almost always appear with intensity decreasing in order of  $j = 2 > 1 > 4 > 3 \approx 0$  (**Figure 4.7**).

Excitation spectra of  $\text{Eu}^{3+}$  are acquired by scanning excitation wavelength and monitoring the emission intensity of the  $^5\text{D}_0 \rightarrow ^7\text{F}_2$  transition at 615 nm because it provides the highest sensitivity. The  $^5\text{D}_0$  level of  $\text{Eu}^{3+}$  can be populated through multiple pathways including direct and indirect excitation of  $\text{Eu}^{3+}$ . Unlike  $\text{Tb}^{3+}$  excitation, direct excitation of  $\text{Eu}^{3+}$  through  $^7\text{F}_j \rightarrow ^5\text{D}_0$  transitions is inefficient and is not practically useful without a laser excitation source. Direct excitation of  $\text{Eu}^{3+}$  is achieved most efficiently by stimulation of the transition from  $^7\text{F}_0$  to  $^5\text{L}_6$  (**Figure 4.7**). Due to the minimal impact of nuclear reorganization on the  $^7\text{F}_0 \rightarrow ^5\text{L}_6$  transition, the excitation wavelength appears consistently at  $395 \pm 5$  nm, making it a useful signature for  $\text{Eu}^{3+}$  excitation. Indirect excitation of  $\text{Eu}^{3+}$  can be achieved via non-radiative energy transfer from a higher-energy, donor-localized excited state to the  $^5\text{D}_0$  level. Therefore, energy transfer is indicated if the  $\text{Eu}^{3+}$  emission fingerprint results from excitation of transitions not associated with  $\text{Eu}^{3+}$ . Importantly, the density of lanthanide energy levels increases dramatically above  $30,000 \text{ cm}^{-1}$  (below 333 nm), and UV irradiation of samples containing  $\text{Tb}^{3+}$  and  $\text{Eu}^{3+}$  may result in simultaneous excitation.<sup>118</sup> Given this ambiguity, energy transfer between these and other lanthanides must be studied using lower energy radiation, where specific excitation of unique  $\text{Tb}^{3+}$  or  $\text{Eu}^{3+}$  transitions is reliable. This strategy was used for the acquisition of excitation and emission spectra of **4.6**, **4.7**, and **4.8**, discussed in the following sections.

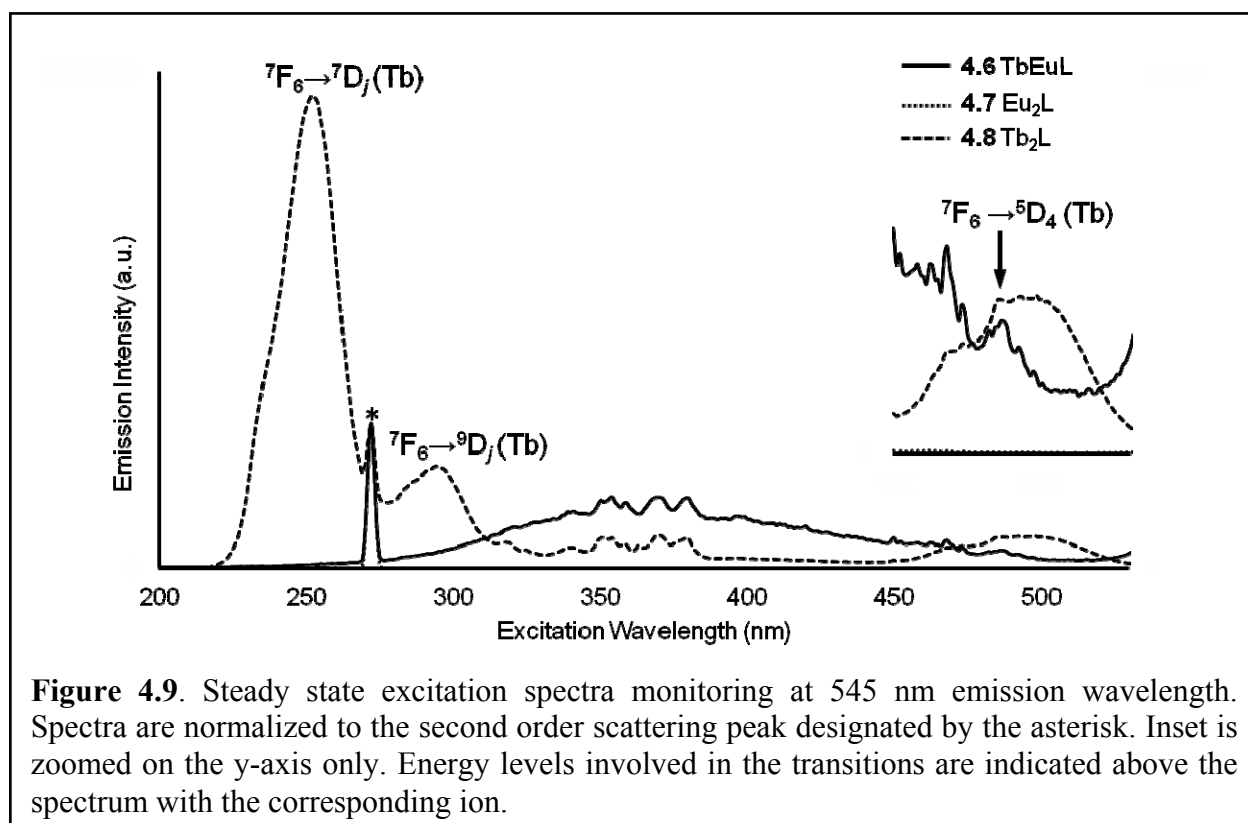
### Analysis of Steady State Excitation Spectra

An excitation spectrum of  $\text{Eu}_2\text{L}$ , **4.7**, was generated by recording the emission intensity of the  ${}^5\text{D}_0 \rightarrow {}^7\text{F}_2$  transition of  $\text{Eu}^{3+}$  at 612 nm and scanning excitation wavelength. The resulting excitation spectrum was typical of  $\text{Eu}^{3+}$ -containing complexes and displayed a 394 nm excitation maximum, corresponding to the  ${}^7\text{F}_0 \rightarrow {}^5\text{L}_6$  transition of  $\text{Eu}^{3+}$  (**Figure 4.8**). Importantly, an excitation peak at 487 nm was not observed, indicating that there were no  $\text{Eu}^{3+}$ -based transitions that overlap the  $\text{Tb}^{3+}$ -based  ${}^5\text{D}_4 \rightarrow {}^7\text{F}_6$  transition at 487 nm. Therefore, any excitation peaks at 487 nm in the  $\text{Tb}_2\text{L}$ - or  $\text{TbEuL}$ -containing systems were likely to originate from  $\text{Tb}^{3+}$  excitation.



A second excitation spectrum of  $\text{Eu}_2\text{L}$ , **4.7**, was acquired by recording the emission intensity of the  ${}^5\text{D}_4 \rightarrow {}^7\text{F}_5$  transition of  $\text{Tb}^{3+}$  at 545 nm (**Figure 4.9**). As expected for **4.7**, which contained no  $\text{Tb}^{3+}$ , no excitation peaks were observed while recording the emission intensity at

545 nm, confirming that  $\text{Eu}^{3+}$ -based emission from **4.7** would not coincide with  $\text{Tb}^{3+}$ -based emission in the 545 nm range with any excitation wavelength (**Figure 4.9**).



An excitation spectrum of  $\text{Tb}_2\text{L}$ , **4.8**, was generated by recording the emission intensity of the  ${}^5\text{D}_4 \rightarrow {}^7\text{F}_5$  transition of  $\text{Tb}^{3+}$  at 545 nm and scanning excitation wavelength. The resulting excitation spectrum displayed broad excitation maxima at 252 and 295 nm, corresponding to  $\text{Tb}^{3+}$  transitions from the  ${}^7\text{F}_0$  to  ${}^7\text{D}$  and  ${}^9\text{D}$  states, respectively (**Figure 4.9**). Importantly, a weak excitation peak at 487 nm was observed, corresponding to the  $\text{Tb}^{3+}$ -based  ${}^5\text{D}_4 \rightarrow {}^7\text{F}_6$  transition at the expected wavelength. The presence of an excitation peak at 487 nm in the spectrum of  $\text{Tb}_2\text{L}$ , **4.8**, combined with the absence of a peak at 487 nm in the excitation spectrum of  $\text{Eu}_2\text{L}$ , **4.7**, confirmed that an excitation peak at 487 nm in the excitation spectrum of  $\text{TbEuL}$ , **4.6**, originated from  $\text{Tb}^{3+}$  excitation.

A second excitation spectrum of Tb<sub>2</sub>L, **4.8**, was acquired by recording the emission intensity of the  $^5D_0 \rightarrow ^7F_2$  transition of Eu<sup>3+</sup> at 612 nm (**Figure 4.8**). As expected for **4.8**, which contained no Eu<sup>3+</sup>, no excitation peaks were observed while recording the emission intensity at 612 nm, confirming that Tb<sup>3+</sup>-based emission from **4.8** would not coincide with Eu<sup>3+</sup>-based emission in the 612 nm range with any excitation wavelength (**Figure 4.8**).

Because TbEuL, **4.6**, could not be isolated from Eu<sub>2</sub>L, **4.7**, excitation spectra were acquired using a sample containing both **4.6** and **4.7**, which I will henceforth refer to as **4.6**. An excitation spectrum of TbEuL, **4.6**, was generated by recording the emission intensity of the  $^5D_0 \rightarrow ^7F_0$  transition of Eu<sup>3+</sup> at 612 nm and scanning excitation wavelength (**Figure 4.8**). The resulting excitation spectrum was similar to that of Eu<sub>2</sub>L, **4.7**, and displayed an excitation maximum at 394 nm, consistent with the Eu<sup>3+</sup> transition from  $^7F_0$  to  $^5L_6$  (**Figure 4.8**). Importantly, a weak excitation peak at 487 nm was also observed. The presence of an excitation peak corresponding to the Tb<sup>3+</sup>-based  $^7F_6 \rightarrow ^5D_4$  transition at 487 nm while monitoring the emission from the Eu<sup>3+</sup>-based the  $^5D_0 \rightarrow ^7F_0$  transition at 612 nm indicated that energy transfer was occurring from the Tb<sup>3+</sup>-based  $^5D_4$  level to the Eu<sup>3+</sup>-based  $^5D_0$  level.

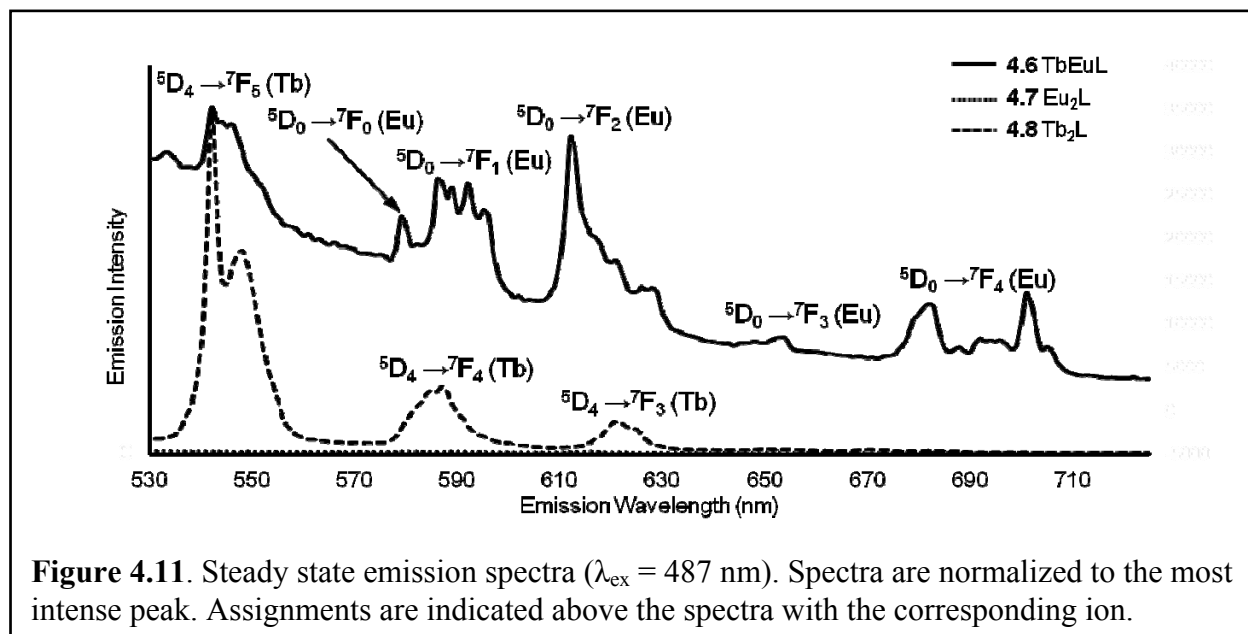
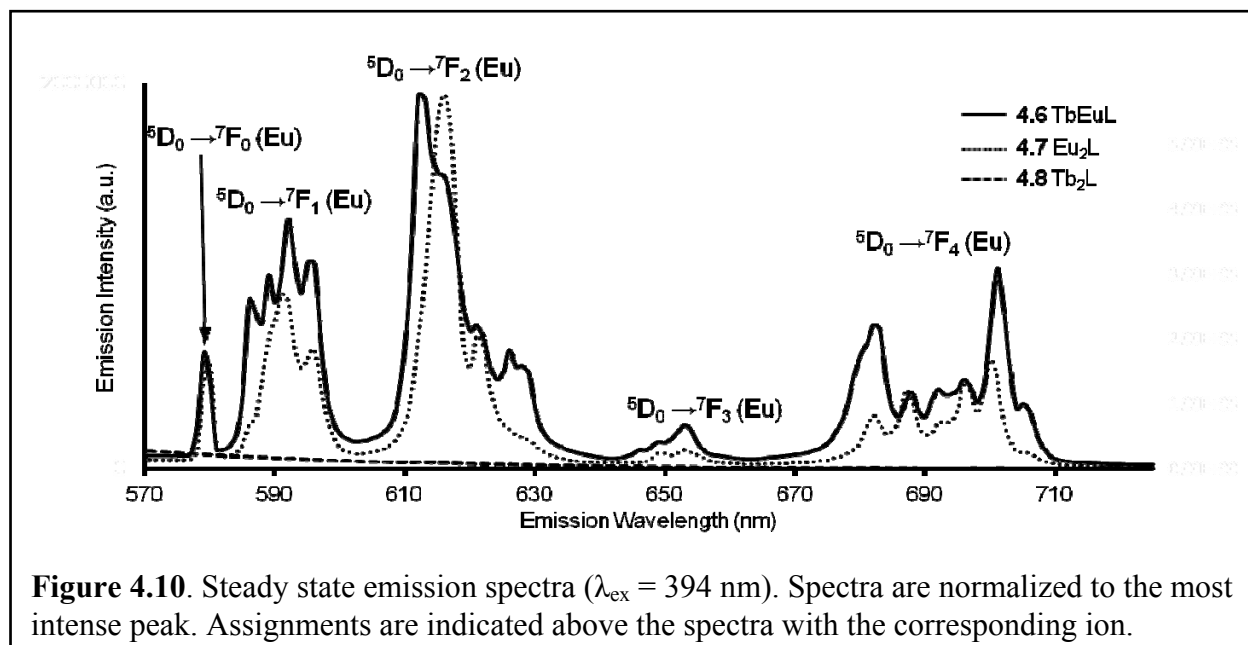
A second excitation spectrum of TbEuL, **4.6**, was acquired by recording the emission intensity of the  $^5D_4 \rightarrow ^7F_5$  transition of Tb<sup>3+</sup> at 545 nm (**Figure 4.9**). Peaks corresponding to the  $^7F_6$  to  $^7D$  and  $^9D$  states at 252 and 295 nm were absent, and the peak corresponding to the  $^7F_6$  to  $^5D_4$  transition at 487 nm was substantially weaker in the spectrum of TbEuL, **4.6**, than in the spectrum of Tb<sub>2</sub>L, **4.8**. The concentration of Tb<sup>3+</sup> in the sample of **4.6** was lower than in **4.8** and the absence of peaks at 252 and 295 nm might be the result of low concentration. However, the ratio between the peaks at 252, 295, and 487 nm is not expected to differ dramatically between **4.6** and **4.8**; and, peak at 487 nm was observed in the spectrum of **4.6**, suggesting that the peaks

at 252 and 295 nm are absent due to a quenching pathway only present in TbEuL, **4.6**. Given the increased density of energy levels at energies above  $30,000\text{ cm}^{-1}$  (wavelengths below 333 nm) for both  $\text{Tb}^{3+}$  and  $\text{Eu}^{3+}$ , energy transfer between  $\text{Tb}^{3+}$ -based  ${}^7\text{D}$  and  ${}^9\text{D}$  states and  $\text{Eu}^{3+}$ -based high energy excited states might be possible. However, the density of states at high energy prevents the study of energy transfer at high energy due to ambiguous excitation. Therefore, emission spectra were only recorded using excitation wavelengths unique to  $\text{Eu}^{3+}$  or  $\text{Tb}^{3+}$ , at 394 nm or 487 nm, respectively. Based on the excitation spectra of **4.6**, **4.7**, and **4.8**, I hypothesized that  $\text{Tb}^{3+}$ -centered excitation would result in  $\text{Eu}^{3+}$ -based emission, which would confirm the occurrence of energy transfer from  $\text{Tb}^{3+}$  to  $\text{Eu}^{3+}$ . The emission spectra discussed in the following section were used to test this hypothesis.

#### *Analysis of Steady State Emission Spectra*

The emission spectrum of  $\text{Eu}_2\text{L}$ , **4.7**, was similar to those previously reported with 394 nm excitation radiation and displayed the expected  $\text{Eu}^{3+}$ -based transitions at 580, 592, 616, 653, 682, and 700 nm (**Figure 4.10**).<sup>93</sup> The presence of four transitions in the  ${}^5\text{D}_0 \rightarrow {}^7\text{F}_1$  manifold centered at 592 nm (**Figure 4.10**) suggested that there was more than one  $\text{Eu}^{3+}$  environment present in **4.7** because a maximum of three transitions can occur from a single  $\text{Eu}^{3+}$  environment. However, the presence of only one principle transition at 616 nm (**Figure 4.10**) in the  ${}^5\text{D}_0 \rightarrow {}^7\text{F}_2$  manifold indicated that the symmetry of the two  $\text{Eu}^{3+}$  ions was similar. When **4.7** was irradiated with 487 nm radiation, specific to excitation of  $\text{Tb}^{3+}$ , no emission was observed, as was expected for a complex containing only  $\text{Eu}^{3+}$  (**Figure 4.11**).

The emission spectrum of  $\text{Tb}_2\text{L}$ , **4.8**, with 394 nm excitation radiation displayed no emission peaks, consistent with the expected inability of  $\text{Tb}^{3+}$  to absorb 394 nm radiation (**Figure 4.10**). The emission spectrum of  $\text{Tb}_2\text{L}$  with 487 nm excitation radiation was typical of



$\text{Tb}^{3+}$ -containing complexes, with transitions at 545, 586, and 621 nm, corresponding to transitions from the  $^5\text{D}_4$  state to the  $^7\text{F}_5$ ,  $^7\text{F}_4$ , and  $^7\text{F}_3$  states, respectively (**Figure 4.11**). Structural information cannot be derived from the  $\text{Tb}^{3+}$  emission spectrum because the observed transitions

are not sensitive to  $\text{Tb}^{3+}$  symmetry.<sup>116</sup> However, the emission pattern indicated that the emission of  $\text{Tb}^{3+}$  can be stimulated by direct excitation of the  ${}^7\text{F}_6 \rightarrow {}^5\text{D}_4$  transition at 487 nm.

Because  $\text{TbEuL}$ , **4.6**, could not be isolated from  $\text{Eu}_2\text{L}$ , **4.7**, emission spectra were acquired using a sample containing both **4.6** and **4.7**. I assigned any transitions that did not appear in the spectra of pure **4.7** to emission from **4.6**. Irradiation of the sample containing **4.6** and **4.7** with 394 nm radiation resulted in an emission spectrum with three notable differences from the sample of pure **4.7**: (1) the  ${}^5\text{D}_0 \rightarrow {}^7\text{F}_0$  transition at 579 nm is slightly red-shifted from the **4.7** spectrum; (2) the ratio between the hyperfine transitions at 586 and 592 nm in the  ${}^5\text{D}_0 \rightarrow {}^7\text{F}_1$  manifold increased compared to the spectrum of **4.7**; and (3) an intense transition in the  ${}^5\text{D}_0 \rightarrow {}^7\text{F}_2$  manifold appeared at 612 nm in addition to the 616 nm transition observed in the spectrum of **4.7**. All three of these observations imply the presence a  $\text{Eu}^{3+}$ -containing species with different symmetry than the  $\text{Eu}^{3+}$  ions in **4.7**. Based on HPLC-MS data, I expected that both **4.6** and **4.7** would be present in the sample. I assigned the peaks that appeared in the spectrum of both **4.7** and the mixture of **4.6** and **4.7** to  $\text{Eu}_2\text{L}$ , **4.7**. I assigned the remaining transitions at 586 and 612 nm to **4.6** and assumed that **4.6** also contributed transitions to all other  $\text{Eu}^{3+}$  manifolds.

The emission spectrum of  $\text{TbEuL}$ , **4.6**, with 487 nm excitation wavelength displayed the expected  $\text{Tb}^{3+}$  transition at 545 nm and a set of peaks at 579, 592, 612, 653, 682, and 701 nm that indicated the presence of  $\text{Eu}^{3+}$  emission (**Figure 4.11**). The latter peaks were not observed for  $\text{Tb}_2\text{L}$ , **4.8**, which contained only  $\text{Tb}^{3+}$ , and are known to originate from the  ${}^5\text{D}_0 \rightarrow {}^7\text{F}_0$ ,  ${}^5\text{D}_0 \rightarrow {}^7\text{F}_1$ ,  ${}^5\text{D}_0 \rightarrow {}^7\text{F}_2$ ,  ${}^5\text{D}_0 \rightarrow {}^7\text{F}_3$ ,  ${}^5\text{D}_0 \rightarrow {}^7\text{F}_4$ , and  ${}^5\text{D}_0 \rightarrow {}^7\text{F}_5$  transitions of  $\text{Eu}^{3+}$ , suggesting that excitation of the  ${}^7\text{F}_0 \rightarrow {}^5\text{D}_4$  transition of  $\text{Tb}^{3+}$  at 487 nm populates the emissive  ${}^5\text{D}_0$  state of  $\text{Eu}^{3+}$ . This phenomenon was reported for complex **4.2**, although the published emission spectra only

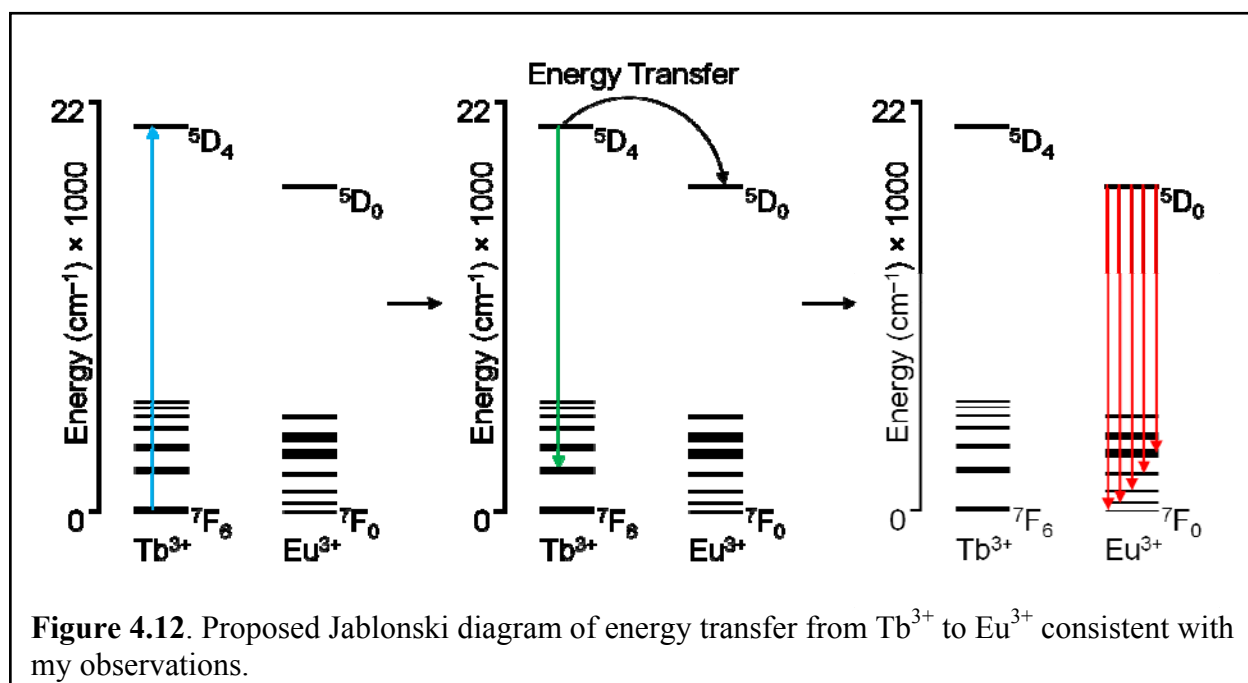
displayed a 580 to 620 nm range, where  $\text{Tb}^{3+}$  and  $\text{Eu}^{3+}$  emission peaks overlap.<sup>114</sup> The major transition in the  ${}^5\text{D}_0 \rightarrow {}^7\text{F}_2$  manifold appeared at 612 nm in both  $\text{Eu}^{3+}$ - and  $\text{Tb}^{3+}$ -centered excitation spectra, and the transition at 616 nm, which I assigned to  $\text{Eu}_2\text{L}$ , **4.7**, was substantially weaker in the spectrum of **4.6**, further indicating that the source of  $\text{Eu}^{3+}$ -based emission peaks with 545 nm excitation was **4.6**. Interestingly, the presence of the  $\text{Tb}^{3+}$ -based transition at 545 nm *and* the  $\text{Eu}^{3+}$  based transitions suggested that the emissive process from  ${}^5\text{D}_4$  to  ${}^7\text{F}_5$  and the energy transfer process from  ${}^5\text{D}_4$  to  ${}^5\text{D}_0$  are occurring at similar rates. Future experiments to determine the decay rates of the emissive processes would be useful to corroborate this observation.

Given that the  ${}^5\text{D}_0$  state of  $\text{Eu}^{3+}$  is approximately  $3100\text{ cm}^{-1}$  lower in energy than the  ${}^5\text{D}_4$  state of  $\text{Tb}^{3+}$ , it is reasonable to assume that energy transfer from  ${}^5\text{D}_4$  ( $\text{Tb}^{3+}$ ) to  ${}^5\text{D}_0$  ( $\text{Eu}^{3+}$ ) would occur given a sufficiently small interatomic distance. Given the strong dependence of energy transfer on distance, it is unlikely that intramolecular energy transfer occurs at the low concentrations of these solutions. Therefore, energy transfer that I have observed from  $\text{Tb}^{3+}$  to  $\text{Eu}^{3+}$  implied that the  $\text{Tb}^{3+}$ - $\text{Eu}^{3+}$  distance was within the  $10\text{ \AA}$  range required for Förster resonance energy transfer. With the luminescence decay data for **4.7** presented in Chapter 3, this result further supported the calculated structure of  $\text{Eu}_2\text{L}$ , **4.7**, and suggested that  $\text{TbEuL}$ , **4.6**, has a similar structure.

### Summary and Conclusion

I have reported the synthesis of a new heterodimetallic complex **4.6** that contains  $\text{Eu}^{3+}$  and  $\text{Tb}^{3+}$  and exhibits efficient Ln–Ln energy transfer. The presence of complex **4.6** was confirmed by ESIMS analysis and was corroborated by luminescence spectral analysis. The energy transfer phenomenon was demonstrated by observing  $\text{Eu}^{3+}$ -based emission with direct

excitation of  $\text{Tb}^{3+}$ , representing direct observation of intramolecular Ln–Ln energy transfer. A diagram of a possible energy transfer mechanism consistent with my observations is illustrated in **Figure 4.11**. The efficiency of energy transfer, though not directly measured, must be high to observe  $\text{Eu}^{3+}$  emission from direct  $\text{Tb}^{3+}$  excitation. High efficiency energy transfer is the first direct empirical evidence that the Ln–Ln distance is within 10 Å, suggesting that the optimized structure of **4.7** reported in Chapter 3 represents the solution-state structure of these complexes. Finally, these results suggest that bridged-lanthanide structures are possible for numerous combinations of lanthanides, allowing optimization of the excitation wavelength, emission wavelength, and lifetime properties for imaging applications.



## CHAPTER 5: Summary, Conclusions, and Future Directions

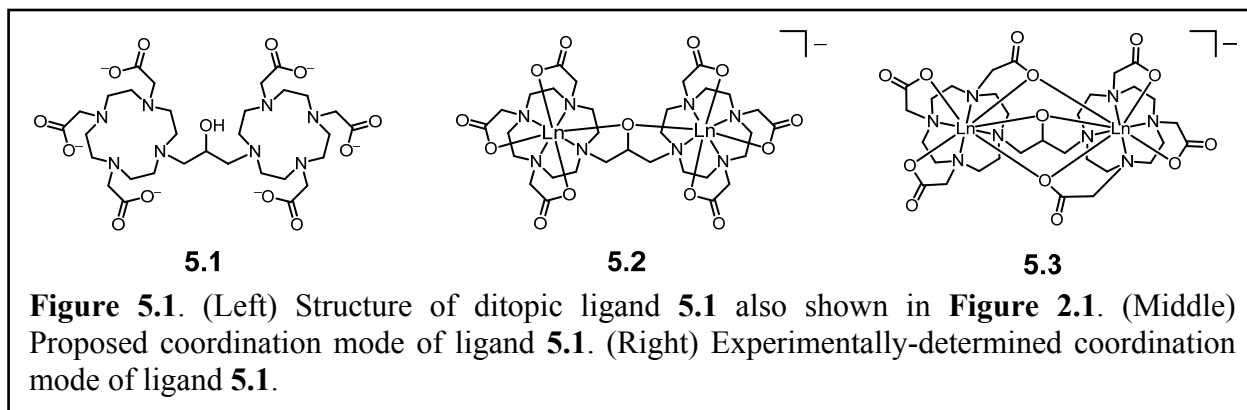
### Introduction

Studies of multimetallic lanthanide ( $\text{Ln}^{3+}$ ) complexes relating to imaging applications have been reported extensively to study properties relevant to contrast agents for magnetic resonance imaging (MRI), probes for luminescence imaging, and biological interactions.<sup>34, 35, 44–50, 72, 73, 83–87</sup> Interestingly, the properties of some multimetallic lanthanide systems differ from their monometallic counterparts, though few systems exhibit direct  $\text{Ln}^{3+}$ – $\text{Ln}^{3+}$  interactions.<sup>83, 113–115</sup> An absence of focus on  $\text{Ln}^{3+}$  complexes that might exhibit properties different or greater than the sum of the  $\text{Ln}^{3+}$  chelates linked together prompted my approach to contribute studies clearly focused on complexes that would likely feature  $\text{Ln}^{3+}$ – $\text{Ln}^{3+}$  interactions. The goals of my research were to design, synthesize, and study the structural, magnetic, and luminescence properties of a dimetallic  $\text{Ln}^{3+}$  complex that I hypothesized would have an unprecedented degree of  $\text{Ln}^{3+}$ – $\text{Ln}^{3+}$  interaction. These goals were aimed at elucidating new properties of  $\text{Ln}^{3+}$  complexes with a particular focus on factors affecting MRI and luminescence imaging.

### Ligand Design

I designed a ditopic ligand containing a 2-propanolyl moiety bridging two 1,4,7,10-tetraazacyclododecane-(1,4,7-triacetate) macrocycles that I hypothesized would chelate and bridge two lanthanide ions through an alcohol or alkoxide oxygen atom (**Figure 5.1**). This hypothesis was based on previous reports of stable lanthanide complexes with cyclen-based polyaminopolycarboxylate ligands and the preference of lanthanides for coordination that forms 5-membered rings. I further supposed that a single-atom bridge between  $\text{Ln}^{3+}$  ions chelated in this ligand would result in small  $\text{Ln}^{3+}$ – $\text{Ln}^{3+}$  distances, leading to new luminescence and magnetic properties that could be applied to problems in biological and medical imaging. Interestingly,

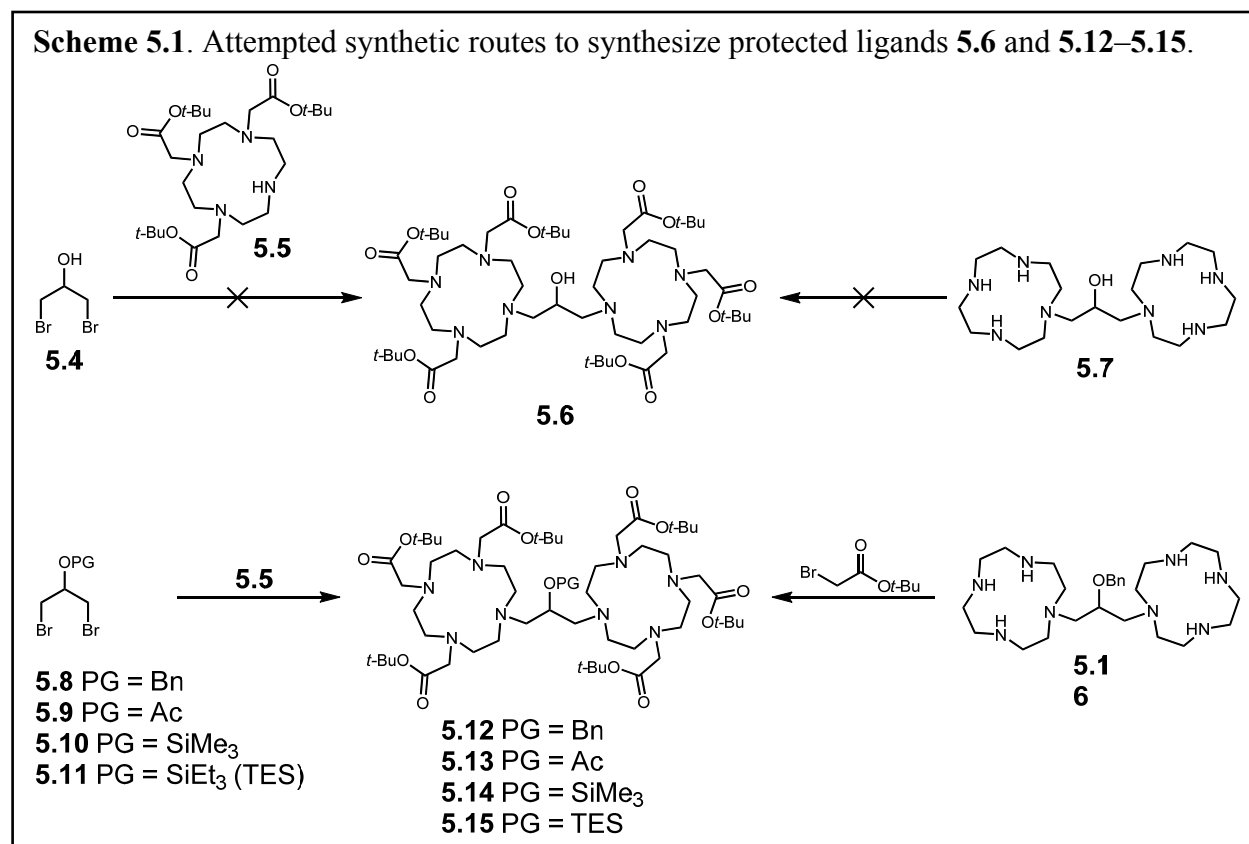
after analyzing the luminescence data of the  $\text{Eu}^{3+}$  complex and proposing structure **5.2** to Dr. Cisneros, he calculated the optimized structure, **5.3**, that contained two additional  $\mu$ -oxygen atoms (**Figure 5.1**). Though **5.3** was a departure from the structure I expected, I was able to use this complex to study Ln–Ln interactions.



### Ligand Synthesis

I proposed that the synthesis of **5.1** could be achieved through hexa-*tert*-butyl ester intermediate **5.6** (**Scheme 5.1**). However, attempts to synthesize **5.6** in one step starting from 1,3-dibromo-2-propanol (**5.4**) and DO3A-*tris-tert*-butyl ester (**5.5**) were unsuccessful. An alternative method to synthesize and alkylate **5.7** yielded ambiguous results due to the possibility that the alcohol might have been alkylated. Compound **5.16** was synthesized and successfully converted to **5.12** but **5.1** was not generated from this route due to unsuccessful conversion of the benzyl ether to an alcohol. However, due to the successful formation of **5.12** from **5.16**, I hypothesized that **5.12** could be synthesized by reacting the benzyl derivative of **5.4**, **5.8**, with **5.5**. The success of this reaction indicated that the alcohol could be masked with a protecting group without hindering the substitution of 1,3-dibromo-2-propanol derivatives. Therefore, I prepared a series of protected 1,3-dibromo-2-propanol intermediates, **5.8** – **5.11**, and screened them in reactions with **5.5**. The intermediate **5.11** successfully furnished **5.15**, confirming that

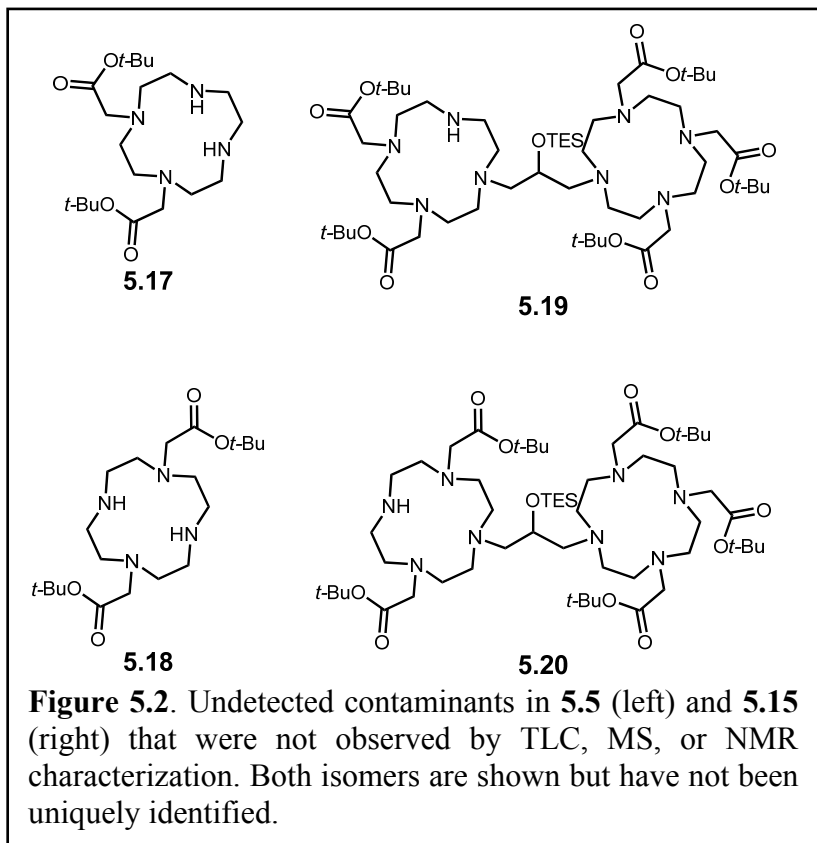
steric interference by the protecting group was not as important as I initially assumed. Side products that interfered with purification in previous attempts were limited and the chromatographic properties of **5.15** were unique enough that separation was achieved. As expected, global deprotection of intermediate **5.15** generated H<sub>6</sub>**5.1**.



### Comments on Synthetic Methods

Though several routes to synthesize **5.1** were not successful, exploring these reactions allowed me to develop practical methods of monitoring these reactions. Specifically, I found that monitoring these reactions with thin layer chromatography (TLC) was only useful for determining the consumption of 1,3-dibromo-2-propanol or its derivatives, which was usually not indicative of product formation. Also, the cyclen-containing moieties did not chromatograph cleanly, making isolation of the components of these reactions challenging if not impossible. I found that the most reliable method to monitor product formation in these reactions was using

electrospray-ionization mass spectrometry. However, this method was also limited because some components could not be detected. An example of this limitation occurred when 5-arm analogs of **5.15**, **5.19** and **5.20**, were not detected and were unknowingly present through deprotection and metallation reactions (**Figure 5.2**). The presence of **5.19** and **5.20** were only observed by high performance liquid chromatography of the resulting metal complexes. The presence of these products highlighted the importance of eliminating 2-arm impurities, **5.17** and **5.18**, in the synthesis of **5.5** and highlighted the limitations of TLC, mass spectrometry, and NMR spectroscopy. None of these techniques suggested the presence of 2-arm contaminants in **5.5** or 5-arm contaminants in **5.15**.

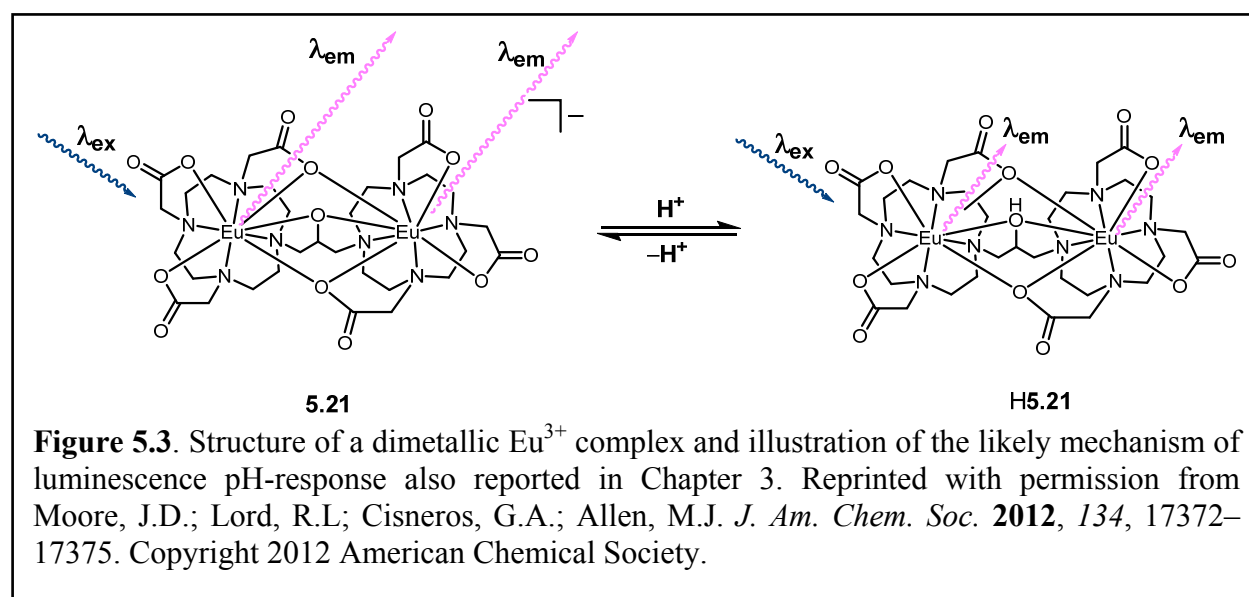


### Dimetallic $\text{Eu}^{3+}$ -complex for Concentration-Independent pH Detection

Using ligand **5.1**, I synthesized a dimetallic  $\text{Eu}^{3+}$  complex that I determined did not contain water molecules coordinated to the  $\text{Eu}^{3+}$  ions. This result was unexpected given the expected structure **5.2** and the fact that  $\text{Eu}^{3+}$  is usually 9-coordinate. However, the lack of coordinated water suggested that the  $\text{Eu}^{3+}$  ions were bridged by the alcohol. Calculation of the

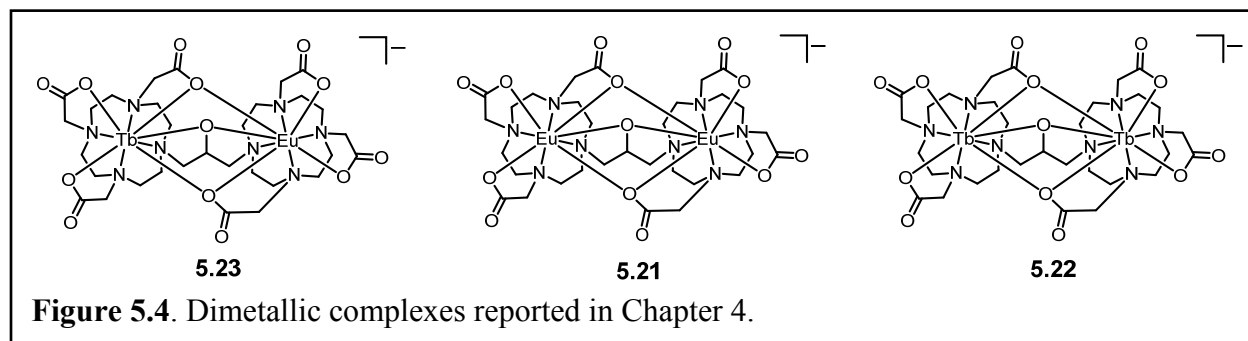
optimized structure revealed two additional bridging atoms from the carboxylate arms, consistent with the absence of coordinated water molecules (**Figure 5.3**).

Confident that a  $\text{Eu}^{3+}\text{-Eu}^{3+}$  bridge had formed, I expected that the protonation state of the bridging alcohol, and, therefore, the presence of a hydroxyl oscillator in the  $\text{Eu}^{3+}$  coordination sphere, would be modulated by pH. Because the luminescence-decay rate of  $\text{Eu}^{3+}$  is dependent on the number of hydroxyl oscillators in the coordination sphere, I hypothesized that the luminescence-decay rate of  $\text{Eu}^{3+}$  in **5.21** would change with pH. Further, I expected that the luminescence response to pH would be independent of **5.21** concentration. By measuring the luminescence-decay rate of 0.50 mM and 1.0 mM solutions of **5.21** at different pH values, I confirmed my hypotheses that the luminescence-decay rate of **5.21** changes with pH and that the pH response does not depend on the concentration of **5.21**. These results demonstrated a new approach to sensing pH, wherein a property known to be independent of probe concentration could be used to address limitations of sensing techniques: namely, the need to know the concentration of the probe. This example also represented a new mechanism of pH-response (**Figure 5.3**) that could provide a boon to biological imaging.



### Intramolecular Lanthanide–Lanthanide Energy Transfer in a Heterodimetallic Complex

After I determined that the tri-bridged configuration was likely representative of the solution-state structure of **5.21** and demonstrated the utility of this complex, I sought a method to unequivocally confirm that two lanthanide ions chelated in **5.1** could interact. I hypothesized that a Ln–Ln interaction would be observed in the form of luminescence energy transfer between  $\text{Tb}^{3+}$  and  $\text{Eu}^{3+}$  in adjacent sites of **5.1**. This phenomenon would require that the  $\text{Ln}^{3+}$  ions are within 10 Å; therefore, observation of energy transfer would also indicate that the  $\text{Ln}^{3+}$  ions are likely bridged. To test these hypotheses, I synthesized and characterized complexes **5.21**, **5.22**, and **5.23** (**5.23** was isolated as a mixture of **5.23** and **5.21**). By comparing excitation and emission spectra of solutions of each complex, I determined that excitation of  $\text{Tb}^{3+}$  resulted in emission from  $\text{Eu}^{3+}$ . This result indicated that intramolecular Ln–Ln energy transfer occurred in complex **5.23** from the  $^5\text{D}_4$  excited state of  $\text{Tb}^{3+}$  to the  $^5\text{D}_0$  excited state of  $\text{Eu}^{3+}$ . Observation of energy transfer confirmed that ligand **5.1** brings two  $\text{Ln}^{3+}$  ions within 10 Å, and likely closer. The excitation and emission data also represent the most direct observation of  $\text{Ln}^{3+}$ – $\text{Ln}^{3+}$  energy transfer yet reported. Further, these results expand the utility of  $\text{Ln}^{3+}$ -based luminescence probes by making tuning of excitation, emission, and lifetime properties to the needs of specific applications as simple as selecting the right  $\text{Ln}^{3+}$ – $\text{Ln}^{3+}$  combination.



## Future Directions

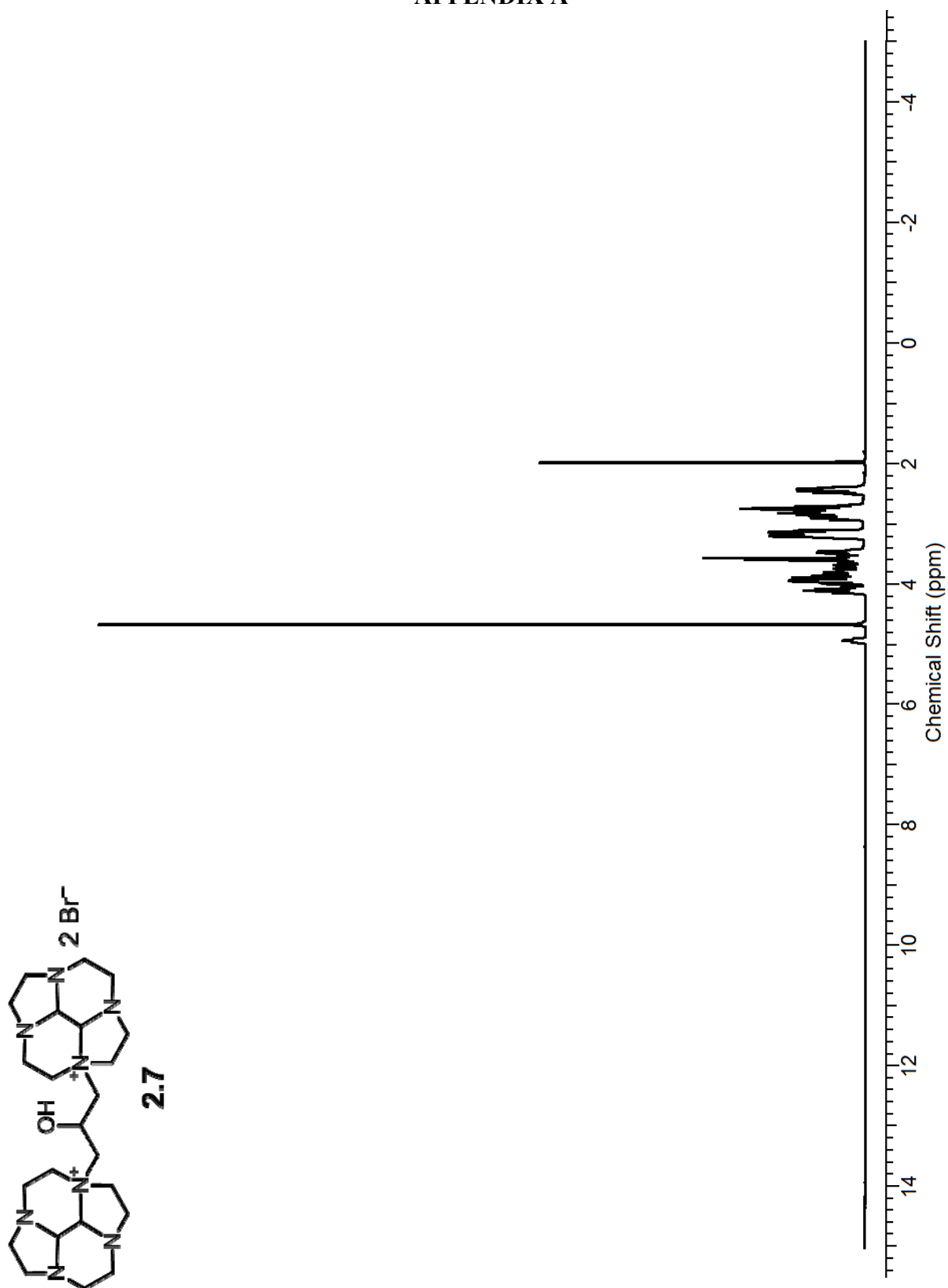
Though I have exhausted many routes to synthesize ligand **5.1**, the low yield and impurities that hamper the synthesis of pure metal complexes should be addressed. One area that could be explored is purification of **5.1** by HPLC. Optimization of the syntheses of **5.6** or a derivative that could serve as an intermediate to **5.1** are likely possible and will require the screening of many new reactions. Other derivatives of ligand **5.1**, such as an analog with amide arms, would also be interesting to determine the structural factors that are important for forming stable  $\text{Ln}^{3+}\text{-Ln}^{3+}$  bridged complexes. Finally, to unequivocally confirm the structure of these lanthanide complexes, crystallographic data should be pursued.

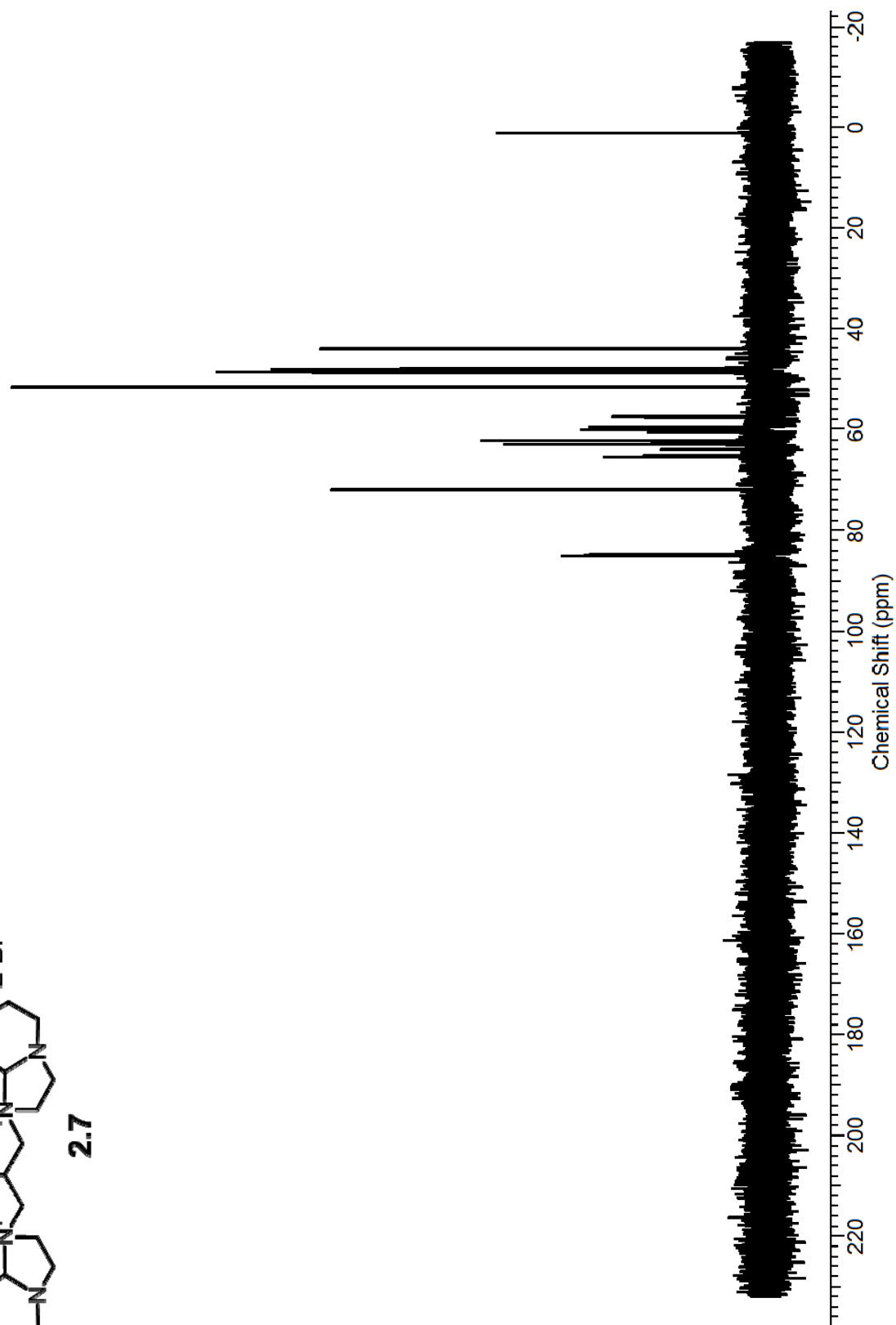
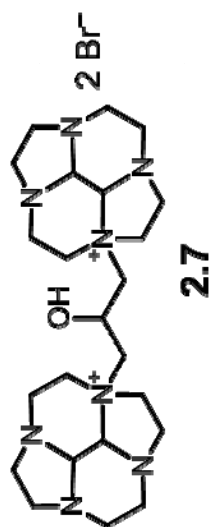
Improving the emission intensity of lanthanide complexes is often achieved by installing an organic chromophore on the chelate that will efficiently absorb and transfer photons to the  $\text{Ln}^{3+}$  ion. This approach would likely prove useful to decrease the detection limit of these probes. Low detection limits are especially important for biological applications where probe concentration needs to be minimized to avoid toxicity and interfering with the system being studied.

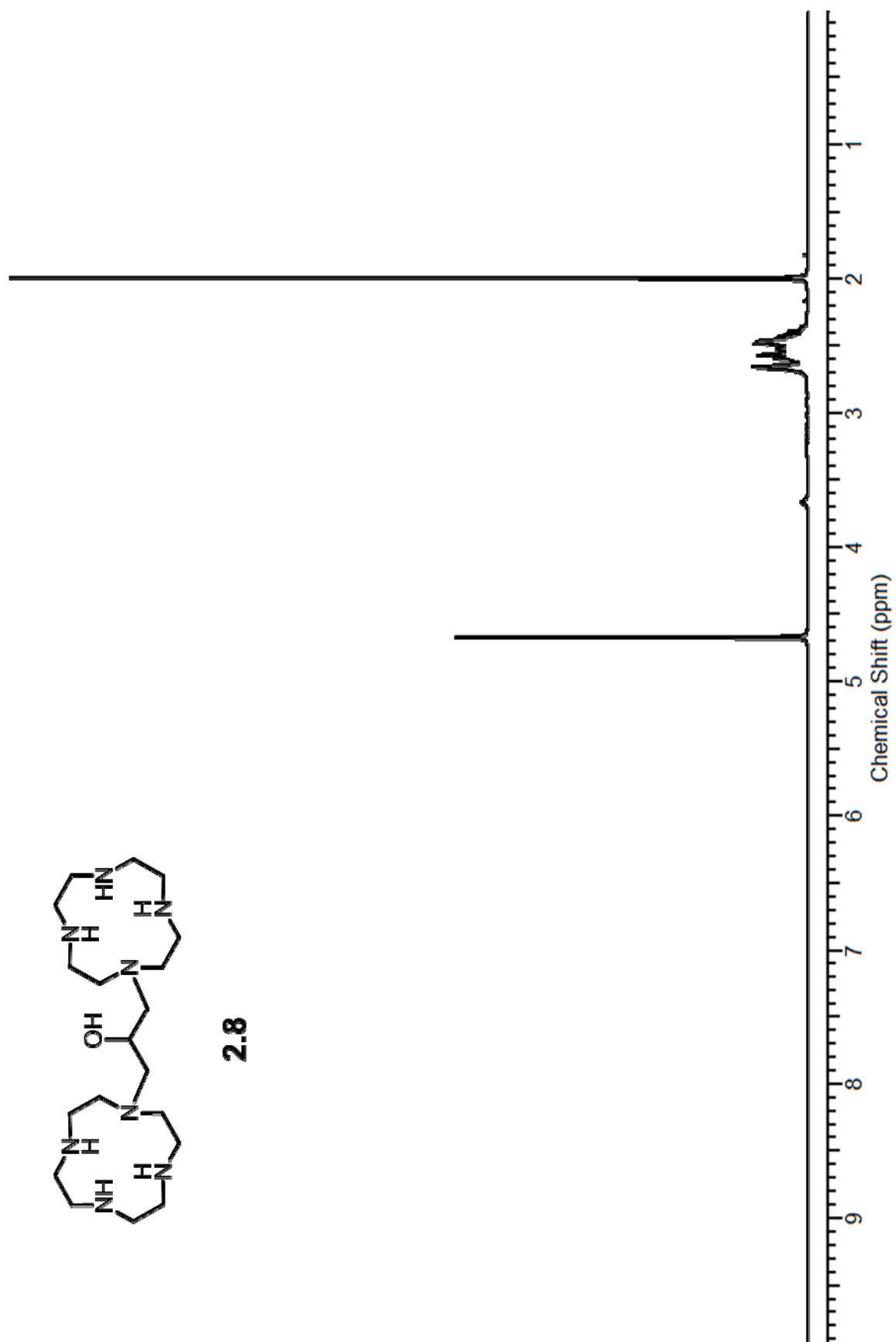
Fundamental studies on the mechanism of energy transfer would also be enlightening. The  $\text{Ln}^{3+}$  emissive states are expected to be primarily f-orbital-based, and the f-orbitals are not considered to be involved in bonding interactions; thus, I assume that the energy transfer mechanism is purely dipolar in nature. Comparing the luminescence-decay rates of **5.23** and the  $\text{Gd}^{3+}/\text{Tb}^{3+}$  analog will likely provide insight into the mechanism of energy transfer, which would be useful to elucidate the role, if any, of the bridging atoms. The utility of these complexes would be greatly expanded by demonstrating that energy transfer can occur between other pairs of  $\text{Ln}^{3+}$  ions and if the heterometallic complexes could be synthesized in pure form. The latter

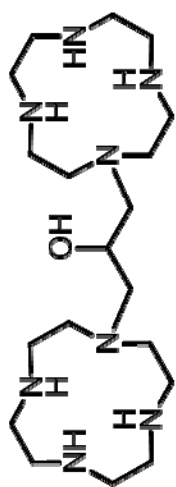
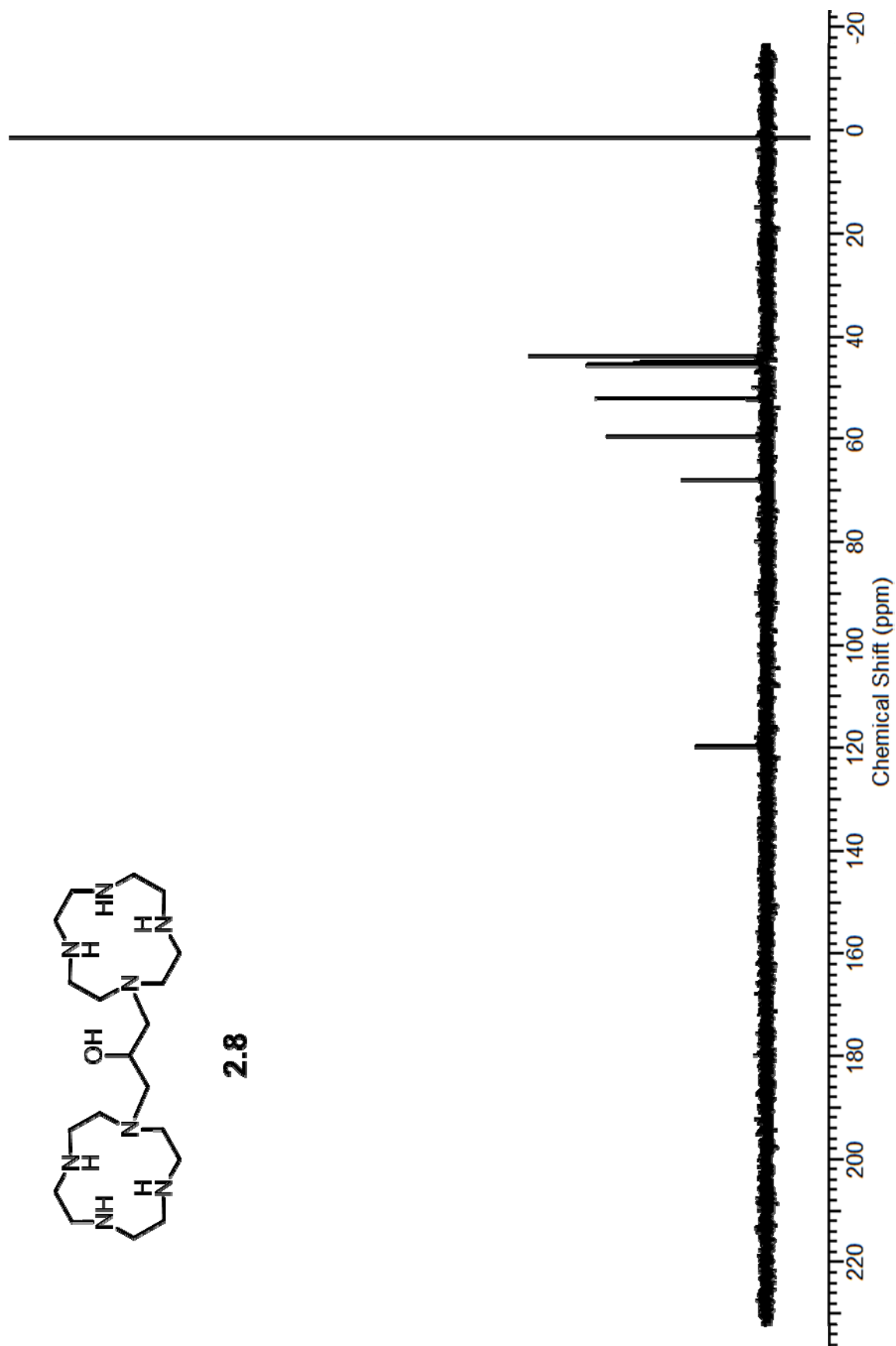
goal presents a formidable synthetic challenge, but control over heterodimetallic metallation would have tremendous implications for a wide range of disciplines ranging from medicine and biology to materials and nuclear waste applications.

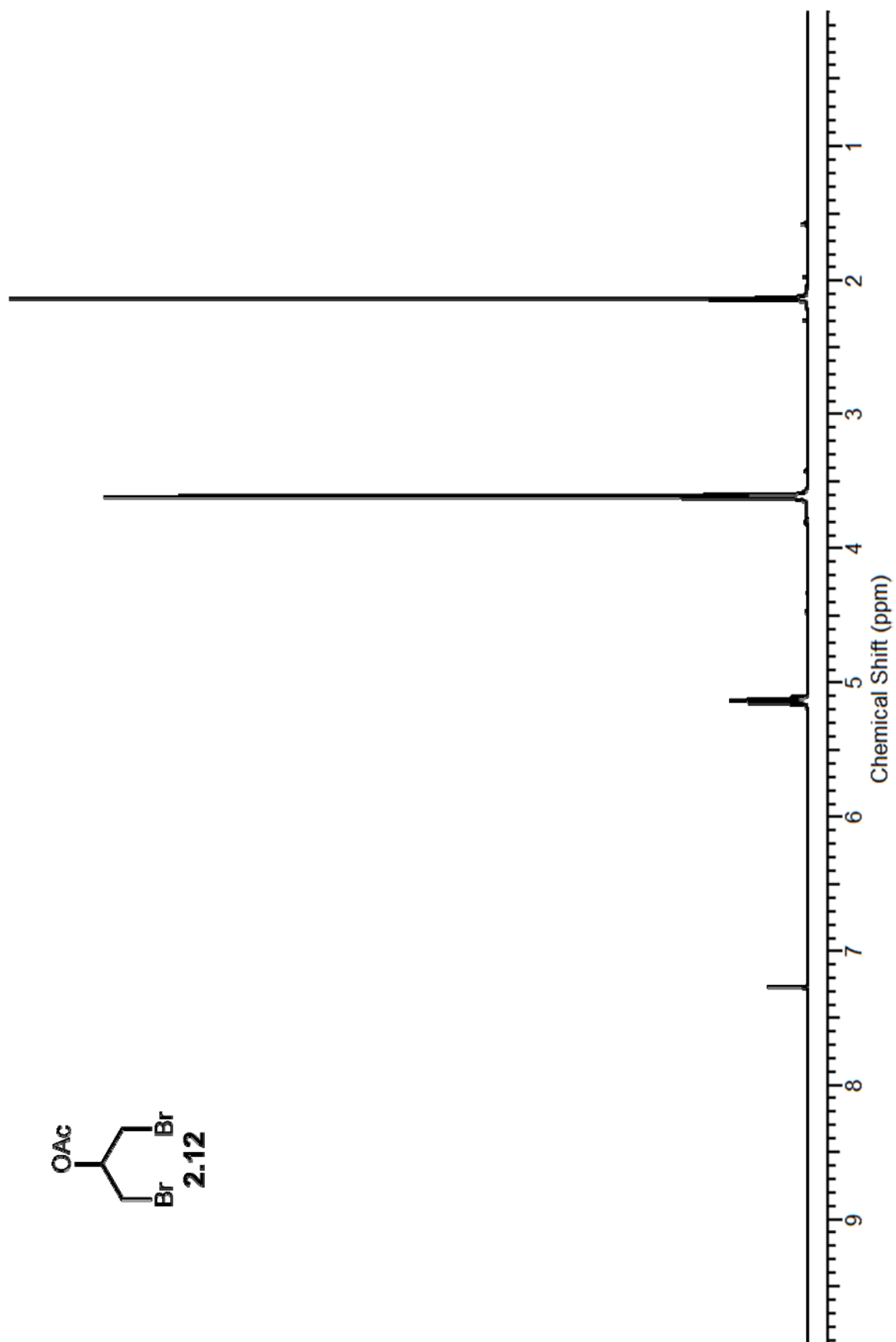
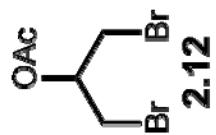
## APPENDIX A

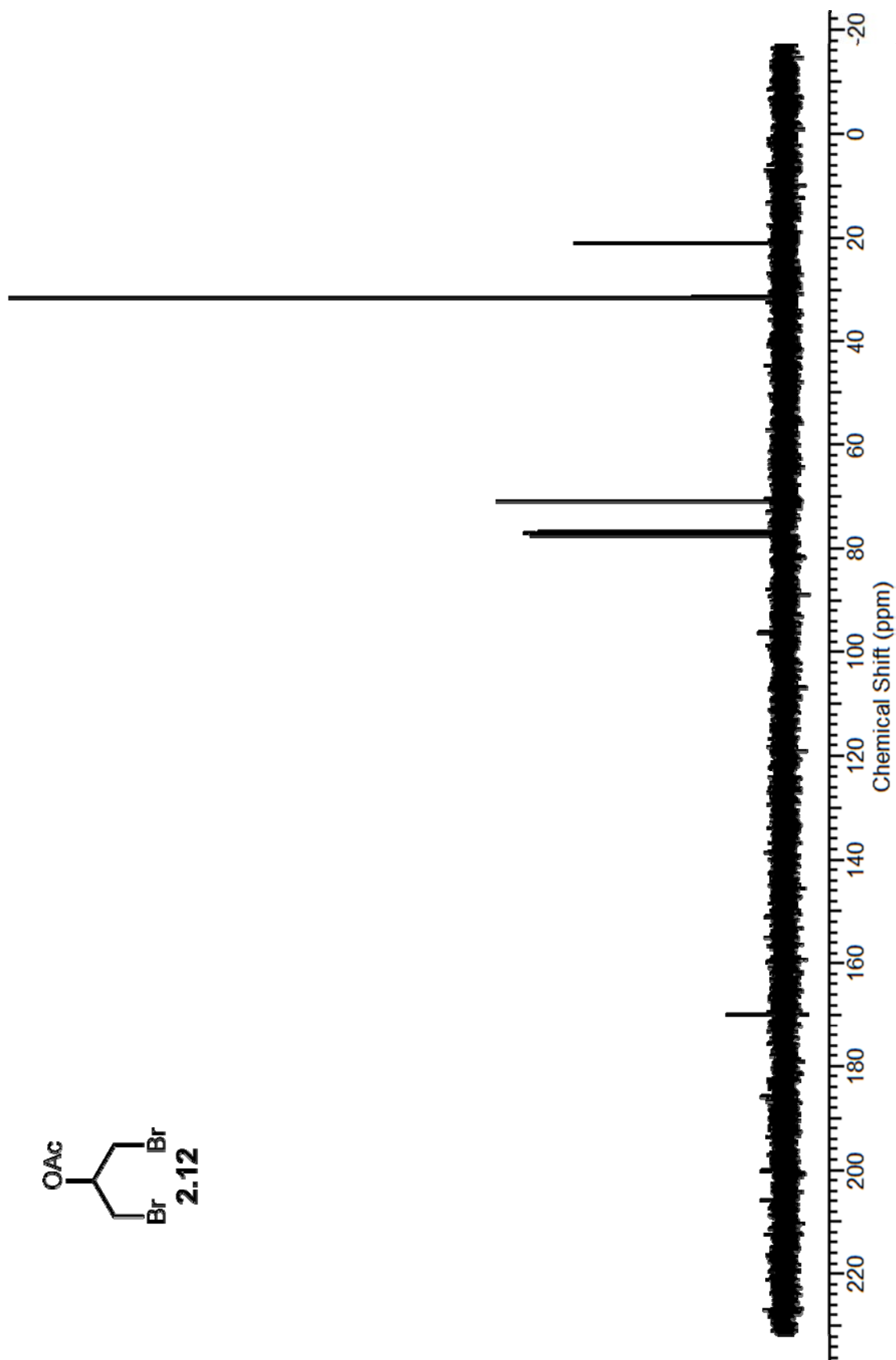
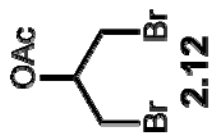


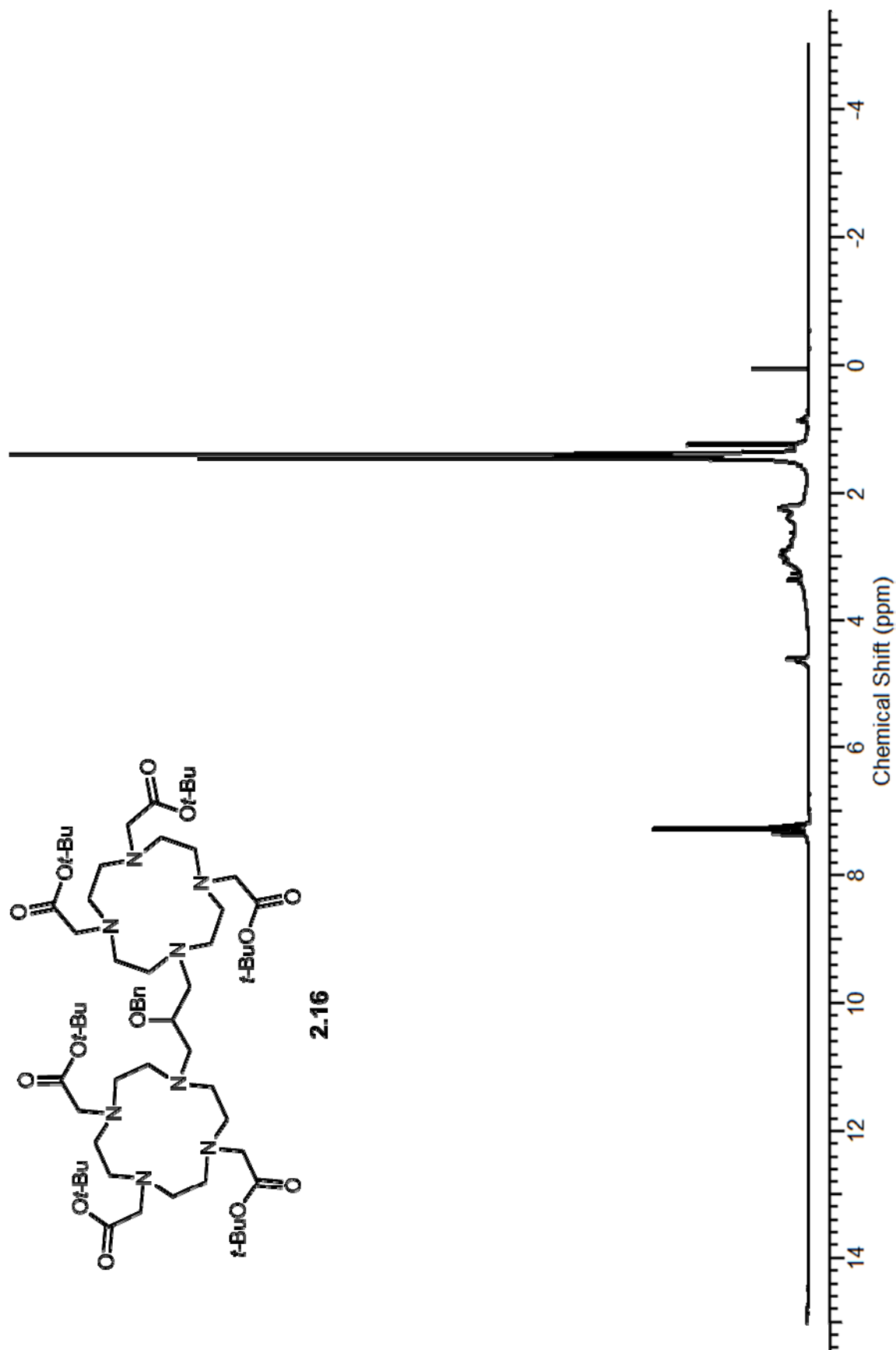


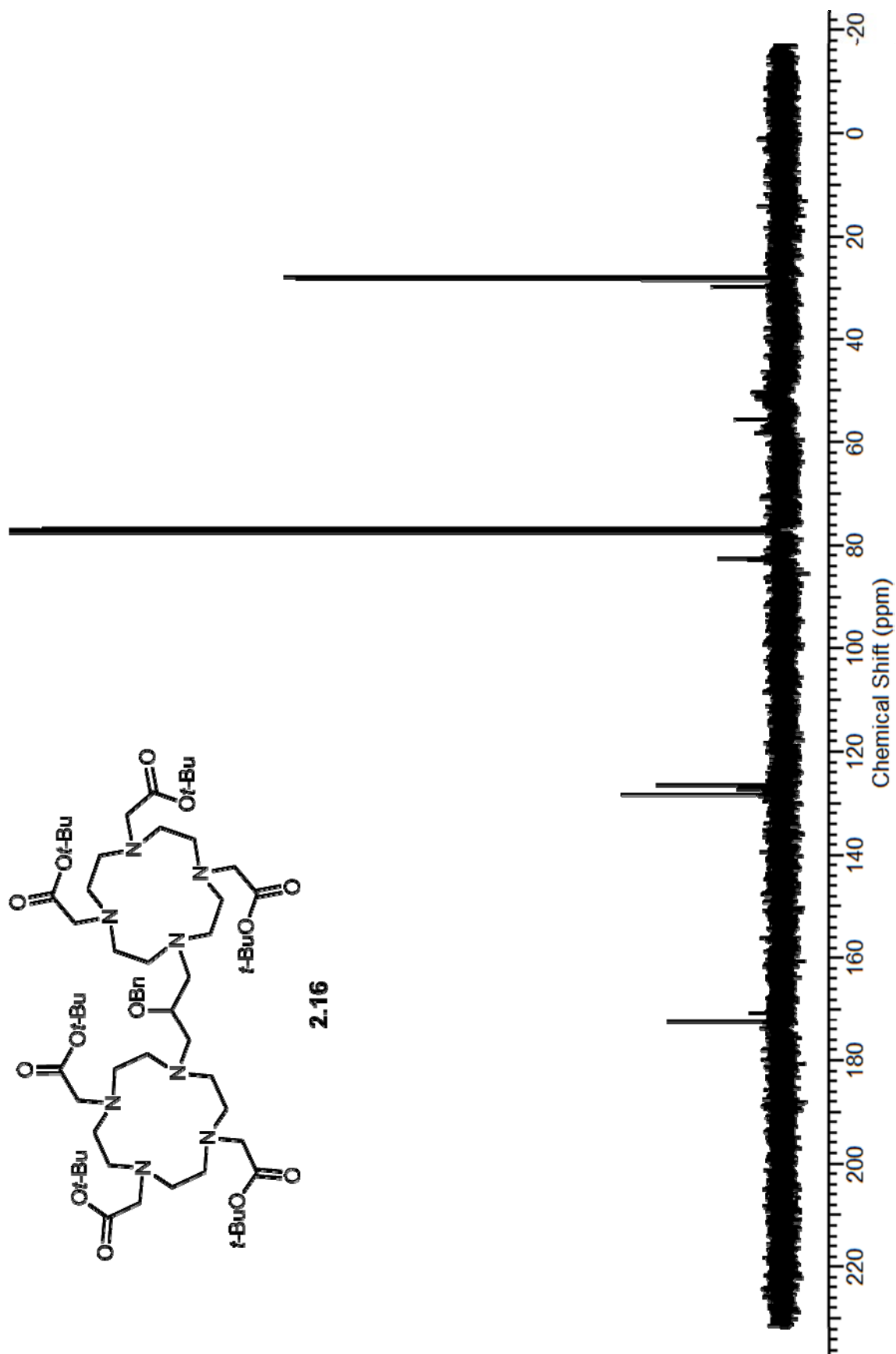


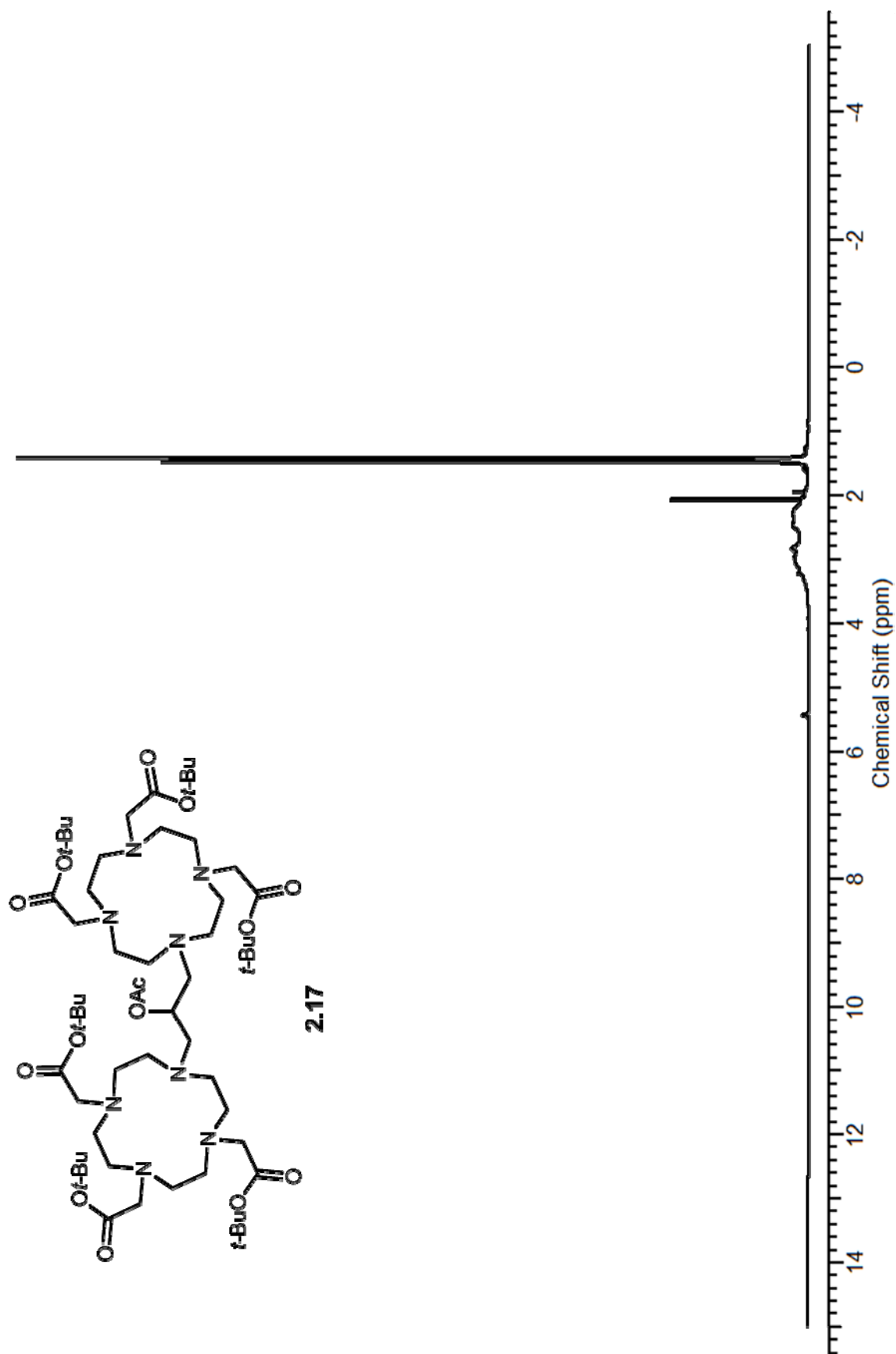
**2.8**

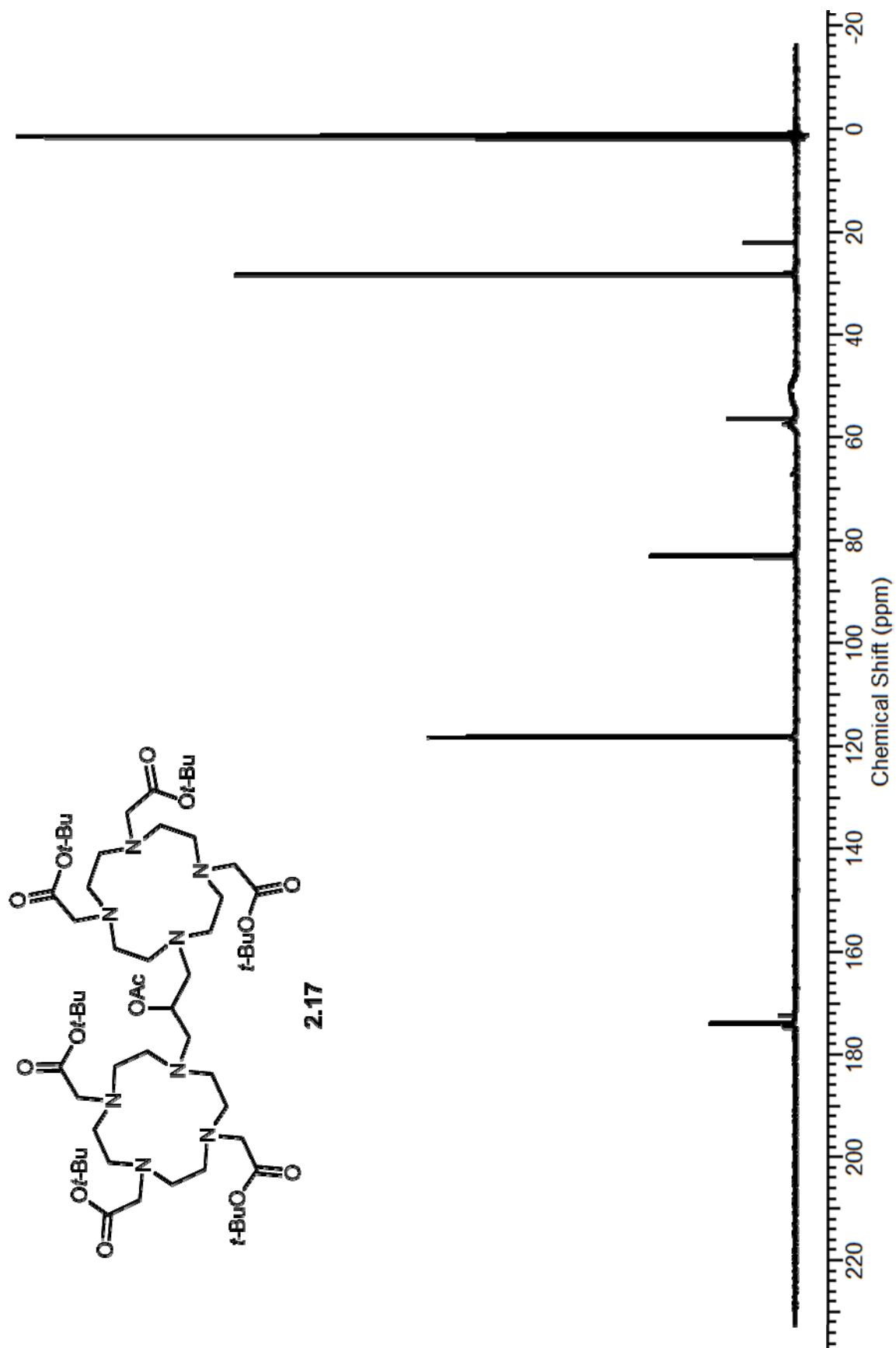






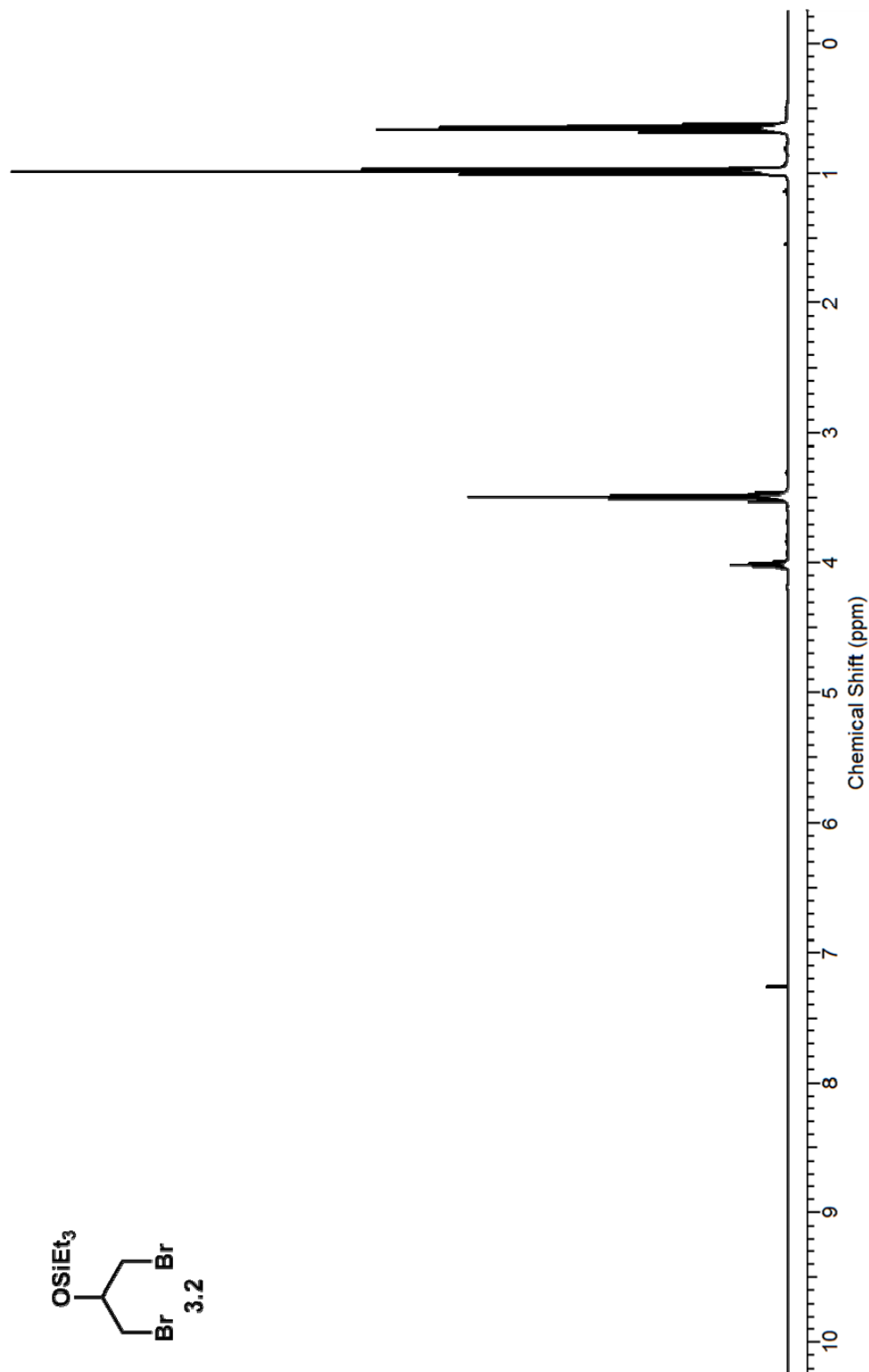


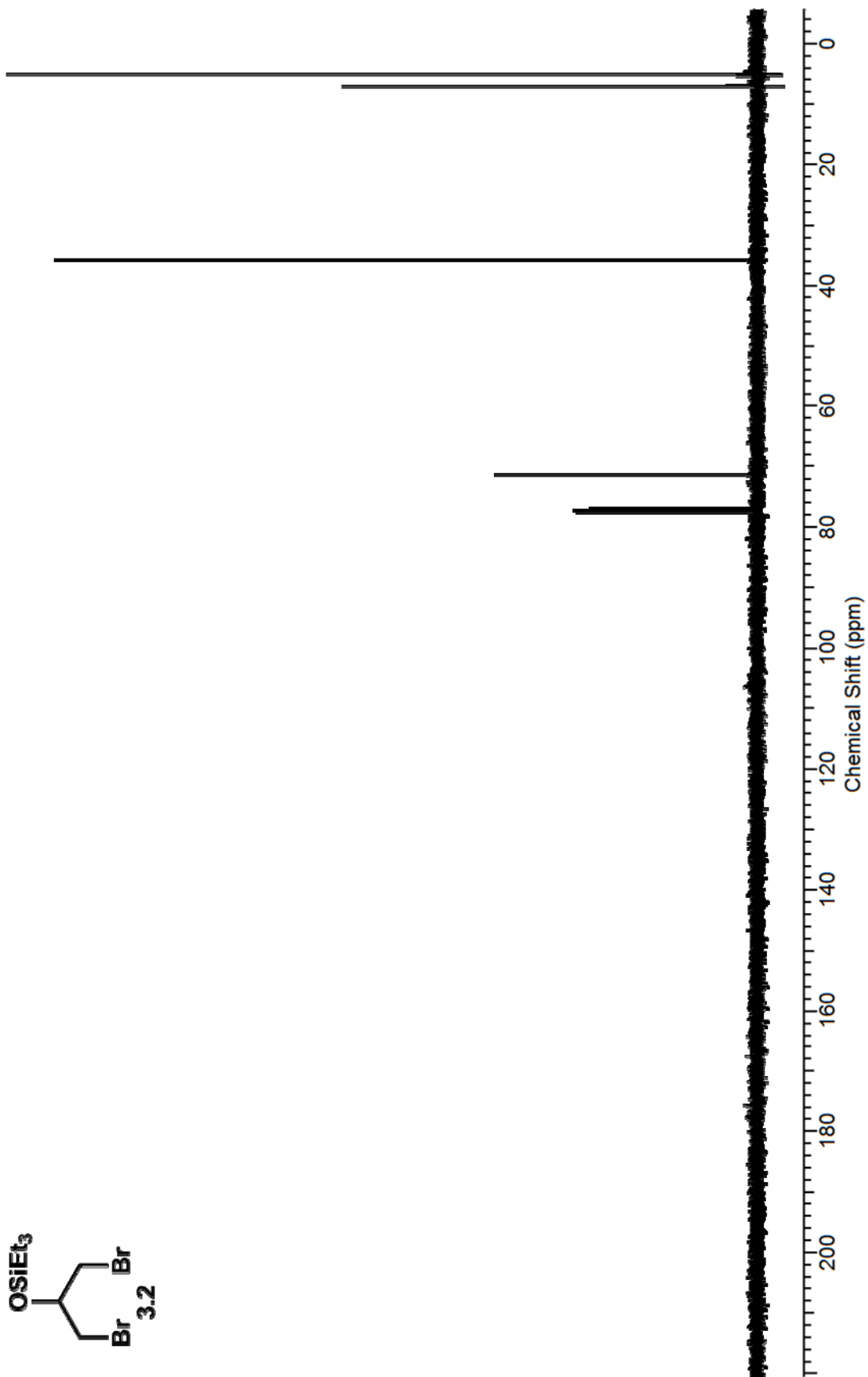
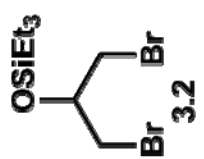


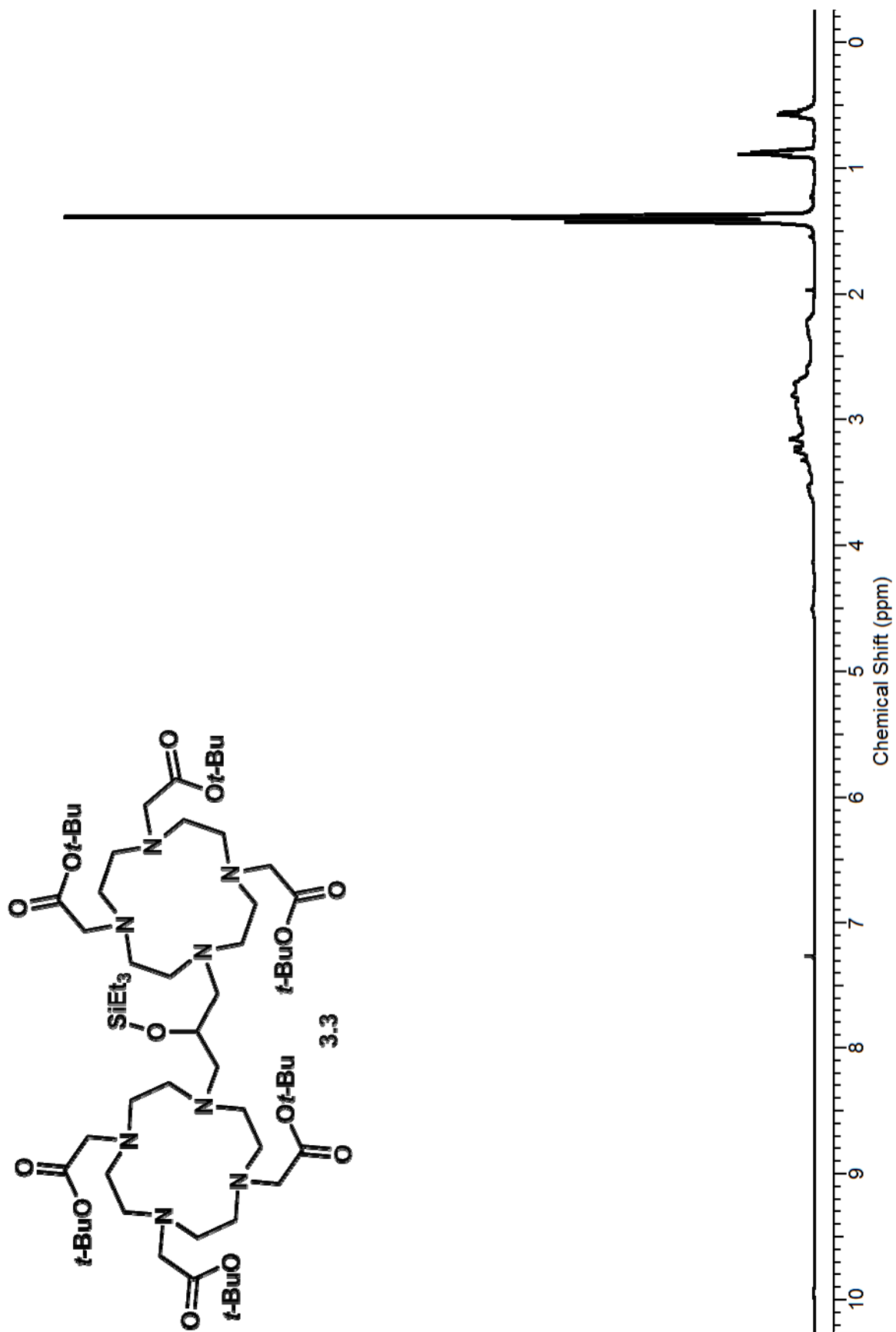


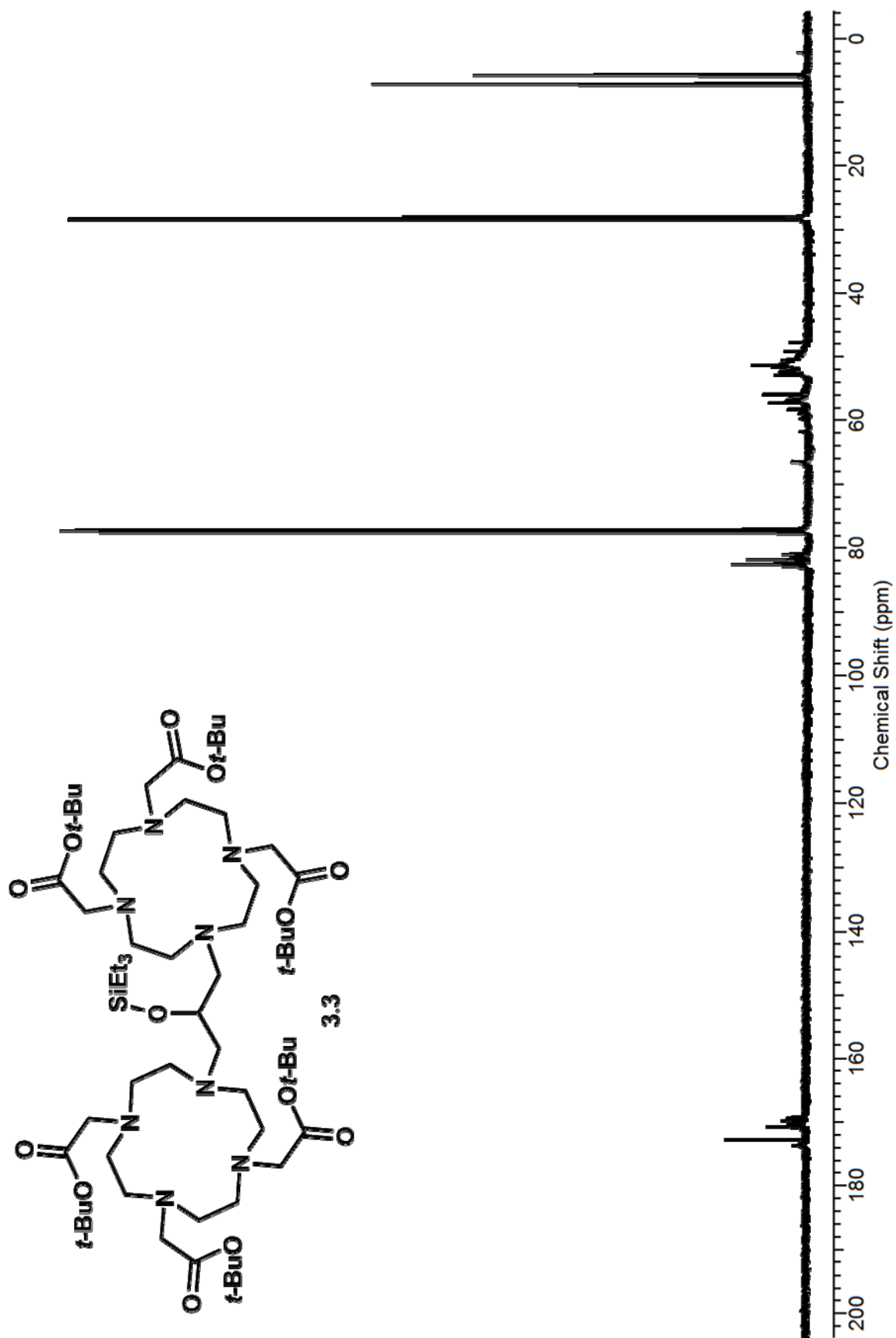
## APPENDIX B

Portions of this text have been reprinted with permission from the *Journal of the American Chemical Society*.









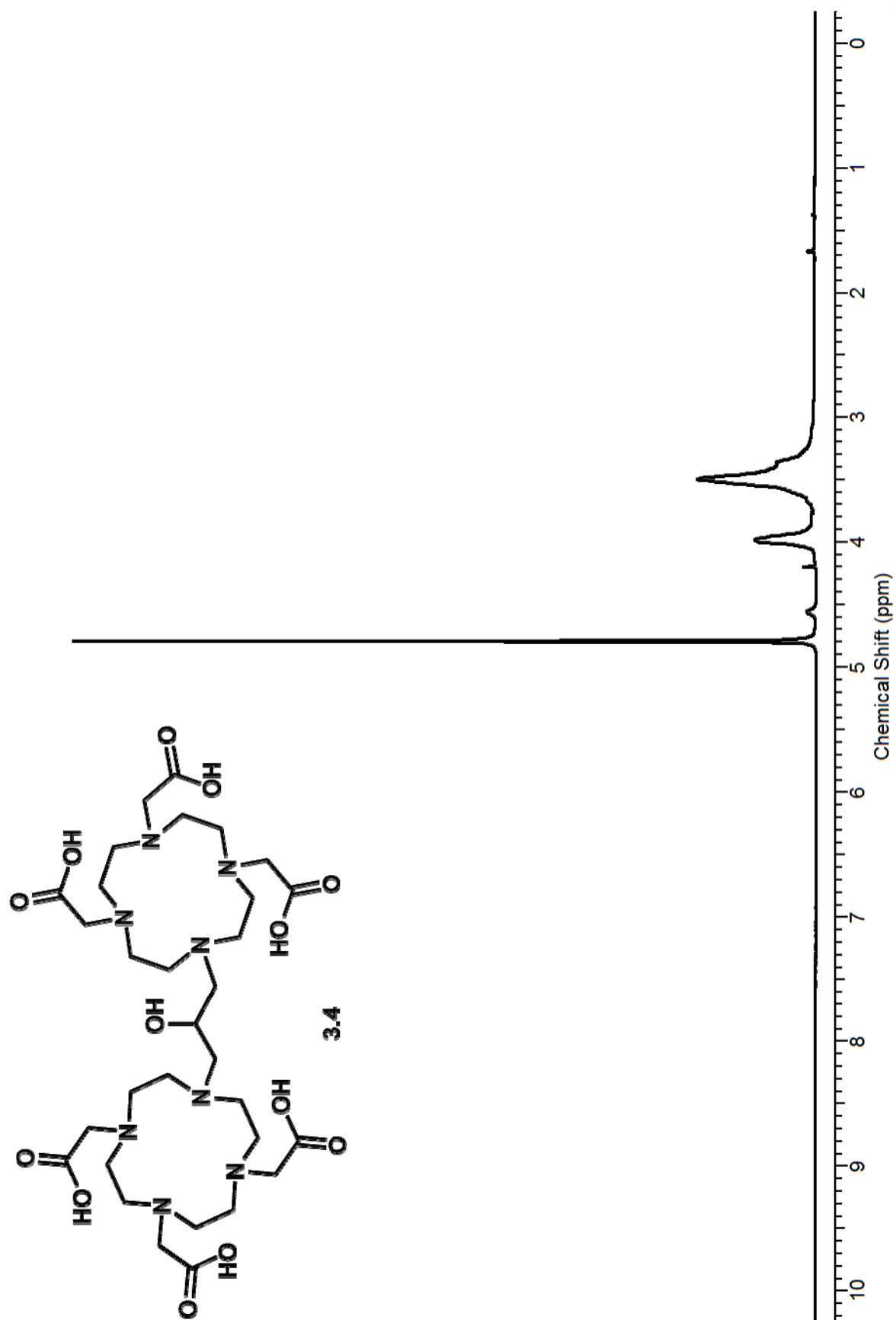


**Table B.1.** Luminescence-decay rates ( $\tau^{-1}$ ) of **3.1** at different pH values.

	<b>3.1 (0.50 mM)</b>	<b>3.1 (1.0 mM)</b>
pH	$\tau^{-1}$ (ms <sup>-1</sup> )	$\tau^{-1}$ (ms <sup>-1</sup> )
4.0	1.48	1.49
4.2	1.47	1.48
4.4	1.43	1.45
4.6	1.42	1.42
4.8	1.39	1.39
5.0	1.36	1.35
5.2	1.32	1.33
5.4	1.28	1.28
5.6	1.25	1.25
5.8	1.20	1.20
6.0	1.18	1.17
6.2	1.15	1.14
6.4	1.13	1.12
6.6	1.09	1.09
6.8	1.07	1.07
7.0	1.01	1.02
7.2	0.998	1.01
7.4	0.972	0.978
7.6	0.955	0.950
7.8	0.934	0.948
8.0	0.929	0.930

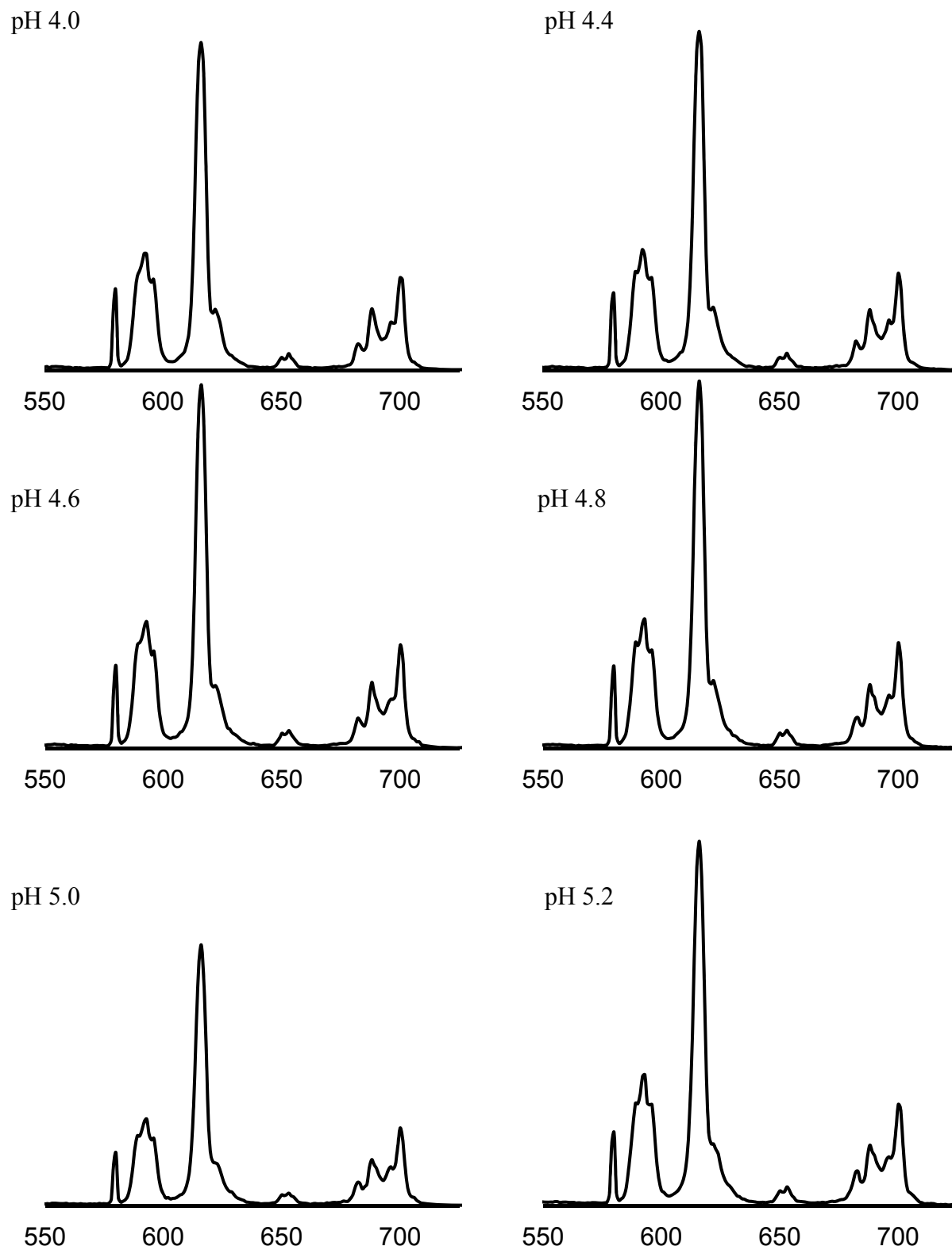
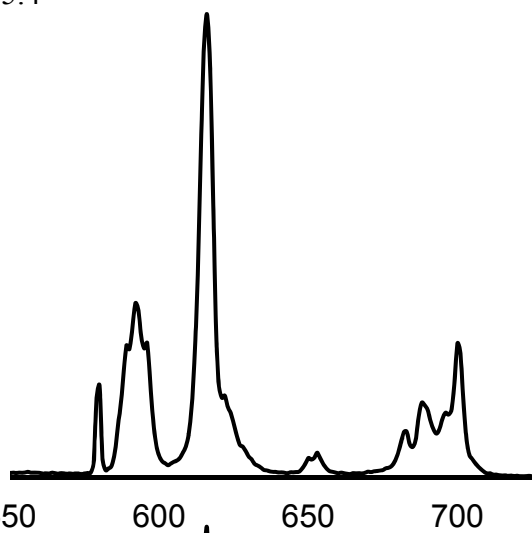
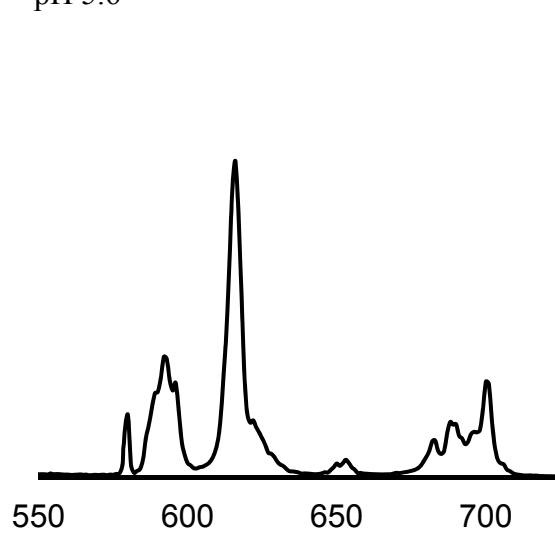


**Figure B.2.** Emission spectra of **3.1**.

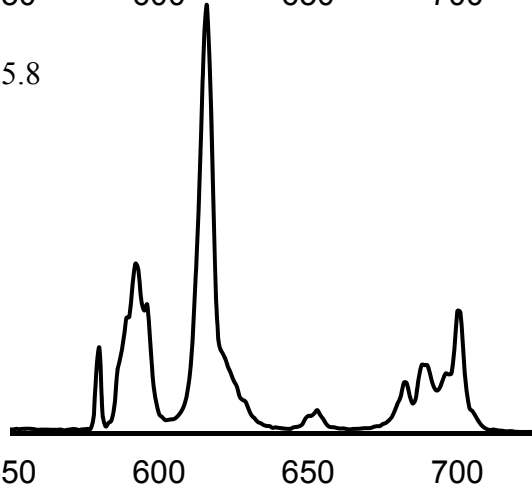
pH 5.4



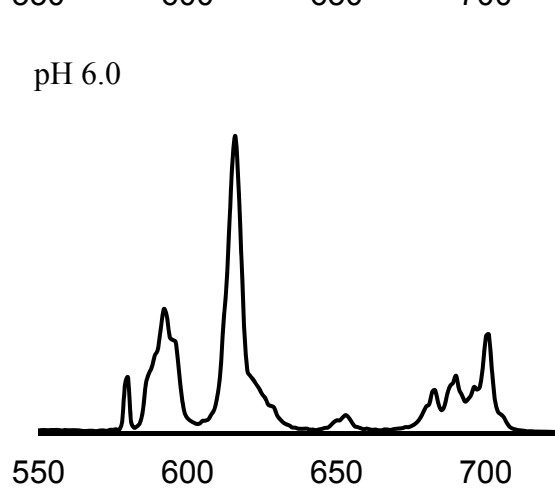
pH 5.6



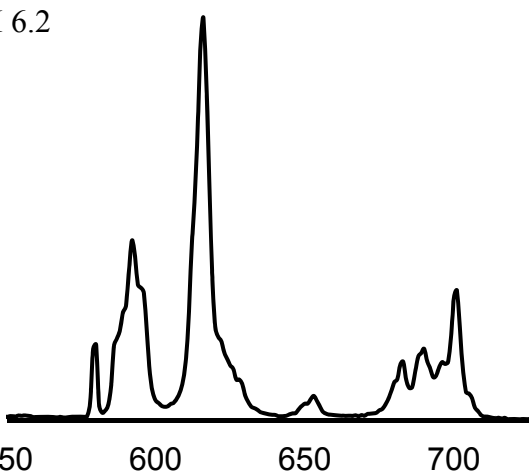
pH 5.8



pH 6.0



pH 6.2



pH 6.4

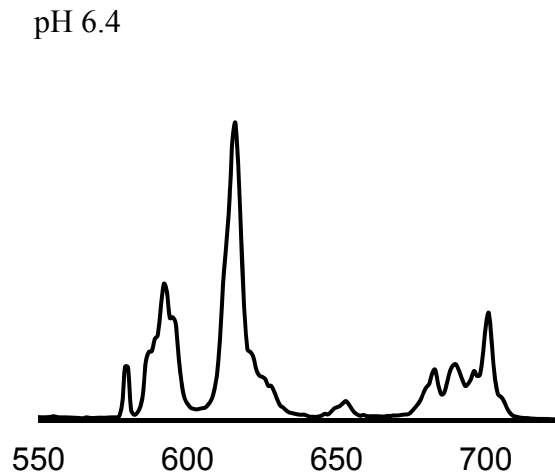
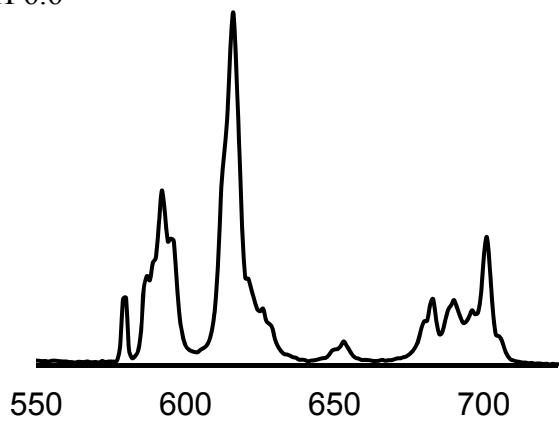
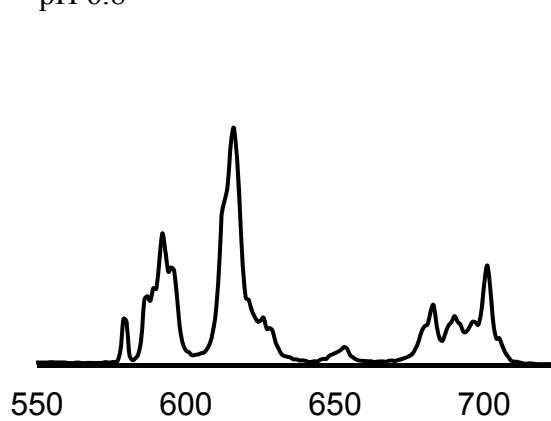


**Figure B.2 cont'd.** Emission spectra of **3.1**.

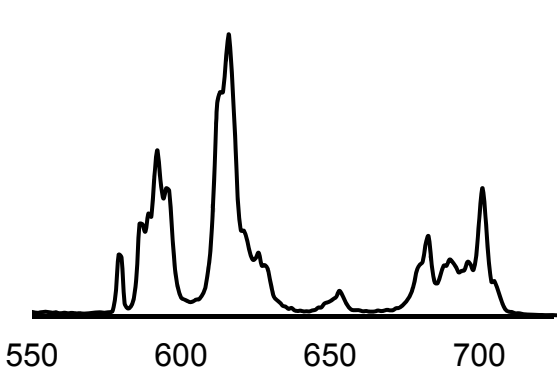
pH 6.6



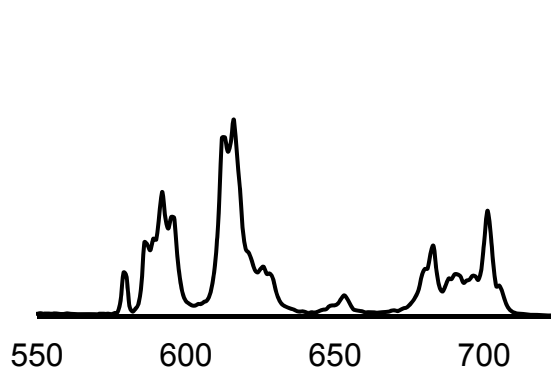
pH 6.8



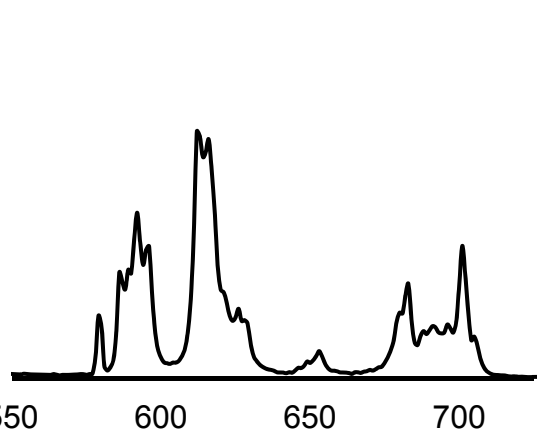
pH 7.0



pH 7.2



pH 7.4



pH 7.6

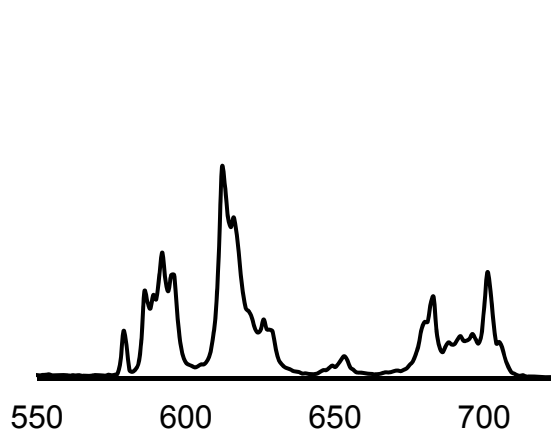


**Figure B.2 cont'd.** Emission spectra of **3.1**.

pH 7.8

pH 8.0

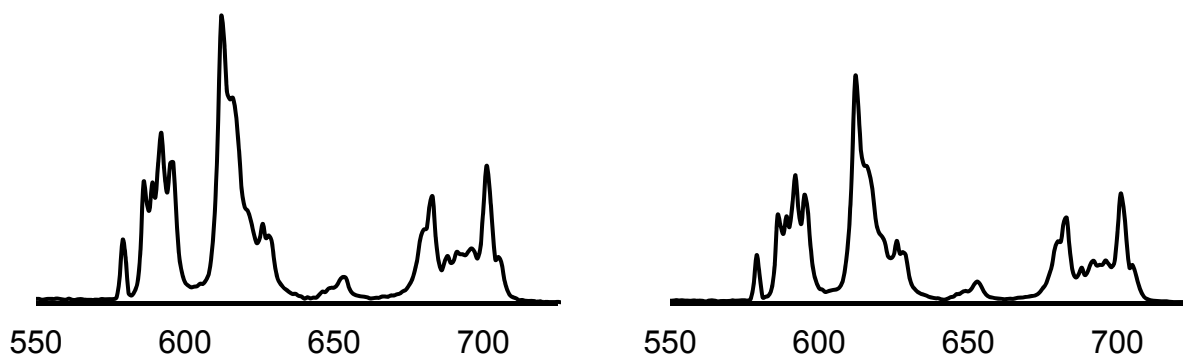


Figure B.2 cont'd. Emission spectra of 3.1.

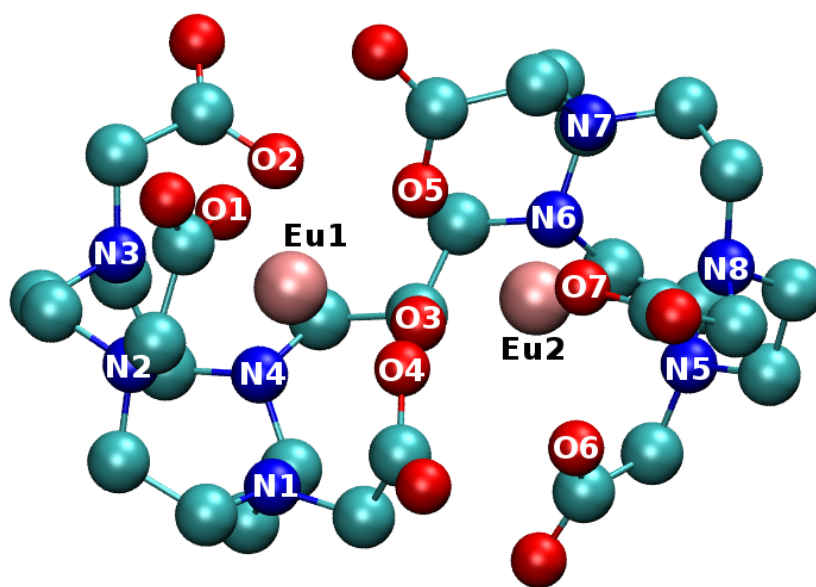


Figure B.3. Optimized computational structure of 3.1. Labels for atoms corresponding to distances in Table B.2.

**Table B.2.** Distances between the Eu(III) ions and the first coordination sphere (in Å). Distances between the Eu(III) ions and the bridging hydroxyl O have been bolded.

Distance	<b>3.1</b>	<b>H3.1</b>
Eu1-N1	2.98	2.82
Eu1-N2	2.96	2.84
Eu1-N3	2.91	2.75
Eu1-N4	2.84	2.84
Eu1-O1	2.34	2.31
Eu1-O2	2.38	2.40
<b>Eu1-O3</b>	<b>2.40</b>	<b>2.45</b>
Eu1-O4	2.42	2.44
Eu1-O5	2.49	2.48
<b>Eu2-O3</b>	<b>2.36</b>	<b>2.91</b>
Eu2-O4	2.52	2.56
Eu2-O5	2.40	2.34
Eu2-O6	2.33	2.25
Eu2-O7	2.33	2.44
Eu2-N5	2.93	2.95
Eu2-N6	3.26	3.07
Eu2-N7	3.14	2.97
Eu2-N8	2.73	2.71

Optimized Cartesian coordinates for **3.1**.

```

7 -4.363586 -1.308194 -0.561580
7 -4.293900 1.598668 0.406659
8 -1.928546 -1.756388 -1.761164
8 -2.816247 1.530057 -1.829745
6 -5.548558 -0.538554 -0.106082
1 -5.694288 -0.756751 0.966561
1 -6.471270 -0.893400 -0.623507
6 -5.436393 0.971076 -0.315950
1 -5.307331 1.182090 -1.388084
1 -6.399943 1.442091 -0.009436
6 -4.549963 1.706595 1.862079
1 -5.016362 0.763387 2.194361
1 -5.285507 2.517376 2.080326
6 -4.302512 -2.629946 0.125685
1 -3.707899 -3.311930 -0.499810
1 -5.316473 -3.085768 0.202174
6 -4.300763 -1.474883 -2.047442
1 -4.309071 -0.475883 -2.515250
1 -5.156685 -2.066863 -2.431489
6 -2.981293 -2.176286 -2.438573
6 -3.957250 2.906278 -0.223214

```

1	-3.148276	3.393477	0.346230
1	-4.827346	3.595288	-0.244652
6	-3.454871	2.672999	-1.659369
7	-2.257977	0.894722	2.570633
7	-2.311327	-2.016520	1.560254
8	-0.256168	1.678251	0.664366
8	0.066839	-1.034738	0.662808
6	-2.618236	-0.294009	3.387700
1	-3.714132	-0.415702	3.348935
1	-2.360156	-0.124524	4.457511
6	-1.919098	-1.577830	2.930802
1	-0.833729	-1.406994	2.933763
1	-2.134613	-2.381734	3.672748
6	-3.701652	-2.542923	1.531413
1	-4.324025	-1.881610	2.156411
1	-3.746836	-3.555716	1.998936
6	-3.284385	1.970422	2.677845
1	-2.809213	2.907236	2.346021
1	-3.573043	2.132698	3.741988
6	-0.925920	1.451939	2.963589
1	-0.215309	0.633378	3.154838
1	-1.007168	2.055854	3.888744
6	-0.362856	2.317989	1.836778
6	-1.357871	-3.012958	0.998240
1	-1.714909	-3.273225	-0.008395
1	-1.342146	-3.937174	1.622547
6	0.082941	-2.449465	0.866643
8	-2.991151	-3.093510	-3.313446
8	-0.060672	3.523345	2.031135
8	-3.678296	3.535307	-2.556073
63	-1.831590	0.098782	-0.267848
1	0.634101	-2.659108	1.809990
6	0.790175	-3.123976	-0.317744
7	2.210890	-2.684347	-0.421139
1	0.244578	-2.812404	-1.222344
1	0.727548	-4.235961	-0.243359
6	2.741694	-2.837943	-1.799176
6	3.055203	-3.395538	0.570932
1	3.843268	-2.843067	-1.735711
1	2.453570	-3.827102	-2.224911
6	2.269436	-1.758619	-2.775440
6	4.340212	-2.655841	0.965195
1	2.439896	-3.556533	1.469935
1	3.334084	-4.410521	0.200191
7	2.722466	-0.369008	-2.443824
1	1.169104	-1.744971	-2.809306

1	2.618365	-2.034445	-3.796342
7	4.085855	-1.337879	1.578699
1	4.963086	-2.503090	0.068193
1	4.928524	-3.324958	1.640500
6	4.195621	-0.226991	-2.628552
6	1.972700	0.604082	-3.302953
6	5.257844	-0.435084	1.567337
6	3.475805	-1.414339	2.925588
6	4.803679	0.995109	-1.936405
1	4.673266	-1.140799	-2.238637
1	4.441686	-0.177303	-3.714105
1	2.330773	1.622630	-3.078992
1	2.136619	0.390146	-4.377796
6	0.461736	0.577227	-3.015149
6	5.658289	0.058018	0.173876
1	4.998697	0.427916	2.200526
1	6.148818	-0.926250	2.032090
1	2.975530	-2.386099	3.054326
1	4.243686	-1.356763	3.728148
6	2.408492	-0.329484	3.186818
7	4.659671	0.959934	-0.451857
1	4.314218	1.910957	-2.299677
1	5.876357	1.068727	-2.229338
8	0.160872	0.402093	-1.730102
8	-0.352005	0.733157	-3.957985
1	5.812821	-0.801690	-0.500102
1	6.647054	0.568834	0.254735
8	2.304539	0.615517	2.282864
8	1.692278	-0.448416	4.232002
6	4.737342	2.336525	0.118104
63	1.817000	0.403934	0.010311
1	4.634658	2.270149	1.214348
1	5.705568	2.827184	-0.115753
6	3.585922	3.208968	-0.413241
8	2.471907	2.539654	-0.645033
8	3.769346	4.444524	-0.601403

Optimized Cartesian coordinates for H3.1.

7	-4.274561	0.008397	1.404609
7	-4.191426	-1.107736	-1.467416
8	-1.757151	-0.087280	2.394832
8	-2.255979	-2.482853	-0.291067
6	-5.474065	-0.327097	0.584246
1	-5.800593	0.601525	0.083295
1	-6.316861	-0.642690	1.238869

6	-5.240615	-1.426440	-0.450601
1	-4.927504	-2.353479	0.054741
1	-6.208150	-1.649034	-0.954170
6	-4.619575	-0.070656	-2.444629
1	-5.191215	0.699353	-1.900312
1	-5.311890	-0.501730	-3.201665
6	-4.432625	1.356733	2.038121
1	-3.799184	1.385683	2.935739
1	-5.477320	1.497596	2.391072
6	-3.970665	-1.023205	2.454806
1	-3.817949	-2.001852	1.968108
1	-4.794212	-1.111654	3.189470
6	-2.663561	-0.641934	3.178039
6	-3.769675	-2.369095	-2.145369
1	-3.183875	-2.126400	-3.046417
1	-4.642523	-2.971311	-2.464854
6	-2.871309	-3.192938	-1.212440
7	-2.513531	1.341910	-2.282778
7	-2.670927	2.465006	0.596130
8	-0.200944	-0.237257	-1.734755
8	-0.251120	1.566034	0.164569
6	-3.137658	2.644645	-1.883843
1	-4.212053	2.464989	-1.715770
1	-3.071254	3.371340	-2.722697
6	-2.516198	3.288006	-0.640782
1	-1.443945	3.457588	-0.809089
1	-2.978852	4.291321	-0.501137
6	-4.072077	2.514381	1.105668
1	-4.742625	2.507705	0.229661
1	-4.266250	3.471564	1.640896
6	-3.434619	0.564476	-3.172089
1	-2.826138	-0.215174	-3.658220
1	-3.818487	1.217196	-3.987319
6	-1.223892	1.563811	-3.011514
1	-0.717183	2.446159	-2.585705
1	-1.409213	1.777789	-4.081405
6	-0.210284	0.414427	-2.899925
6	-1.686819	2.852234	1.654732
1	-1.917450	2.249800	2.543832
1	-1.796954	3.928310	1.913107
6	-0.218856	2.566124	1.220146
8	-2.545276	-0.838199	4.422012
8	0.601255	0.222657	-3.840753
8	-2.757543	-4.440817	-1.367831
63	-1.925985	-0.213769	-0.001251
1	0.226302	3.482147	0.786265

6	0.629476	2.020863	2.376895
7	2.012964	1.581089	1.979646
1	0.092021	1.142720	2.769217
1	0.695027	2.783208	3.187235
6	2.597670	0.780110	3.103549
6	2.881411	2.756020	1.659372
1	3.694759	0.807275	3.008552
1	2.359835	1.260745	4.077786
6	2.114038	-0.669434	3.151562
6	4.243589	2.423407	1.029145
1	2.318415	3.425545	0.994431
1	3.087689	3.339405	2.586709
7	2.582028	-1.498837	1.989375
1	1.013356	-0.696834	3.164531
1	2.455257	-1.128009	4.104645
7	4.214902	1.796540	-0.325369
1	4.805909	1.751600	1.696732
1	4.821039	3.376279	0.988062
6	4.024487	-1.857892	2.135752
6	1.731359	-2.730088	1.889842
6	5.520095	1.145396	-0.639806
6	3.852907	2.797427	-1.373205
6	4.690323	-2.286068	0.827880
1	4.550046	-0.985159	2.558624
1	4.139920	-2.680449	2.875180
1	2.099527	-3.355902	1.059453
1	1.769170	-3.321672	2.824408
6	0.277906	-2.350223	1.597458
6	5.747016	-0.171737	0.108882
1	5.536439	0.958874	-1.725565
1	6.375310	1.824367	-0.420516
1	4.377474	3.761599	-1.221960
1	4.151180	2.391352	-2.354385
6	2.347300	3.041786	-1.429273
7	4.733188	-1.211097	-0.209088
1	4.144385	-3.137978	0.393007
1	5.717286	-2.650559	1.055155
8	0.158873	-1.311670	0.760908
8	-0.666155	-2.976562	2.126653
1	5.721571	0.005946	1.196382
1	6.774490	-0.532458	-0.123354
8	1.639839	1.921261	-1.354582
8	1.852631	4.199058	-1.525422
6	4.955920	-1.820810	-1.550739
63	1.944126	-0.272259	-0.340350
1	5.179161	-1.022595	-2.278327

1	5.814280	-2.521947	-1.550366
6	3.693863	-2.552993	-2.039913
8	2.562617	-2.069308	-1.553873
8	3.791550	-3.510287	-2.851924
1	0.390473	1.847134	-0.608756

## APPENDIX C

**Grant of Permission**

Dear Dr. Moore:

Thank you for your interest in our copyrighted material, and for requesting permission for its use.

Permission is granted for the following subject to the conditions outlined below:

Recent Patents on Nanomedicine, 2011, 1, 88-100.

To be used in the following manner:

1. Bentham Science Publishers grants you the right to reproduce the material indicated above on a one-time, non-exclusive basis, solely for the purpose described. Permission must be requested separately for any future or additional use.
2. For an article, the copyright notice must be printed on the first page of article or book chapter. For figures, photographs, covers, or tables, the notice may appear with the material, in a footnote, or in the reference list.

Thank you for your patience while your request was being processed. If you wish to contact us further, please use the address below.

Sincerely,

***AMBREEN IRSHAD***

***Permissions & Rights Manager***

Bentham Science Publishers

Email: [permission@benthamscience.org](mailto:permission@benthamscience.org)

URL: [www.benthamscience.com](http://www.benthamscience.com)



RightsLink®

[Home](#)[Account Info](#)[Help](#)ACS Publications  
High quality. High impact.**Title:** Concentration-Independent pH Detection with a Luminescent Dimetallic Eu(III)-Based Probe**Author:** Jeremiah D. Moore, Richard L. Lord, G. Andrés Cisneros, and Matthew J. Allen**Publication:** Journal of the American Chemical Society**Publisher:** American Chemical Society**Date:** Oct 1, 2012

Copyright © 2012, American Chemical Society

Logged in as:

Jeremiah Moore

Account #:  
3000430833[LOGOUT](#)**PERMISSION/LICENSE IS GRANTED FOR YOUR ORDER AT NO CHARGE**

This type of permission/license, instead of the standard Terms & Conditions, is sent to you because no fee is being charged for your order. Please note the following:

- Permission is granted for your request in both print and electronic formats, and translations.
- If figures and/or tables were requested, they may be adapted or used in part.
- Please print this page for your records and send a copy of it to your publisher/graduate school.
- Appropriate credit for the requested material should be given as follows: "Reprinted (adapted) with permission from (COMPLETE REFERENCE CITATION). Copyright (YEAR) American Chemical Society." Insert appropriate information in place of the capitalized words.
- One-time permission is granted only for the use specified in your request. No additional uses are granted (such as derivative works or other editions). For any other uses, please submit a new request.

[BACK](#)[CLOSE WINDOW](#)

## REFERENCES

- (1) Villaraza, A.J.L.; Bumb, A.; Brechbiel, M.W. *Chem. Rev.* **2010**, *110*, 2921–2959.
- (2) *The Chemistry of Contrast Agents in Medical Magnetic Resonance Imaging*, 1<sup>st</sup> ed.; Merbach A.E.; Tóth É., Eds.; Wiley: Chichester, U.K.; 2001.
- (3) Caravan, P.; Ellison, J.J.; McMurry, T.J.; Lauffer, R.B. *Chem. Rev.* **1999**, *99*, 2293–2352.
- (4) Brunet, E.; Juanes, O.; Rodriguez-Ubis, J.C. *Curr. Chem. Biol.* **2007**, *1*, 11–39.
- (5) Port, M. Contrast agent encapsulating systems for CEST imaging. WO032705, 2006.
- (6) Yang, J.J.; Liu, Z-R. Contrast agents prepared from mutagenized metal ion-binding scaffold proteins. WO009058, 2007.
- (7) Van Veggel, F.C.J.M.; Prosser, R.S.; Dong, C. Lanthanide rich nanoparticles, and their investigative uses in MRI and related technologies. CA2575649, 2007.
- (8) Axelsson, O.; Cuthbertson, A.; Meijer, A. Preparation of contrast agents for magnetic resonance imaging and spectroscopy consisting of a cyclic oligoamide core of 3 to 4 identical monomer units with 3 to 4 paramagnetic chelate side chains. WO111514, 2007.
- (9) Kiessling, L.L.; Raines, R.T.; Allen, M.J. Magnetic resonance imaging contrast agents synthesized using ring-opening metathesis polymerization. WO131084, 2007.
- (10) Hovinen, J. Lanthanide chelates and chelating agents containing triazolyl subunits. WO025886, 2008.
- (11) Uvdal, K. Compositions containing metal oxide nanoparticles and their use as contrast agents in magnetic resonance imaging. WO096279, 2008.
- (12) Axelsson, O.; Uvdal, K. Visualization of biological material by the use of coated contrast agents. WO096280, 2008.

- (13) Moore, D.A. High relaxivity coordinatively unsaturated lanthanide complexes. WO134289, 2008.
- (14) Grotjahn, D.; Weiner, E. Bifunctional chelators for sequestering lanthanides in cancer treatment. US0107606, 2008.
- (15) Langereis, S.; Burdinski, D.; Bevers, E.M.; Hackeng, T.M.; Pikkemaat, J.A. CEST MRI contrast agents based on non-spherical erythrocyte ghosts. WO060403, 2009.
- (16) Burdinski, D.; Langereis, S.; Pikkemaat, J.A. Nonspherical contrast agents for CEST MRI based on bulk magnetic susceptibility effect. WO069051, 2009.
- (17) Yang, J.J.; Liu, Z.; Li, S.; Zhou, Y.; Jiang, J.; Xue, S.; Qiao, J.; Wei, L. Contrast agents, methods for preparing contrast agents, and methods of imaging. WO146099, 2009.
- (18) Meijer, A.; Axelsson, O.; Braathe, A.; Olsson, A.; Johansen, J.H.; Wynn, D.G. Compounds comprising paramagnetic chelates arranged around a central core and their use in magneto resonance imaging and spectroscopy. WO127715, 2009.
- (19) Langereis, S.; Keupp, J.; Gruell, H.; Burdinski, D.; Beelen, D. Drug carrier providing MRI contrast enhancement. WO029469, 2010.
- (20) Reineke, T.; Bryson, J. Theranostic polycation beacons comprising oligoethyleneamine repeating units and lanthanide chelates. WO006011, 2011.
- (21) Butlin, N.G.; Raymond, K.N.; Xu, J.; D'Aleo, A. Preparation of macrocyclic hydroxypyridinonyl (HOPO)-containing chelators of lanthanides and their conjugates as luminescent probes. WO025790, 2011.
- (22) Gunnlaugsson, T.; Leonard, J.P. *Chem. Commun.* **2005**, 3114–3131.
- (23) Langereis, S.; Dirksen, A.; Hackeng, T.M.; van Genderen, M.H.P.; Meijer, E.W. *New J. Chem.* **2007**, *31*, 1152–1160.

- (24) Menjoge, A.R.; Kannan, R.M.; Tomalia, D.A. *Drug Discov. Today* **2010**, *15*, 171–185.
- (25) Rocha, J.; Carlos, L.D.; Paz, F.A.A.; Ananias, D. *Chem. Soc. Rev.* **2011**, *40*, 926–940.
- (26) Yan, G.P.; Ai, C.W.; Li, L.; Zong, R.F.; Liu, F. *Chin. Sci. Bull.* **2010**, *55*, 3085–3093.
- (27) Yu, G.; Yamashita, M.; Tian, M.; Zhang, H.; Ozaki, N.; Yamashita, J.; Fujie, M.; Takehar, Y.; Sakahara, H. *Curr. Med. Imaging Rev.* **2010**, *6*, 42–45.
- (28) Greenwood, N.N.; Earnshaw, A. *Chemistry of the elements*, 2nd ed; Amsterdam, 1998; 1233.
- (29) Suchý, M.; Hudson, R.H.E. *Eur. J. Org. Chem.* **2008**, 4847–4865.
- (30) Zhang, S.; Winter, P.; Wu, K.; Sherry, A.D. *J. Am. Chem. Soc.* **2001**, *123*, 1517–1518.
- (31) Green, K.N.; Viswanathan, S.; Rojas-Quijano, F.A.; Kovacs, Z.; Sherry, A.D. *Inorg. Chem.*; **2011**, *50*, 1648–1655.
- (32) Morrow, J.R.; Chin, K.O.A. *Inorg. Chem.* **1993**, *32*, 3357–3361.
- (33) Kotkova, Z.; Pereira, G. A.; Djanashvili, K.; Kotek, J.; Rudovsky, J.; Hermann, P.; Vander Elst, L.; Muller, R. N.; Geraldes, C.F.G.C.; Lukes, I.; Peters, J.A. *Eur. J. Inorg. Chem.* **2009**, 119–136.
- (34) Ranganathan, R.S.; Fernandez, M.E.; Kang, S.I.; Nunn, A.D.; Ratsep, P.C.; Pillai, K.M.; Zhang, X.; Tweedle, M.F. *Invest. Radiol.* **1998**, *33*, 779–797.
- (35) Livramento, J.B.; Helm, L.; Sour, A.; O’Neil, C.; Merbach, A.E.; Tóth, É. *Dalton Trans.* **2008**, 1195–1202.
- (36) Kowalewski, J.; Nordenskiöld, L.; Benetis, N.; Westlund, P.-O. *Prog. Nucl. Magn. Reson. Spectroscop.* **1985**, *17*, 141–185.
- (37) Lauffer, R.B. *Chem. Rev.* **1987**, *87*, 901–927.
- (38) Cacheris, W.P.; Quay, S.C.; Rocklage, S.M. *Magn. Reson. Imaging* **1990**, *8*, 467–481.

- (39) Caravan, P. *Chem. Soc. Rev.* **2006**, *35*, 512–523.
- (40) Terreno, E.; Castelli, D.D.; Viale, A.; Aime, S. *Chem. Rev.* **2010**, *110*, 3019–3042.
- (41) Datta, A.; Raymond, K.N. *Acc. Chem. Res.* **2009**, *42*, 938–947.
- (42) Andrec, M.; Montelione, G.T.; Levy, R.M. *J. Magn. Reson.* **1999**, *139*, 408–421.
- (43) Dunand, F.A.; Tóth, É.; Hollister, R.; Merbach, A.E. *J. Biol. Inorg. Chem.* **2001**, *6*, 247–255.
- (44) Rudovský, J.; Botta, M.; Hermann, P.; Koridze, A.; Aime, S. *Dalton Trans.* **2006**, 2323–2333.
- (45) Costa, J.; Balogh, E.; Turcryn, V.; Tripier, R.; Le Baccon, M.; Chuburu, F.; Handel, H.; Helm, L.; Tóth, É.; Merbach, A.E. *Chem. Eur. J.* **2006**, *12*, 6841–6851.
- (46) Mishra, A.; Fouskova, P.; Angelovski, G.; Balogh, E.; Mishra, A.K.; Logothetis, N.K.; Tóth, É. *Inorg. Chem.* **2008**, *47*, 1370–1381.
- (47) Tei, L.; Gugliotta, G.; Avedano, S.; Giovenzana, G.B.; Botta, M. *Org. Biomol. Chem.* **2009**, *7*, 4406–4414.
- (48) Jones, J.E.; Amoroso, A.J.; Dorin, I.M.; Parigi, G.; Ward, B.D.; Buurma, N.J.; Pope, S. J.A. *Chem. Commun.* **2011**, *47*, 3374–3376.
- (49) Miéville, P.; Jaccard, H.; Reviriego, F.; Tripier, R.; Helm, L. *Dalton Trans.* **2011**, *40*, 4260–4267.
- (50) Mastarone, D.J.; Harrison, V.S.R.; Eckermann, A.L.; Parigi, G.; Luchinat, C.; Meade, T.J. *J. Am. Chem. Soc.* **2011**, *133*, 5329–5337.
- (51) Tanwar, J.; Datta, A.; Tiwari, A.K.; Chaturvedi, S.; Ojha, H.; Allard, M.; Chaudary, N.K.; Thirumal, M.; Mishra, A.K. *Dalton Trans.* **2011**, *40*, 3346–3351.
- (52) Jebasingh, B.; Alexander, V. *Inorg. Chem.* **2005**, *44*, 9434–9443.

- (53) Platzek, J.; Schirmer, H.; Weinmann, H.-J.; Martin, J.L.; Harto, J.R. Trimeric, macrocyclically substituted halo-benzene derivatives. US0154989, 2006.
- (54) Rudovský, J.; Kotek, J.; Hermann, P.; Lukeš, I.; Mainero, V.; Aime, S. *Org. Biomol. Chem.* **2005**, *3*, 112–7.
- (55) Jászberényi, Z.; Sour, A.; Tóth, É.; Benmelouka, M.; Merbach, A.E. *Dalton Trans.* **2005**, 2713–2719.
- (56) Mato-Iglesias, M.; Platas-Iglesias, C.; Djanashvili, K.; Peters, J.A.; Tóth, É.; Balogh, E.; Muller, R.N.; Vander Elst, L.; de Blas, A.; Rodriguez-Blas, T. *Chem. Commun.* **2005**, 4729–4731.
- (57) Helm, L. *Future Med. Chem.* **2010**, *2*, 385–396.
- (58) Bryson, J.M.; Chu, W.-J.; Lee, J.-H.; Reineke, T.M. *Bioconjugate Chem.* **2008**, *19*, 1505–1509.
- (59) Song, Y.; Kohlmeir, E.K.; Meade, T.J. *J. Am. Chem. Soc.* **2008**, *130*, 6662–6663.
- (60) Song, Y.; Meade, T.J.; Kohlmeir, E. MRI contrast agents and related methods of use. US0196829, 2009.
- (61) Nicolle, G.M.; Yerly, F.; Imbert, D.; Böttger, U.; Bünzli, J.-C.; Merbach, A.E. *Chem. Eur. J.* **2003**, *9*, 5453–5467.
- (62) Powell, D.H.; Ni D.; Orla M.; Pubanz, D.; Helm, L.; Lebedev, Y.S.; Schlaepfer, W.; Merbach, A.E. *J. Am. Chem. Soc.* **1996**, *118*, 9333–9346.
- (63) Tóth, É.; Helm, L.; Merbach, A.E.; Hedinger, R.; Hegetschweiler, K.; Jánossy, A. *Inorg. Chem.* **1998**, *37*, 4104–4113.
- (64) McLachlan, A.D. *Proc. R. Soc. Lond. A* **1964**, *280*, 271–288.

- (65) Werner, E.J.; Kozhukh, J.; Botta, M.; Moore, E.G.; Avedano, S.; Aime, S.; Raymond, K.N. *Inorg. Chem.* **2009**, *48*, 277–286.
- (66) Zhang, S.; Merritt, M.; Woessner, D.E.; Lenkinski, R.E.; Sherry, A.D. *Acc. Chem. Res.* **2003**, *36*, 783–790.
- (67) Ward, K.M.; Aletras, A.H.; Balaban, R.S. *J. Magn. Reson.* **2000**, *143*, 79–87.
- (68) Ali, M.M.; Liu, G.; Shah, T.; Flask, C.A.; Pagel, M.D. *Acc. Chem. Rev.* **2009**, *42*, 915–924.
- (69) Hancu, I.; Dixon, W.T.; Woods, M.; Vinogradov, E.; Sherry, A.D.; Lenkinski, R.E. *Acta Radiol.* **2010**, *51*, 910–923.
- (70) Pikkemaat, J.A.; Wegh, R.T.; Lamerichs, R.; van de Molengraaf, R.A.; Langereis, S.; Burdinski, D.; Raymond, A.Y.F.; Janssen, H.M.; de Waal, B.F.M.; Willard, N.P.; Meijer, E.W.; Gruell, H. *Contrast Media Mol. Imaging* **2007**, *2*, 229–239.
- (71) Wu, Y.; Zhou, Y.; Ouari, O.; Woods, M.; Zhao, P.; Soesbe, T.C.; Kiefer, G.E.; Sherry, A. *J. Am. Chem. Soc.* **2008**, *130*, 13854–13855.
- (72) New, K.; Andolina, C.M.; Huang, C.-H.; Morrow, J.R. *Bioconjugate Chem.* **2009**, *20*, 1375–1382.
- (73) Suchý, M.; Li, A.X.; Bartha, R.; Hudson, R.H.E. *Tetrahedron Lett.* **2010**, *51*, 1087–1090.
- (74) Horrocks, W.D.; Jr.; Sudnick, D.R. *Acc. Chem. Res.* **1981**, *14*, 384–392.
- (75) Werts, M.H.V. *Sci. Prog.* **2005**, *88*, 101–131.
- (76) Choppin, G.R.; Peterman, D.R. *Coord. Chem. Rev.* **1998**, *174*, 283–299.
- (77) Lis, S. *Chem. Anal.* **1993**, *38*, 443–54.
- (78) Dickson, E.F.G.; Poollak, A.; Diamandis, E.P. *J. Photochem. Photobiol. B* **1995**, *27*, 3–19.
- (79) Yuan, J.; Wang, G. *Trends Anal. Chem.* **2006**, *25*, 490–500.
- (80) Faulkner, S.; Pope, S.J. *J. Am. Chem. Soc.* **2003**, *125*, 10526–10527.

- (81) Bünzli, J.-C.G.; Chauvin, A.-S.; Kim, H.K.; Deiters, E.; Eliseeva, S.V. *Coord. Chem. Rev.* **2010**, *254*, 2623–2633.
- (82) Moore, E.G.; Samuel, A.P.S.; Raymond, K.N. *Acc. Chem. Res.* **2009**, *42*, 542–552.
- (83) Andolina, C.M.; Morrow, J.R. *Eur. J. Inorg. Chem.* **2011**, 154–164.
- (84) Nwe, K.; Andolina, C.M.; Morrow, J.R. *J. Am. Chem. Soc.* **2008**, *130*, 14861–14871.
- (85) Harte, A.J.; Jensen, P.; Plush, S.E.; Kruger, P.E.; Gunnlaugsson, T. *Inorg. Chem.* **2006**, *45*, 9465–9474.
- (86) Andrews, M.; Amoroso, A.J.; Harding, L.P.; Pope, S.J.A. *Dalton Trans.* **2010**, *39*, 3407–3411.
- (87) Murray, B.S.; Parker, D.; dos Santos, C.M.G.; Peacock, R.D. *Eur. J. Inorg. Chem.* **2010**, 2663–2672.
- (88) Shiraishi, Y.; Furubayashi, Y.; Nishimura, G.; Hirai, T. *J. Lumin.* **2007**, *127*, 623–632.
- (89) Plush, S.E.; Gunnlaugsson, T. *Org. Lett.* **2007**, *9*, 1919–1922.
- (90) (a) Le Baccon, M.; Chuburu, F.; Toupet, L.; Handel, H.; Soibinet, M.; Déchamps-Olivier, I.; Barbier, J-P.; Aplincourt, M. *New J. Chem.* **2001**, *25*, 1168–1174. (b) Baker, W. C.; Choi, M. J.; Hill, D. C.; Thompson, J. L.; Petillo, P. A. *J. Org. Chem.* **1999**, *64*, 2683–2689.
- (91) Kasireddy, K.; Moghis, U.A.; Ali, S.M.; Ahmad, I. *Tetrahedron Lett.* **2004**, *45*, 2743–2746.
- (92) Dadabhoy, A.; Faulkner, S.; Sammes, P. G. *J. Chem. Soc., Perkin Trans. 2* **2002**, 348–357.
- (93) Moore, J.D.; Lord, R.L.; Cisneros, G.A.; Allen, M.J. *J. Am. Chem. Soc.* **2012**, *134*, 17372–17375.
- (94) (a) Parker, D.; Senanayake, K.; Williams, J. A. G. *Chem. Commun.* **1997**, 1777–1778. (b) Aime, S.; Barge, A.; Botta, M.; Howard, J. A. K.; Katakya, R.; Lowe, M. P.; Moloney, J. M.; Parker, D.; de Sousa, A. V. *Chem. Commun.* **1999**, 1047–1048. (c) Parker, D. *Coord.*

- Chem. Rev.* **2000**, *205*, 109–130. (d) Lowe, M. P.; Parker, D.; Reany, O.; Aime, S.; Botta, M.; Castellano, G.; Gianolio, E.; Pagliarin, R. *J. Am. Chem. Soc.* **2001**, *123*, 7601–7609. (e) Woods, M.; Sherry, A. D. *Inorg. Chem.* **2003**, *42*, 4401–4408. (f) Pal, R.; Parker, D. *Chem. Commun.* **2007**, 474–476. (g) Hanaoka, K.; Kikuchi, K.; Kobayashi, S.; Nagano, T. *J. Am. Chem. Soc.* **2007**, *129*, 13502–13509. (h) Pal, R.; Parker, D. *Org. Biomol. Chem.* **2008**, *6*, 1020–1033. (i) Thibon, A.; Pierre, V. C. *J. Am. Chem. Soc.* **2009**, *131*, 434–435. (j) Andrews, M.; Amoroso, A. J.; Harding, L. P.; Pope, S. J. A. *Dalton Trans.* **2010**, *39*, 3407–3411. (k) Weitz, E. A.; Pierre, V. C. *Chem. Commun.* **2011**, *47*, 541–543.
- (95) (a) Dickins, R. S.; Gunnlaugsson, T.; Parker, D.; Peacock, R. D. *Chem. Commun.* **1998**, 1643–1644. (b) Dickins, R. S.; Aime, S.; Batsanov, A. S.; Beeby, A.; Botta, M.; Bruce, J. I.; Howard, J. A. K.; Love, C. S.; Parker, D.; Peacock, R. D.; Puschmann, H. *J. Am. Chem. Soc.* **2002**, *124*, 12697–12705. (c) Atkinson, P.; Bretonniere, Y.; Parker, D. *Chem. Commun.* **2004**, 438–439. (d) Bretonniere, Y.; Cann, M. J.; Parker, D.; Slater, R. *Org. Biomol. Chem.* **2004**, *2*, 1624–1632. (e) Parker, D.; Yu, J. *Chem. Commun.* **2005**, 3141–3143. (f) Poole, R. A.; Bobba, G.; Cann, M. J.; Frias, J.-C.; Parker, D.; Peacock, R. D. *Org. Biomol. Chem.* **2005**, *3*, 1013–1024. (g) Harte, A. J.; Jensen, P.; Plush, S. E.; Kruger, P. E.; Gunnlaugsson, T. *Inorg. Chem.* **2006**, *45*, 9465–9474. (h) Poole, R. A.; Kielar, F.; Richardson, S. L.; Stenson, P. A.; Parker, D. *Chem. Commun.* **2006**, 4084–4086. (i) Poole, R. A.; Montgomery, C. P.; New, E. J.; Congreve, A.; Parker, D.; Botta, M. *Org. Biomol. Chem.* **2007**, *5*, 2055–2062. (j) Pålsson, L.-O.; Pal, R.; Murray, B. S.; Parker, D.; Beeby, A. *Dalton Trans.* **2007**, 5726–5734. (k) Plush, S. E.; Gunnlaugsson, T. *Org. Lett.* **2007**, *9*, 1919–1922. (l) Kielar, F.; Montgomery, C. P.; New, E. J.; Parker, D.; Poole, R. A.; Richardson, S. L.; Stenson, P. A. *Org. Biomol. Chem.* **2007**, *5*, 2975–2982. (m) Murray, B.

- S.; New, E. J.; Pal, R.; Parker, D. *Org. Biomol. Chem.* **2008**, *6*, 2085–2094. (n) Andolina, C. M.; Morrow, J. R. *Eur. J. Inorg. Chem.* **2011**, 154–164.
- (96) (a) Song, B.; Wang, G.; Tan, M.; Yuan, J. *J. Am. Chem. Soc.* **2006**, *128*, 13442–13450. (b) Page, S. E.; Wilke, K. T.; Pierre, V. C. *Chem. Commun.* **2010**, *46*, 2423–2425. (c) Pershagen, E.; Nordholm, J.; Borbas, K. E. *J. Am. Chem. Soc.* **2012**, *134*, 9832–9835.
- (97) (a) Yu, J.; Parker, D.; Pal, R.; Poole, R. A.; Cann, M. J. *J. Am. Chem. Soc.* **2006**, *128*, 2294–2299. (b) Halim, M.; Tremblay, M. S.; Jockusch, S.; Turro, N. J.; Sames, D. *J. Am. Chem. Soc.* **2007**, *129*, 7704–7705. (c) Kielar, F.; Congreve, A.; Law, G.-I.; New, E. J.; Parker, D.; Wong, K.-L.; Castroño, P.; de Mendoza, J. *Chem. Commun.* **2008**, 2435–2437.
- (98) Bobba, G.; Frias, J. C.; Parker, D. *Chem. Commun.* **2002**, 890–891.
- (99) Jin, D.; Piper, J. A. *Anal. Chem.* **2011**, *83*, 2294–2300.
- (100) (a) Beeby, A.; Botchway, S. W.; Clarkson, I. M.; Faulkner, S.; Parker, A. W.; Parker, D.; Williams, J. A. G. *J. Photochem. Photobiol.; B* **2000**, *57*, 83–89. (b) You, Y.; Han, Y.; Lee, Y.-M.; Park, S. Y.; Nam, W.; Lippard, S. J. *J. Am. Chem. Soc.* **2011**, *133*, 11488–11491. (c) You, Y.; Lee, S.; Kim, T.; Ohkubo, K.; Chae, W.-S.; Fukuzumi, S.; Jhon, G.-J.; Nam, W.; Lippard, S. J. *J. Am. Chem. Soc.* **2011**, *133*, 18328–18342. (d) Holst, G.; Kohls, O.; Klimant, I.; König, B.; Kühl, M.; Richter, T. *Sens. Actuators, B* **1998**, *51*, 163–170.
- (101) Helmlinger, G.; Yuan, F.; Dellian, M.; Jain, R. K. *Nat. Med.* **1997**, *3*, 177–182.
- (102) Moore, J. D.; Allen, M. J. *Recent Patents on Nanomedicine* **2011**, *1*, 88–100.
- (103) (a) Supkowski, R. M.; Horrocks, W. D.; Jr. *Inorg. Chim. Acta* **2002**, *340*, 44–48. (b) Horrocks, W. D.; Jr.; Sudnick, D. R. *J. Am. Chem. Soc.* **1979**, *101*, 334–340.
- (104) Barge, A.; Cravotto, G.; Gianolio, E.; Fedeli, F. *Contrast Med. Mol. Imaging* **2006**, *1*, 184–188.

- (105) (a) Gibbs, E. L.; Lennox, W. G.; Nims, L. F.; Gibbs, F. A. *J. Biol. Chem.* **1942**, *144*, 325–332. (b) Wike-Hooley, J. L.; van den Berg, A. P.; van der Zee, J.; Reinhold, H. S. *Eur. J. Cancer Clin. Oncol.* **1985**, *21*, 785–791. (c) Gerweck, L. E.; Seetharaman, K. *Cancer Res.* **1996**, *56*, 1194–1198.
- (106) (a) Gaussian 09, Revision A.1, Frisch, M. J.; Trucks, G. W.; Schlegel, H. B.; Scuseria, G. E.; Robb, M. A.; Cheeseman, J. R.; Scalmani, G.; Barone, V.; Mennucci, B.; Petersson, G. A.; Nakatsuji, H.; Caricato, M.; Li, X.; Hratchian, H. P.; Izmaylov, A. F.; Bloino, J.; Zheng, G.; Sonnenberg, J. L.; Hada, M.; Ehara, M.; Toyota, K.; Fukuda, R.; Hasegawa, J.; Ishida, M.; Nakajima, T.; Honda, Y.; Kitao, O.; Nakai, H.; Vreven, T.; Montgomery, Jr., J. A.; Peralta, J. E.; Ogliaro, F.; Bearpark, M.; Heyd, J. J.; Brothers, E.; Kudin, K. N.; Staroverov, V. N.; Kobayashi, R.; Normand, J.; Raghavachari, K.; Rendell, A.; Burant, J. C.; Iyengar, S. S.; Tomasi, J.; Cossi, M.; Rega, N.; Millam, J. M.; Klene, M.; Knox, J. E.; Cross, J. B.; Bakken, V.; Adamo, C.; Jaramillo, J.; Gomperts, R.; Stratmann, R. E.; Yazyev, O.; Austin, A. J.; Cammi, R.; Pomelli, C.; Ochterski, J. W.; Martin, R. L.; Morokuma, K.; Zakrzewski, V. G.; Voth, G. A.; Salvador, P.; Dannenberg, J. J.; Dapprich, S.; Daniels, A. D.; Farkas, Ö.; Foresman, J. B.; Ortiz, J. V.; Cioslowski, J.; Fox, D. J. Gaussian, Inc., Wallingford CT, 2009. (b) Adamo, C.; Barone V. *J. Chem. Phys.* **1999**, *110*, 6158–6170.
- (107) Albin, M.; Horrocks, W. D.; Jr.; Liotta, F. J. *Chem. Phys. Lett.* **1982**, *85*, 61–64.
- (108) (a) Piguet, C.; Bünzli, J.-C.; Berardinelli, G.; Hopfgartner, G.; Williams, A.F. *J. Am. Chem. Soc.* **1993**, *115*, 8197–8206. (b) Murakami, S.; Herren, M.; Doris, R.; Sakurai, T.; Morita, M. *J. Lumin.* **1999**, 215–219. (c) Sosa-Fonseca, R.; Flores, M.; Rodriguez, R.; Hernández, J.; Muñoz, F. *J. Lumin.* **2001**, *93*, 327–332. (d) Tapia, M.J.; Burrows, H.D.

- Langmuir* **2002**, *18*, 1872–1876. (e) Ramaya, A.R.; Sharma, D.; Srinivasan, N.; Reddy, M.L.P. *Inorg. Chem.* **2012**, *51*, 8818–8826. (f) Rodrigues, M.O.; Dutra, J.D.L.; Nunes, L.A.O.; de Sá, G.F.; de Azevedo, W.M.; Silva, P.; Paz, F.A.A.; Freire, R.O.; Júnior, S.A. *J. Phys. Chem. C* **2012**, *116*, 19951–19957.
- (109) (a) Matthews, K.D.; Fairman, R.A.; Johnson, A.; Spence, K.V.N.; Kahwa, I.A.; McPherson, G.L.; Robotham, H. *J. Chem. Soc., Dalton Trans.* **1993**, 1719–1723. (b) Buddhudu, S.; Morita, M.; Murakami, S.; Rau, S. *J. Lumin.* **1999**, 199–203. (c) Chewpraditkul, W.; Shen, Y.; Chen, D.; Beitlerova, A.; Nikl, M. *Optical Mater.* **2013**, *35*, 426–430.
- (110) Tanner, P.A.; Wang, J. *Chem. Phys. Lett.* **2008**, *455*, 335–338.
- (111) Singh-Wilmot, M.A.; Kahwa, I.A.; White, A.J.P.; Williams, D.J.; Lough, A.J. *Polyhedron* **2010**, *29*, 270–279.
- (112) Lee, M.; Tremblay, M.S.; Jockusch, S.; Turro, N.J.; Sames, D. *Org. Lett.* **2011**, *13*, 2802–2805.
- (113) Faulkner, S.; Pope, S.J.A. *J. Am. Chem. Soc.* **2003**, *125*, 10526–10527.
- (114) Tremblay, M.S.; Sames, D. *Chem. Commun.* **2006**, 4116–4118.
- (115) Nonat, A.; Regueiro-Figueroa, M.; Esteban-Gómez, D.; de Blas, A.; Rodríguez-Blas, T.; Platas-Iglesias, C.; Charbonnière, L.J. *Chem. Eur. J.* **2012**, *18*, 8163–8173.
- (116) Bünzli, J.-C.; Eliseeva, S.V. Basics of Lanthanide Photophysics. In *Lanthanide Luminescence: Photophysical, Analytical, and Biological Aspects*; Springer-Verlag: Berlin, 2010.

- (117) (a) Horrocks, W.D.; Jr.; Rhee, M.-J.; Snyder, A.P.; Sudnick, D.R. *J. Am. Chem. Soc.* **1980**, *102*, 3650–3652. (b) Snyder, A.P.; Sudnick, D.R.; Arkle, V.K.; Horrocks, W.D.; Jr. *Biochemistry* **1981**, *20*, 3334–3339.
- (118) (a) Ofelt, G.S. *J. Chem. Phys.* **1963**, *38*, 2171–2180. (b) Dorenbos, P. *J. Lumin.* **2000**, *91*, 91–106. (c) Peijzel, P.S.; Meijerink, A.; Wegh, R.T.; Reid, M.F.; Burdick, G.W. *J. Solid State Chem.* **2005**, *178*, 448–453. (d) Srivastava, A.M.; Comanzo, H.A.; Camardello, S.J.; Aycibin, M.; Happek, U. *Optical Mater.* **2012**, *34*, 591–595. (e) Chewpraditkul, W.; Shen, Y.; Chen, D.; Beitlerova, A.; Nikl, M. *Optical Mater.* **2013**, *35*, 426–430.

**ABSTRACT****DESIGN, SYNTHESIS, AND LUMINESCENCE PROPERTIES  
OF BRIDGED DIMETALLIC LANTHANIDE COORDINATION  
COMPOUNDS**

by

**JEREMIAH D. MOORE****August 2013****Advisor:** Dr. Matthew J. Allen**Major:** Chemistry**Degree:** Doctor of Philosophy

I synthesized and characterized new homo- and heterodimetallic  $\text{Eu}^{3+}$ - and  $\text{Tb}^{3+}$ -containing complexes. Solution-phase luminescence measurements and density functional theory (DFT)-optimized structures indicated that all complexes were nearly isostructural and contained a dimetallic lanthanide core bridged by three oxygen atoms that are covalently bound to the ligand backbone. The homodimetallic  $\text{Eu}^{3+}$  complex behaved as a concentration-independent pH sensor that correlates the luminescence-decay rate of the complex to pH. The probable mechanism of pH sensing was attributed to the modulation of a hydroxyl oscillator in the  $\text{Eu}^{3+}$  coordination sphere, which was a previously unreported method to sense pH. The heterodimetallic  $\text{Tb}^{3+}/\text{Eu}^{3+}$  complex displayed energy transfer from  $\text{Tb}^{3+}$  to  $\text{Eu}^{3+}$  that is unprecedentedly efficient. The observed energy transfer confirmed that the  $\text{Tb}^{3+}$ - $\text{Eu}^{3+}$  distance in the heterodimetallic complex is within 10 Å and demonstrated a unique interaction between lanthanide ions.

## AUTOBIOGRAPHICAL STATEMENT

### Education

Wayne State University, Detroit, MI  
August 2007–Present  
Degree: pursuing Ph.D. in Inorganic Chemistry

University of Michigan, Flint, MI  
August 2002–August 2007  
Major: Chemistry  
Degree: B.S. (ACS Certified)

### Research Experience

**Wayne State University**                      January 2008–August 2013    (Graduate Student)  
Advisor: Prof. Matthew J. Allen  
Synthesis and study of dinuclear lanthanide complexes as contrast agents for magnetic resonance imaging

**University of Michigan, Flint**              May 2005–August 2007        (Undergraduate)  
Advisor: Prof. Robert Stach  
Effects of nerve growth factor gradients on axonal growth of pheochromocytoma-12

### Honors and Awards

WSU Graduate Student Professional Travel Award, 2010  
WSU Departmental Citation for Excellence in Teaching Service, 2009  
University of Michigan, Flint Chemistry Researcher of the Year, 2007

### Publications

**Moore, J.D.**; Lord, R.L.; Cisneros, G.A.; Allen, M.J. Concentration-Independent pH Detection with a Luminescent Dimetallic Eu(III)-Based Probe. *J. Am. Chem. Soc.* **2012**, *134*, 17372–17375.

**Moore, J. D.**; Allen, M. J. Multilanthanide Systems for Medical Imaging Applications. *Recent Patents on Nanomedicine* **2011**, *1*, 88–100.

### Patent

Allen, M. J.; Gamage, N.-D. H.; **Moore, J. D.** “Dramatic Oxidative Stabilization of Aqueous Europium” PCT/US11/21643 filed January 19, 2011.